

GLOBAL THERMOSPHERIC RESPONSE TO GEOMAGNETIC STORMS

by

Padmashri Suresh

A dissertation submitted in partial fulfillment
of the requirements for the degree

of

DOCTOR OF PHILOSOPHY

in

Electrical Engineering

Approved:

Charles Swenson, Ph.D.
Major Professor

Jan Sojka, Ph.D.
Committee Member

Robert Schunk, Ph.D.
Committee Member

Todd Moon, Ph.D.
Committee Member

Jacob Gunther, Ph.D.
Committee Member

Mark R. McLellan, Ph.D.
Vice President for Research and
Dean of the School of Graduate Studies

UTAH STATE UNIVERSITY
Logan, Utah

2016

Copyright © Padmashri Suresh 2016

All Rights Reserved

ABSTRACT

Global Thermospheric Response to Geomagnetic Storms

by

Padmashri Suresh, Doctor of Philosophy

Utah State University, 2016

Major Professor: Charles Swenson, Ph.D.
Department: Electrical and Computer Engineering

Geomagnetic storms deposit energy and momentum into the Earth's magnetosphere which in turn energizes the terrestrial atmosphere through Joule heating and particle precipitation. This storm energy predominantly converges at altitudes of 100 to 150 km, corresponding to the lower thermospheric region, which is then globally redistributed throughout the thermosphere. It is essential that we understand the times and magnitudes of this energy to understand the terrestrial atmospheric response to geomagnetic storms. However, our current knowledge is mostly limited to the studies of orbital altitudes of the thermosphere. We aim to fill this gap by conducting a statistical study of lower thermospheric response to geomagnetic storms. We use neutral temperature data from SABER (Sounding of the Atmosphere Using Broadband Emission Radiometry) instrument onboard the TIMED (Thermosphere, Ionosphere, and Mesosphere Energy Dynamics) satellite for this study.

We devise a procedure to extract the storm response from SABER temperature measurements and deduce the magnitudes and times of the global storm energy redistribution in the 100 to 120 km altitude of the thermosphere. We use methods of inferential and descriptive statistics to investigate the lower thermospheric response for 145 storm intervals

that occurred between 2002 and 2010. We also investigate the performance of the state-of-art physics and empirical models in replicating the lower thermosphere during geomagnetic storms.

(172 pages)

PUBLIC ABSTRACT

Global Thermospheric Response to Geomagnetic Storms

Padmashri Suresh

The terrestrial atmospheric region between the altitudes of 90 km and 600 km is known as the thermosphere region. The thermosphere is continuously modulated by particle emissions and magnetic fields that originate from the sun. These fields and emissions are intensified during events known as geomagnetic storms which alter the state of the thermosphere by dumping gigawatts of energy. This energy is mostly deposited in the lower thermosphere regions of 150 km and below and can potentially have hazardous repercussions on the technological assets of mankind. These storms can disrupt radio communication systems, interrupt electric power systems, threaten the safety of astronauts, and disrupt global position systems (GPS), all of which can wreck havoc on the technology-dependent human society. Hence it is essential that we understand and predict the influence of these storms on the terrestrial thermosphere.

Our current understanding of the thermospheric response to the geomagnetic storm energy is limited to observations of the thermospheric state at orbital altitudes of 400 km and above. The state of the thermosphere at altitudes of 150 km and below during geomagnetic storms is largely unknown. This lower thermospheric response is instrumental in understanding and predicting the thermospheric state during geomagnetic storms. In this dissertation we bridge the gap in understanding the thermospheric response to storms by observing the change in lower thermospheric state in the event of geomagnetic storm occurrences.

We conduct this study using kinetic temperatures obtained from the SABER (Sounding of the Atmosphere Using Broadband Emission Radiometry) instrument onboard the TIMED (Thermosphere, Ionosphere, and Mesosphere Energy Dynamics) satellite. We conduct a

statistical study of storms corresponding to a decade worth of data to find out the magnitude and time scales of the geomagnetic storm induced changes of the lower thermospheric state. We use methods of inferential and descriptive statistics to investigate the storm induced global changes for more than a hundred storms that occurred between 2002 and 2010. We also investigate the performance of the state-of-art physics and empirical models in predicting the lower thermospheric state during geomagnetic storms.

To Sunny and Comet.

ACKNOWLEDGMENTS

I would like to express my sincere gratitude to my PhD advisor Dr. Charles Swenson. I cannot thank him enough for his excellent mentorship and support throughout my graduate school tenure. He is an exemplary individual who has always inspired me to do the “hard things”. My graduate school journey would not be half as rewarding as it was if it weren’t under his advisement.

I would also like to thank my dissertation committee members, Dr. Jan Sojka, Dr. Robert Schunk, Dr. Todd Moon and Dr. Jacob Gunther for their willingness to serve on my dissertation committee. I am grateful for all the time they spent on reviewing this work and for all of their valuable comments. I would also like to thank Dr. Edmund Spencer for his time spent on being a committee member during the earlier stages of this work.

I would like to express my gratitude to Dr. Andrew Christensen whose idea of retirement includes tirelessly guiding and inspiring students. I am extremely grateful for his encouragement and mentorship. I would like to particularly thank him for his patience in reviewing the messy drafts of this dissertation and for his help in making this dissertation better.

I am thankful for the various research programs, the opportunity to participate in which, helped me carry out this work. I would like to express my gratitude for receiving the NASA Earth and Space Science fellowship which was the primary funding source for this work. I would like to express my gratitude for being given the opportunity to attend the Heliophysics summer school which helped me to hit the ground running when I started this work. I would like to thank the Los Alamos National Laboratory for awarding me the Vela fellowship through their Space Weather Summer School program, which helped me to pursue some of the research ideas that aided this work.

I would like to thank my family for their support. I thank my husband Alok Shenoy for his patience and encouragement. I thank him for being my biggest cheerleader and for always believing in me. I would like to thank my mum Prema and dad Suresh for their love

and their faith in my abilities. Finally, I would like to thank the Almighty for giving me the courage and strength to pursue this work.

Padmashri Suresh

CONTENTS

	Page
ABSTRACT	iii
PUBLIC ABSTRACT	v
ACKNOWLEDGMENTS	viii
LIST OF TABLES	xii
LIST OF FIGURES	xiii
1 INTRODUCTION	1
1.1 Geospace Environment	1
1.1.1 Magnetosphere	2
1.1.2 Geomagnetic Storms	3
1.1.3 Terrestrial Atmosphere	4
1.2 Energetics and Dynamics of Thermosphere	6
1.3 Thermosphere Response to Geomagnetic Storms: Current Understanding	8
1.4 Dissertation Objectives	10
1.5 Importance of the Dissertation Objectives	11
1.6 Methods	12
1.6.1 SABER Temperature Data	12
1.6.2 Proxies for Geomagnetic Storms	15
1.6.3 Thermospheric Models	16
1.7 Outline of Dissertation	17
2 QUIET TIME VARIATION IN THE LOWER THERMOSPHERE	19
2.1 Thermospheric Quiet Times	21
2.2 Thermospheric Quiet Time Variations	23
2.2.1 Solar Wind Variation	23
2.2.2 Tidal and Wave Variability	23
2.2.3 Solar Cycle Variations	26
2.3 Thermospheric Quiet Time Variation Model	26
2.3.1 Bias and Variance from Storm and Quiet Interval Distribution	27
2.3.2 Bias and Variance from Orbital Characteristics of the TIMED Satellite	33
2.4 SABER Data Presentation	35
2.4.1 Zonal Mean of Temperature Variation	36
2.5 Extraction of Coefficients of Quiet Time Thermospheric Perturbations	39
2.6 Discussion and Fitting Results	41
2.7 Summary	45

3	SABER TEMPERATURE RESPONSE TO GEOMAGNETIC STORMS	47
3.1	Thermospheric Storm Intervals	48
3.2	Isolation of Storm Response from SABER Measurements	48
3.3	Storm Interval Under Investigation	49
3.4	Morphology of Storm Response	53
3.5	Magnitude and Time Response of the Thermosphere to Geomagnetic Storms	60
3.5.1	Season and Local Time Influence on Thermospheric Storm Response	73
3.6	Summary	75
4	STATISTICAL STUDIES OF THE STORM TIME THERMOSPHERE USING SABER TEMPERATURES	76
4.1	Sample Set for the Statistical Studies	77
4.2	Descriptive Statistics of the Lower Thermosphere Storm Response	82
4.3	Inferential Statistics of the Lower Thermospheric Response to Storms	85
4.3.1	Decision Trees for Storm Response Inference	88
4.4	Importance of Quiet Time Variation in Storm Response Studies	97
4.5	Summary	100
5	COMPARISON OF LOWER THERMOSPHERIC STORM RESPONSE OF SABER, NRLMSIS-00 AND TIEGCM TEMPERATURES	101
5.1	Storm Intervals	101
5.2	Storm Responses	103
5.2.1	Discussion	115
5.3	Summary	118
6	CONCLUSION	119
6.1	Summary	119
6.1.1	Isolating Storm Response from SABER Temperature Measurements	119
6.1.2	Magnitude and Time Response of the Lower Thermosphere to Geo- magnetic Storms	120
6.1.3	Statistical Study of Storm Response	121
6.1.4	Comparison of State-of-art Physics and Empirical Models	122
6.2	Future Work	122
	REFERENCES	125
	APPENDICES	133
	A Coefficients of Quiet Time Variation Model	134
	B T_{ref} Across Various Yaw Cycles and Altitude-latitude Bins.	145
	CURRICULUM VITAE	149

LIST OF TABLES

Table		Page
3.1	Time delay observed across all latitude-altitude bins for the 06-May-2003 storm interval.	68
3.2	Peak response observed across all latitude-altitude bins for the 06-May-2003 storm interval.	69
3.3	Peak response time observed across all latitude-altitude bins for the 06-May-2003 storm interval.	70
3.4	End-of-storm response observed across all latitude-altitude bins for the 06-May-2003 storm interval.	71

LIST OF FIGURES

Figure		Page
1.1	Magnetosphere of the Earth. This image was obtained from NASA Images.	3
1.2	Atmosphere of the Earth. This figure was adapted from the thermosphere figure published in the article <i>A physicist's tour of the upper atmosphere, Physics Today 61(12):70-71, 2008</i> by J. T. Emmert.	5
1.3	Scientific instruments onboard the TIMED satellite. This figure was adapted from the image of TIMED satellite available through NASA Images.	13
1.4	Geo-location of SABER limb measurements made during the course of a single day.	14
2.1	Tracing node traversals made by the TIMED Orbit for a given latitude. . .	20
2.2	Thermosphere Quiet and Active Times during the 2002-2010 Interval. . . .	22
2.3	Yaw cycle intervals.	29
2.4	Thermosphere quiet intervals divided as per yaw cycle intervals.	30
2.5	Beta angle progression of TIMED satellite from 2002-2010.	31
2.6	A schematic to illustrate the principles of our piecewise continuous quiet time variation model.	32
2.7	SABER temperature from both upleg and downleg measurements of latitudes -83° to 53° and altitudes 100 to 120 km corresponding to all the orbits made on a single day. These orbits are from day of year 91 for the year 2010. . .	36
2.8	SABER thermosphere temperature measurements at 110 km for the year 2009. The red points correspond to active times and those in blue correspond to quiet intervals of thermosphere.	37
2.9	Zonal mean of thermosphere temperature variation at 110 km for quiet intervals in the year 2009.	38
2.10	Zonal mean temperature variations at 110 km for quiet intervals in the year 2009 for selected latitudes corresponding to yaw cycles 2 and 3.	40

2.11	Illustration of fitting results for SABER zonal mean temperature vs. quiet time variation model for thermospheric quiet intervals, for selected latitudes of yaw cycle 2 and 3 for altitude bin of 110 km.	42
2.12	Amplitude coefficients of the quiet time variation model calculated from the fit for selected latitudes of 110 km altitudes. The yaw cycle corresponding to the latitudes are noted at the top of the plot.	43
2.13	Phase coefficients of the quiet time variation model calculated from the fit for selected latitudes of 110 km altitudes. The yaw cycle corresponding to the latitudes are noted at the top of the plot.	44
2.14	Illustration of maximum systematic variability derived using our quiet time variation model.	45
2.15	Illustration of maximum random variability derived using our quiet time variation model.	46
3.1	Dst index and Kp index for the 6-May-2003 geomagnetic storm interval. . .	50
3.2	Dst Index and zonal mean temperatures of the thermosphere at the 110 km altitude and -70° latitude bin for the 6-May-2003 storm interval.	52
3.3	Thermospheric storm response at 110 km altitude and -70° latitude for the 6-May-2003 storm interval.	54
3.4	Thermospheric response to May 6th 2003 storm observed at the latitude bins of -70° (left panel) and 50° (right panel). The altitudes, and the local time at which SABER samples the two latitude bins, is noted at the top of the plot.	55
3.5	Thermospheric response to May 6th 2003 storm observed at the latitude bins of -30° (left panel) and 30° (right panel). The altitudes, and the local time at which SABER samples the two latitude bins, is noted at the top of the plot.	55
3.6	Thermospheric response to May 6th 2003 storm observed at the latitude bins of -10° (left panel) and 10° (right panel). The altitudes, and the local time at which SABER samples the two latitude bins, is noted at the top of the plot.	56
3.7	Schematic to illustrate Storm Response Variables.	59
3.8	Temporally smoothed relative Dst index for the May 6, 2003 storm interval, where the relative Dst index corresponds to the the storm time Dst expressed as relative variation with respect to the quiet interval Dst index.	61
3.9	Thermospheric storm response at 100 km altitude and 70° latitude for the 6-May-2003 storm interval. The left and right panels in the figure represent the ascending pass measurements and descending pass measurements respectively. The local time at which SABER samples the latitude bin for the two passes are illustrated at the top of the panels.	61

3.10	Thermospheric storm response at 110 km altitude and 70° latitude for the 6-May-2003 storm interval. The left and right panels in the figure represent the ascending pass measurements and descending pass measurements respectively. The local time at which SABER samples the latitude bin for the two passes are illustrated at the top of the panels.	62
3.11	Thermospheric storm response at 120 km altitude and 70° latitude for the 6-May-2003 storm interval. The left and right panels in the figure represent the ascending pass measurements and descending pass measurements respectively. The local time at which SABER samples the latitude bin for the two passes are illustrated at the top of the panels.	62
3.12	Thermospheric storm response at 100 km altitude and 50° and -50° latitudes for the 6-May-2003 storm interval. The left and right panels in the figure represent the ascending pass measurements and descending pass measurements respectively. The local time at which SABER samples the latitude bin for the two passes are illustrated at the top of the panels.	63
3.13	Thermospheric storm response at 110 km altitude and 50° and -50° latitudes for the 6-May-2003 storm interval. The left and right panels in the figure represent the ascending pass measurements and descending pass measurements respectively. The local time at which SABER samples the latitude bin for the two passes are illustrated at the top of the panels.	63
3.14	Thermospheric storm response at 120 km altitude and 50° and -50° latitudes for the 6-May-2003 storm interval. The left and right panels in the figure represent the ascending pass measurements and descending pass measurements respectively. The local time at which SABER samples the latitude bin for the two passes are illustrated at the top of the panels.	64
3.15	Thermospheric storm response at 100 km altitude and 30° and -30° latitudes for the 6-May-2003 storm interval. The left and right panels in the figure represent the ascending pass measurements and descending pass measurements respectively. The local time at which SABER samples the latitude bin for the two passes are illustrated at the top of the panels.	64
3.16	Thermospheric storm response at 110 km altitude and 30° and -30° latitudes for the 6-May-2003 storm interval. The left and right panels in the figure represent the ascending pass measurements and descending pass measurements respectively. The local time at which SABER samples the latitude bin for the two passes are illustrated at the top of the panels.	65
3.17	Thermospheric storm response at 120 km altitude and 30° and -30° latitudes for the 6-May-2003 storm interval. The left and right panels in the figure represent the ascending pass measurements and descending pass measurements respectively. The local time at which SABER samples the latitude bin for the two passes are illustrated at the top of the panels.	65

3.18	Thermospheric storm response at 100 km altitude and 10° and -10° latitudes for the 6-May-2003 storm interval. The left and right panels in the figure represent the ascending pass measurements and descending pass measurements respectively. The local time at which SABER samples the latitude bin for the two passes are illustrated at the top of the panels.	66
3.19	Thermospheric storm response at 110 km altitude and 10° and -10° latitudes for the 6-May-2003 storm interval. The left and right panels in the figure represent the ascending pass measurements and descending pass measurements respectively. The local time at which SABER samples the latitude bin for the two passes are illustrated at the top of the panels.	66
3.20	Thermospheric storm response at 120 km altitude and 10° and -10° latitudes for the 6-May-2003 storm interval. The left and right panels in the figure represent the ascending pass measurements and descending pass measurements respectively. The local time at which SABER samples the latitude bin for the two passes are illustrated at the top of the panels.	67
4.1	Sample set of the storm intervals, illustrated using geomagnetic indices. The left and the right panel represent the Dst and Kp indices respectively for all the storm intervals, referenced with their respective quiet interval Dst and Kp indices.	77
4.2	Sample set of the storm response across all latitude bins for the 100-120 km altitude range which is used for the statistical study of the thermosphere storm response.	78
4.3	Plotmatrix illustration of the storm predictors constituting our sample set. The plot matrix illustrated here is representation of the 50° latitude-altitude bin.	81
4.4	Illustration of global magnitude response to geomagnetic storms as a function of altitude for each of the four latitude bins. The top panels represent the magnitude response using peak response and the bottom panels using end-of-storm response.	83
4.5	Illustration of global time response to geomagnetic storms as a function of altitude for each of the four latitude bins. The top panels represent time response using delay time and the bottom panels using peak storm response time.	84
4.6	Illustration of categorization scheme for storm response predictors which are employed in the decision tree algorithm investigation of the storm response - storm predictor relationship.	89

4.7	Illustration of categorization scheme for storm response variables used in decision tree algorithm to study the storm response - storm predictor relationship. The latitude-altitude bins corresponding to each of the storm response variables that are illustrated here are labeled at the top of the pie charts.	90
4.8	Decision Tree for delay time classification for 100 km altitude and high latitude bin. The YES and NO represent the presence and absence of time delay. The inhomogeneity associated with each branch is illustrated at the bottom of the branch in red.	92
4.9	Decision Tree for classifying end-of-storm response for 105 km altitude, upper-mid latitude bin. The class YES indicates recovery and NO indicates otherwise. The inhomogeneity associated with each branch is illustrated at the bottom of the branch in red.	92
4.10	Decision Tree for peak response saturation temperature for 110 km and mid latitude bin. The response class of yes indicates saturation and no represent no saturation. The inhomogeneity associated with each branch is illustrated at the bottom of the branch in red.	93
4.11	Decision Tree for peak response for 115 km and low latitude bin. The numbers 1, 2 and 3 represent the three quantiles of the peak response. The inhomogeneity associated with each branch is illustrated at the bottom of the branch in red.	93
4.12	Inhomogeneity of the decision tree response-predictor relationships across all latitude-altitude bins. Each of the four panels represent the four storm response variables.	94
4.13	Inhomogeneity of the decision tree response-predictor relationships using granular data.	96
4.14	Errors in times of storm response from ignoring quiet time variation. The top panels represent the error in delay time and the bottom panels represent the error in peak response time that was seen across various latitude-altitude bins.	98
4.15	Errors in magnitude of storm response from ignoring quiet time variation. The top panels represent the error in peak response and the bottom panels represent the error in end-of-storm response that was seen across various latitude-altitude bins.	99
5.1	Dst index values for the Oct 2008 (left box) and the Oct 2003 (right box) storm intervals. The value of the Dst indices illustrated in this figure are the relative Dst indices which are defined as the relative variation of the storm interval Dst values with reference to the quiet interval Dst index.	102

5.2	Comparison of the SABER, NRLMSIS-00 and TIEGCM response to the Oct 2008 storm for selected latitude bins of 110 km altitude. The local time of the SABER orbit at the storm onset for each of the selected latitude is illustrated at the top of the plot.	104
5.3	Comparison of the SABER, NRLMSIS-00 and TIEGCM response to the Oct 2003 storm for selected latitude bins of 110 km altitude. The local time of the SABER orbit at the storm onset for each of the selected latitude is illustrated at the top of the plot.	104
5.4	Comparison of the Oct 2008 storm response variables computed using SABER, NRLMSIS-00 and TIEGCM for all latitudes of the 100 km altitude bin. In this figure, the thick bars represent the storm response variables deduced from the ascending pass measurements and the thin bars with red outline represent the storm response variables derived from the descending pass. . .	105
5.5	Comparison of the Oct 2003 storm response variables computed using SABER, NRLMSIS-00 and TIEGCM for all latitudes of the 100 km altitude bin. In this figure, the thick bars represent the storm response variables deduced from the ascending pass measurements and the thin bars with red outline represent the storm response variables derived from the descending pass. . .	106
5.6	Comparison of the Oct 2008 storm response variables computed using SABER, NRLMSIS-00 and TIEGCM for all latitudes of the 105 km altitude bin. In this figure, the thick bars represent the storm response variables deduced from the ascending pass measurements and the thin bars with red outline represent the storm response variables derived from the descending pass. . .	107
5.7	Comparison of the Oct 2003 storm response variables computed using SABER, NRLMSIS-00 and TIEGCM for all latitudes of the 105 km altitude bin. In this figure, the thick bars represent the storm response variables deduced from the ascending pass measurements and the thin bars with red outline represent the storm response variables derived from the descending pass. . .	108
5.8	Comparison of the Oct 2008 storm response variables computed using SABER, NRLMSIS-00 and TIEGCM for all latitudes of the 110 km altitude bin. In this figure, the thick bars represent the storm response variables deduced from the ascending pass measurements and the thin bars with red outline represent the storm response variables derived from the descending pass. . .	109
5.9	Comparison of the Oct 2003 storm response variables computed using SABER, NRLMSIS-00 and TIEGCM for all latitudes of the 110 km altitude bin. In this figure, the thick bars represent the storm response variables deduced from the ascending pass measurements and the thin bars with red outline represent the storm response variables derived from the descending pass. . .	110

5.10	Comparison of the Oct 2008 storm response variables computed using SABER, NRLMSIS-00 and TIEGCM for all latitudes of the 115 km altitude bin. In this figure, the thick bars represent the storm response variables deduced from the ascending pass measurements and the thin bars with red outline represent the storm response variables derived from the descending pass. . .	111
5.11	Comparison of the Oct 2003 storm response variables computed using SABER, NRLMSIS-00 and TIEGCM for all latitudes of the 115 km altitude bin. In this figure, the thick bars represent the storm response variables deduced from the ascending pass measurements and the thin bars with red outline represent the storm response variables derived from the descending pass. . .	112
5.12	Comparison of the Oct 2008 storm response variables computed using SABER, NRLMSIS-00 and TIEGCM for all latitudes of the 120 km altitude bin. In this figure, the thick bars represent the storm response variables deduced from the ascending pass measurements and the thin bars with red outline represent the storm response variables derived from the descending pass. . .	113
5.13	Comparison of the Oct 2003 storm response variables computed using SABER, NRLMSIS-00 and TIEGCM for all latitudes of the 120 km altitude bin. In this figure, the thick bars represent the storm response variables deduced from the ascending pass measurements and the thin bars with red outline represent the storm response variables derived from the descending pass. . .	114
A.1	Maximum Systematic and random variation at -70° and 70° latitude in %.	134
A.2	Maximum Systematic and random variation at -50° and 50° latitude in %.	134
A.3	Maximum Systematic and random variation at -30° and 30° latitude in %.	135
A.4	Maximum Systematic and random variation at -10° and 10° latitude in %.	135
A.5	Amplitude Coefficient 1 in %	136
A.6	Amplitude Coefficient 2 in %	137
A.7	Amplitude Coefficient 3 in %	138
A.8	Amplitude Coefficient 4 in %	139
A.9	Amplitude Coefficient 5 in %	140
A.10	Amplitude Coefficient 6 in %	141
A.11	Phase Coefficient 1 in radians.	142
A.12	Phase Coefficient 2 in radians.	143

A.13 Phase Coefficient 3 in radians.	144
B.1 T_{ref} for Yaw Cycle Interval 1 for all latitude-altitude bins.	145
B.2 T_{ref} for Yaw Cycle Interval 2 for all latitude-altitude bins.	146
B.3 T_{ref} for Yaw Cycle Interval 3 for all latitude-altitude bins.	146
B.4 T_{ref} for Yaw Cycle Interval 4 for all latitude-altitude bins.	147
B.5 T_{ref} for Yaw Cycle Interval 5 for all latitude-altitude bins.	147
B.6 T_{ref} for Yaw Cycle Interval 6 for all latitude-altitude bins.	148

CHAPTER 1

INTRODUCTION

1.1 Geospace Environment

The sun is the primary source energy and enables life on Earth. The solar composition is predominantly made up of hydrogen and helium with trace quantities of heavier elements like carbon, oxygen and iron. The energy of the sun is produced through nuclear fusion reactions in the core which is then transported to outer regions through radiation and convection [1, 2]. It has a highly variable magnetic field which is produced by a dynamo action in the outermost layer of the sun, known as its convective zone [3]. The magnetic fields lines originating from the sun can either close back onto it's surface or remain open. The open magnetic field lines act as a conduit for plasma to escape into the interplanetary space. The solar corona is visible during a total solar eclipse and is a major source of X-Rays and UV radiation emitted from the sun. The stream of charged particles released into the interplanetary space by the sun, is referred to as the solar wind [4].

The solar wind is a magnetized plasma consisting of particles and open magnetic field lines originating at the sun and streaming into the solar system. This solar magnetic field embedded in the solar wind is called the interplanetary magnetic field (IMF). The IMF undergoes periodic and episodic spatio-temporal variations which result in a corresponding variation in the solar wind [5]. The spatial-temporal variations include: sudden outburst of energetic particle and radiation through solar flares, transient plasma ejections called coronal mass ejections (CMEs) and high speed solar wind ejected on the open magnetic field lines known as the coronal holes. The high speed streams ejected from the coronal holes can interact with the slow moving solar wind to form a compression region characterized with the intense magnetic fields and high velocities, known as co-rotating interaction regions(CIRs). The solar EUV irradiance is modulated by these solar magnetic field variations. The polarity

of the sun's magnetic field undergoes a major reversal of direction every 11 years which is referred to as solar cycle [6]. It is characterized by a period of intense spatio-temporal variations in the magnetic field known as solar maxima followed by a period of low variance known as the solar minima. The period of solar maxima corresponds to increased CMEs, flares and variations in the solar EUV irradiance. On shorter time scales, the rotation of the sun about its axis results in a 27 day periodicity in EUV radiation, IMF and solar wind.

1.1.1 Magnetosphere

The solar wind interacting with the intrinsic magnetic field of the Earth forms a cavity called the magnetosphere, which tempers the harsh solar wind impinging on the earth [7], [8]. The lack of a strong planetary field and magnetosphere at Mars has been suggested as one reason it has lost much of its atmosphere over its life. The magnetosphere and the terrestrial atmosphere together form the geospace environment. The Earth's magnetosphere, as illustrated in fig. 1.1, exists from about 10 Earth-radii on the Sun-facing side (dayside) and several tens of Earth-radii on the anti-Sun facing side (nightside). The magnetosphere structure is determined by the speed, density, direction, and the magnetic field of the solar wind and hence the magnetosphere structure reflects the periodic and episodic variations of the solar wind.

The solar wind, traveling at supersonic speeds, is slowed as it encounters the Earth's magnetic field to subsonic speeds at the bow-shock. The boundary layer between the solar wind and Earth's magnetic field is called the magnetopause. While the magnetopause shields the Earth, it is far from impenetrable. Energy, mass, and momentum are transferred from the solar wind to the Earth's magnetosphere through the magnetopause. This creates internal structure of currents and plasmas inside the magnetosphere including the plasmasphere, the ring current, and the radiation belts. There is a continual merging and unmerging of the IMF with the Earth's magnetic field called Reconnection, that is continually buffeting the shape of the magnetosphere [9]. Spatial-temporal variations in the solar wind drive processes in the magnetosphere which couple into the Earth's upper atmosphere which collectively we call "space weather" [10, 11]. Geomagnetic storms are one such space

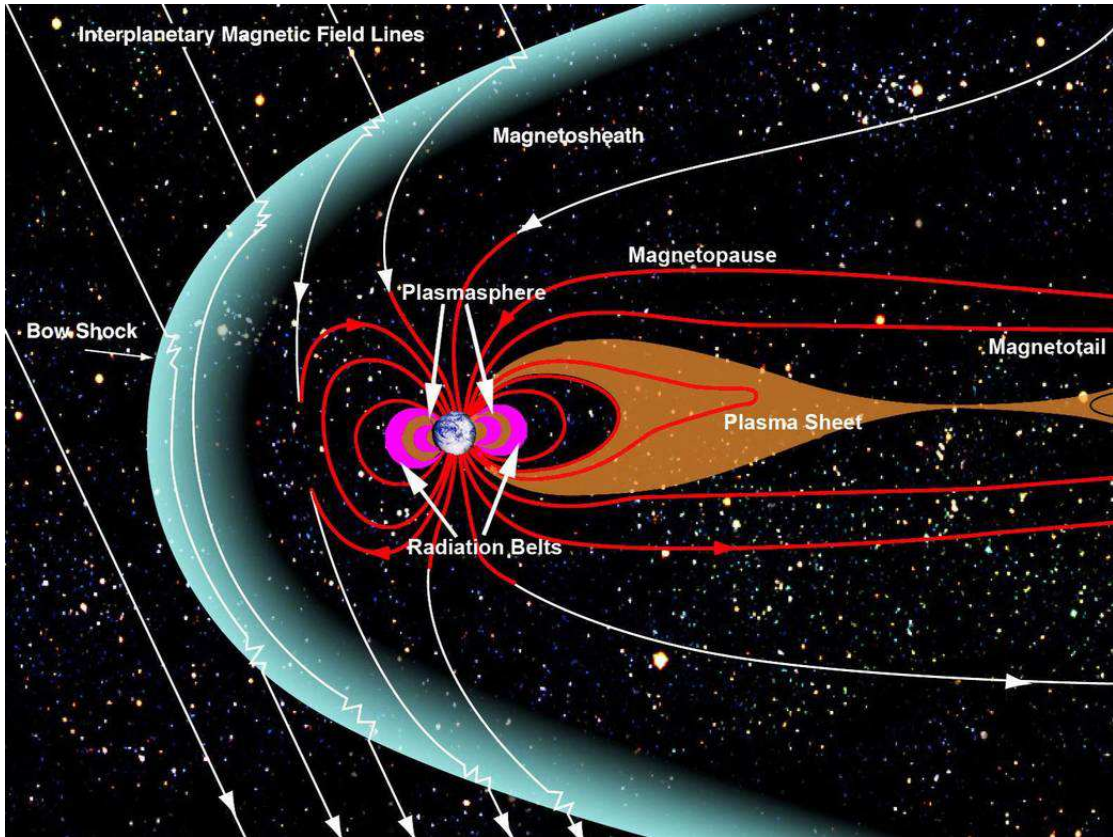


Fig. 1.1: Magnetosphere of the Earth. This image was obtained from NASA Images.

weather event arising from magnetospheric disturbances which in turn result from plasmas and fields ejected from the solar corona that are geoeffective in driving processes such as reconnection [12].

1.1.2 Geomagnetic Storms

Geomagnetic storms occur when the solar wind is moving at high speeds and the IMF is oriented southward for prolonged periods [9, 13]. During such conditions, the IMF merges with the northward oriented geomagnetic field of the Earth at the dayside magnetopause, through the process of magnetic reconnection, injecting particles and energy into the Earth's magnetosphere [5]. This extends the nightside magnetosphere and intensifies the magnetosphere current systems. The magnetic and particle energy of the magnetosphere is subsequently transferred to the Earth's atmosphere through the magnetosphere-ionosphere

currents, and is converted to the internal and kinetic energy of the atmosphere.

The geomagnetic storm is often triggered once the southward component of the IMF weakens and turns northward. The northward IMF weakens or slows the reconnection process causing a reduction in the rate of particles and magnetic energy that is injected into the magnetosphere, which in turn can allow the magnetosphere to suddenly contract to its pre-storm state. The resulting geomagnetic storms are associated with brightening of the aurora and auroral displays at lower latitudes. They are also associated with heating and chemical changes at the Earth's upper atmosphere.

The southward IMF, fast speeds, and density variations of the solar wind can be driven by either a CME or a CIR event. The characteristics of the CME driven storm is markedly different from that of a CIR driven storm [14]. The CIR driven storms are longer marked with slow recovery of the magnetosphere to its pre-storm state and occur during the declining phase of the solar cycle. The coronal holes which trigger the CIR, can persist for multiple solar rotations and cause recurrent CIR driven geomagnetic storms on a 28 day cycle. CME driven storms occur frequently during the solar maximum and are brief and while CIR driven storms are more common during the solar minima.

The occurrence and progression of geomagnetic storms has been discerned by studying the variability of the geomagnetic field [15]. The measured variability of the Earth's magnetic field is a proxy for the variability of current systems in the magnetosphere. A global network of magnetometers that measure the variations and mean geomagnetic field are used to construct indices, which serves as an indicator of the geomagnetic activity. These indices include: Dst index, AE index, Kp Index, PC index etc. [16].

1.1.3 Terrestrial Atmosphere

The atmosphere of the Earth is a thin layer of gases held by gravity that extend from the surface to about 1000 km [17,18]. The terrestrial atmosphere has a vertically differential temperature structure which is used as the basis for classifying the atmosphere [19], as seen in fig. 1.2.

The lowest layer of the atmosphere is called the troposphere and is a highly turbulent

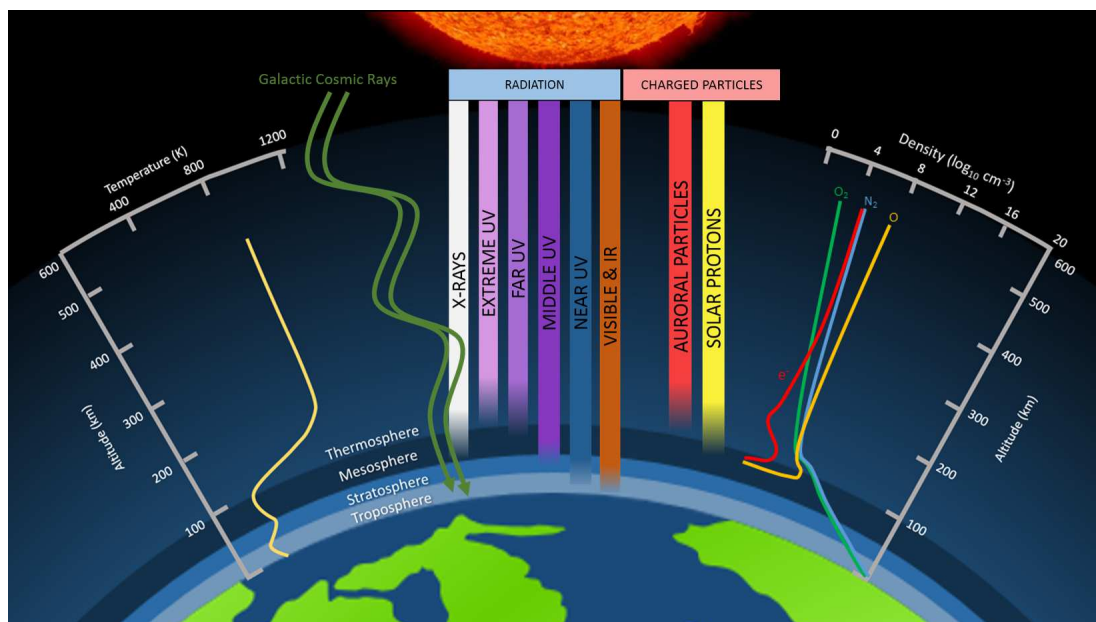


Fig. 1.2: Atmosphere of the Earth. This figure was adapted from the thermosphere figure published in the article *A physicist's tour of the upper atmosphere*, *Physics Today* 61(12):70-71, 2008 by J. T. Emmert.

region, home to most of the terrestrial weather. The upper boundary of this region is about 7-12 km and is referred to as the tropopause. This region absorbs solar radiation in the visible and infrared with maximum absorption occurring at the surface, resulting in a vertically decreasing temperature profile. The atmosphere upwards of the tropopause is a stable region called the stratosphere. This layer extends to a height of about 50 km. It is mainly characterized by the absorption of ultraviolet rays by ozone (O_3). The layer of atmosphere above the stratosphere is termed the mesosphere. It has a decreasing temperature profile due to radiative cooling from infrared emissions of carbon dioxide (CO_2). The upper boundary of the mesosphere, called as the mesopause, occurs at about 90 km and corresponds to the lowest temperature in the entire atmosphere. These three atmospheric layers collectively account for 99% of the atmosphere mass with nitrogen (N_2) and oxygen (O_2) being the major constituents. The relative concentration of N_2 and O_2 is constant throughout these layers resulting in the homogeneity of the mean molecular weight and

giving them a collective name of homosphere.

The region above the mesopause that extends from 90 km to about 600 km is called the thermosphere. Unlike the other three layers, the thermosphere is not homogeneous and the distribution of atmospheric gases is governed by molecular diffusion. This region absorbs solar radiation in the ultraviolet, extreme, far-extreme ultraviolet and x-ray wavelengths which heat the vertically thinning atmosphere, resulting in a vertically increasing temperature profile. In addition to the solar radiation, the thermosphere is also subjected to energy from the particles and plasmas ejected from the sun, via its coupling with the magnetosphere. The incoming radiation and particles from the sun ionize the thermosphere constituents and due to the prevailing low-pressure and the low recombination rate, it gives rise to a permanent population of free ions and electrons in the thermosphere. This ionized part of the thermosphere is called the ionosphere and is characterized by different layers governed by the electron production and loss processes. The region beyond 600 km, called the exosphere, gradually fades into the vacuum of interplanetary space.

1.2 Energetics and Dynamics of Thermosphere

Thermosphere energetics is controlled by the solar irradiance and the solar wind energy that is deposited at high-latitudes by plasma convection and energetic particle precipitation [20]. The solar EUV radiation is the primary source of energy into this region during non-geomagnetic storm times. It interacts with the major constituents: N_2 , O_2 and O , through photodissociation and photoionization [21]. The solar wind coupling with the Earth's magnetic field in the magnetosphere generates electric fields and current systems. Some of these currents flow into the ionosphere along the magnetic field lines to form a magnetosphere-ionosphere current system. The charged particles comprising these currents collide with the neutrals and impart energy and momentum into the thermosphere in a process called Joule heating. Plasma instabilities growing off the free energy of these currents create a minority population of highly energetic particles. These precipitating charged particles ionize, dissociate and excite the neutral particles and thereby release further magnetosphere energy into the thermosphere in the due process.

The thermosphere is also subjected to energy and momentum through tides and gravity waves propagating from the lower atmosphere [22]. The absorption of solar irradiance by the atmospheric constituents like H_2O , O_3 , O_2 in the troposphere, stratosphere and thermosphere generates thermal tides. They are harmonics of the solar day and grow exponentially as they travel upwards into the thermosphere. In addition, there are perturbations due to gravity waves or buoyancy waves generated in the troposphere by volcanoes, thunderstorms and wind flowing over mountains. These waves again carry energy and momentum into the thermosphere. They interact with each other and with the mean flow, dissipating energy and momentum as they break throughout the thermosphere.

The main energy sinks in the thermosphere are downward heat conduction and radiative cooling. The energy and momentum from the lower atmosphere and the direct energy and momentum deposition through solar wind and EUV are globally transported throughout the thermosphere by advection, convection and conduction, giving a distinct latitude, longitude and altitude structure to the thermosphere [23].

The energy from solar irradiance and solar wind are both highly variable in space and time and imprint a corresponding variation in the thermosphere structure [24, 25]. The variation in solar irradiance is seen as the day-night, seasonal and solar cycle variations in the energy deposited throughout the atmosphere.

The thermosphere is also subjected to variations resulting from Joule heating and particle precipitation due to geomagnetic storms following solar events like CMEs and CIRs. This episodically dumped energy results in increased advection, convection, conduction, chemical and composition changes. This increase during geomagnetic storms, can sometimes overtake the EUV as the dominant source of energy in the thermosphere [26]. Most of this solar wind energy converges in the lower thermosphere region between 100 - 160 km [27]. These episodic energy outbursts from geomagnetic storms are of particular interest since they cause significant change in the global structure of the thermosphere-ionosphere system within a few hours of occurrence [28].

1.3 Thermosphere Response to Geomagnetic Storms: Current Understanding

The impact of geomagnetic disturbances on the Earth's neutral atmosphere was first noticed by Jacchia in his observations of orbital element changes of the Sputnik III satellite [29]. When analyzing the changes in the orbital elements of the Sputnik III satellite, he discovered an anomalous deceleration during a geomagnetic storm. He attributed this acceleration to an increase in the atmospheric density caused by upper atmospheric heating. Since then, more than 500 studies have been published on the topic of thermosphere-ionosphere changes and behavior during geomagnetic storms [30], all of which have led to the general consensus that a global change in energetics and dynamics of the thermosphere occurs due to the input of geomagnetic storm energy.

The bulk of the existing knowledge about thermospheric response to geomagnetic storms comes from studies of mass density measurements derived from satellite drag [31] at orbital altitudes (400 - 1000 km). Some notable studies include SETA, CHAMP and GRACE satellite observations, which have provided insight into the spatial and temporal changes associated with global mass density response to storms [32–36]. These observations have attributed a mass density hike at the orbital altitudes, pole-to-pole, ranging anywhere between 50% - 800%, with respect to pre-storm density. These studies report that at high latitudes, there is an almost immediate response while the response at equatorial latitudes exhibits a 2 to 7 hours time lag from the injection of storm energy. These orbital altitude studies of mass density along with the observations of cross-track winds from accelerometers, have also led to the observation of small and meso-scale wave structures, in addition to large gravity waves, which transport storm energy from auroral zones toward the equator [36–38]. A few other studies have attributed large-scale circulation changes to be the source of equator-bound energy they observed [39]. However, the relative importance of these two transport mechanisms under various conditions are yet to be established [40].

These studies based on satellite drag have led to a gross understanding of the storm response, in terms of providing an average expected density response at orbital altitudes. However, we do not yet completely understand the drivers of these changes observed at

orbital altitudes and the underlying processes affecting these changes.

In addition to *in situ* heating, the storm induced mass density changes measured at orbital altitudes arise due to barometric expansion from localized heating at the lower altitudes and due to vertical winds transporting constituents between pressure levels. Although, *in situ* heating at the orbital altitudes is the major contributors to the mass density changes observed at the orbital altitude, localized heating at altitudes below 150 km are also responsible for shaping the orbital altitude mass density [41,42].

It was shown by Lei et al., that the vertical wind effects and temperature effects cannot be deconvolved from studying mass density changes at fixed orbital altitudes [43]. This is due to the changing scale heights and associated composition and temperature changes below the fixed altitude. Hence it is essential that we study the temperature and wind profiles across the thermosphere to understand the orbital altitude storm response in entirety.

Temperature measurements are limited in number, especially at altitudes lower than 150 km. The current understanding of lower thermospheric heating at the 90-150 km altitudes, during storms, mostly comes from localized ground based temperature measurements and sounding rockets, all of which have attributed a 80-200 K storm energy increase in temperatures [40]. Investigation of HITS instrument temperatures onboard the ARGOS satellite reported similar temperature changes and up to 16 hours of delay for storm energy to converge at the equatorial latitudes [44].

Studies of high speed stream effects on lower thermosphere data [45,46], and NO cooling post-storm phase [47] carried out at these lower altitudes have contributed to understanding of the thermospheric expansion and contraction due to external solar wind forcing. However, an exhaustive study of temperatures of the lower thermosphere under storm conditions on a global scale, is absent from the literature. The insufficiency of knowledge with regard to thermospheric storm response is not limited to the thermospheric state variables alone. The knowledge of the interplay of solar EUV and storm energy during geomagnetic storm in influencing the thermosphere response is also currently lacking.

Studies of global response of mass densities have highlighted the difference in responses

to storm energy at summer and winter hemispheres and between day and nightside for the same storm [32–35]. Similarly, using first principle models, Burns et al. showed the difference in the storm response during winter and summer to vary differently for solar maximum and minimum conditions [48]. Similarly, Liu and Luhr investigated day *vs.* night for winter and summer hemispheres for closely spaced storms using CHAMP data [49]. They found the response to exhibit similar multifaceted variations that were functions of the competing process of seasons, local time and storm intensities. In addition, the duration of the storm, the local time at the instigation of storm impulse and longitudinal effects have all been invoked to explain the various features of storm response that seem to vary amongst all the case studies [30]

The atmospheric storm response is hence believed to be a combination of various effects such as seasons, solar cycle, local time, pre-storm conditions, storm intensity and storm duration. These observations highlight the necessity of accruing more than a few scattered case studies and building a systematic statistical database of storm response observations, which can qualify each of the competing factors.

Statistical studies of the thermosphere have been rare due to the absence of long-term missions. Yet, long term data sets from the CHAMP, GRACE and TIMED satellites are now available and studies of mass density response to CME *vs.* CIR storms [50], effects of high speed streams [51], local time effects for quantifying corrections to empirical models [52] have been explored on a statistical scale.

1.4 Dissertation Objectives

The scientific community has limited knowledge of the lower thermospheric heating process during geomagnetic storms. As elaborated earlier, it is essential we advance our knowledge on this matter to explain the storm-driven changes at orbital altitudes. In addition, several factors like season, solar cycle, storm intensity etc. are nested within each other and they collectively qualify the expected storm response. Hence it is essential to conduct a statistical study of storm responses to obtain an understanding of thermospheric storm response.

We aim to fill this gap by studying the global temperature changes in the lower thermospheric region across all latitudes for a period close to a decade. This statistical study would be the first of its kind in advancing our knowledge of the thermosphere storm response in terms of temperature. We will evaluate the state of our current empirical and first principle models in reproducing these storm effects to take stock of the current situation and to make recommendations for future studies. The objective of this dissertation is to advance our current understanding of the lower thermosphere response to storms, by answering the following questions:

- What are the magnitudes of the temperature increase seen across the lower thermosphere following a geomagnetic storm?
- What are the time scales for the storm energy to be transported globally?
- How do the solar cycle, seasons, local time and type of storm influence the storm response?
- How do the state-of-art physics based models and empirical models fare in replicating the lower thermosphere storm response?

1.5 Importance of the Dissertation Objectives

Geomagnetic storms can dump gigawatts of energy and completely alter the state of the thermosphere [26]. This causes dramatic changes in satellite orbits, produces currents in power grids and pipelines, and affects communication and navigational satellite systems as a result of the changes in the ionized atmosphere. In the era of ever increasing number of space-faring nations, our atmosphere is getting heavily crowded with satellites and any change in their orbits, if not accounted-for, risks potential collisions and increasing the space debris [53]. This problem is expected to be catastrophic with the scare of the orbital altitudes eventually becoming unfeasible for space activities and satellites - “Kessler’s syndrome” [54].

The largest source of uncertainty in the orbital predictions made from semi-empirical models stems from storm-driven changes in satellite drag [55]. These empirical models are driven by mass density, temperature and wind observations and their interconnections. As explained earlier, explaining mass density changes requires us to understand the lower thermosphere temperature changes. Understanding the neutral atmosphere heating is essential for understanding the corresponding changes in the coupled ionosphere. This understanding is essential in preventing storm-driven outages of our communication and navigation systems. In a technology-dependent society, any of these above mentioned storm effects would be catastrophic and could potentially cripple modern technological life on this planet [56]. Hence temperature response to storms in lower thermosphere is highly pertinent to improving our empirical models and reducing uncertainty in satellite orbits and in turn understanding how to safe-guard our technology-driven societal needs.

1.6 Methods

The first measurements of the terrestrial atmosphere were made by balloons followed by radars and sounding rockets and then eventually using satellites since the 1950s. Initial measurements of the thermosphere were made by deducing density from the changes in satellite orbital elements. This was succeeded by measurements of winds, temperatures and composition by missions like Atmospheric Explorer and Dynamic Explorer. The advent of satellite missions tremendously increased our knowledge of global atmosphere characteristics. However, these missions were short-termed with limited spatial sampling. It was only in the early 21st century that the launch of satellites like CHAMP, GRACE and TIMED that we came into possession of global coverage and long term data sets of the atmospheric state variables.

1.6.1 SABER Temperature Data

The TIMED mission, where TIMED stands for - Thermosphere, Ionosphere, and Mesosphere Energy Dynamics, was launched in December of 2001 and has been operational to-date [57]. The mission was launched with the science objective of remote sensing of the

Mesosphere Lower Thermosphere Ionosphere (MLTI) state variables and energy inputs and outputs from 60 to 180 km [58]. The lower thermosphere region sampled by TIMED corresponds to the region of convergence of solar wind energy. The global coverage of TIMED and the presence of science data over a decade commends it for advancing our knowledge of global energy redistribution during geomagnetic storms. It has four science instruments, illustrated in fig. 1.3 [59], which are:

- Global UltraViolet Imager (GUVI) - provides composition and electron density data.
- Solar Extreme ultraviolet Experiment (SEE) - measures the energy being input and output of the MLTI region by measuring solar irradiance in X-ray, EUV and FUV.
- TIMED Doppler Interferometer (TIDI) - measures horizontal winds.
- Sounding of the Atmosphere Using Broadband Emission Radiometry (SABER) - provides kinetic temperature, pressure, heating and cooling rates of thermosphere neutrals.

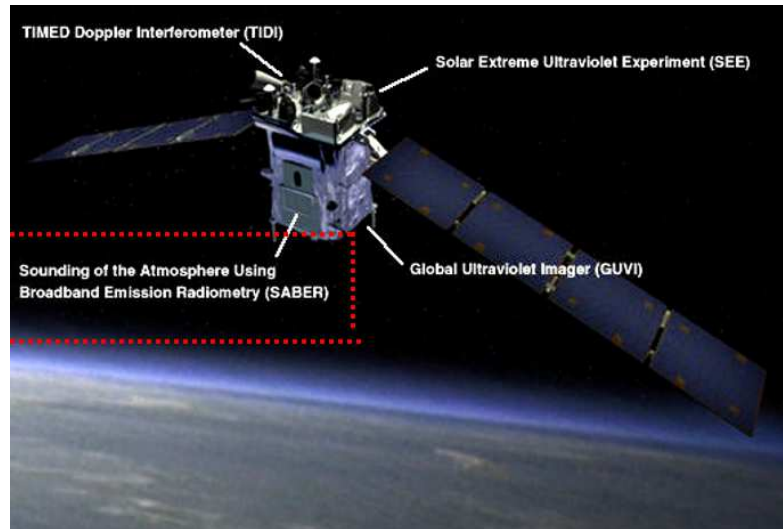


Fig. 1.3: Scientific instruments onboard the TIMED satellite. This figure was adapted from the image of TIMED satellite available through NASA Images.

The TIMED satellite has an orbital altitude of 625 km, inclination of 73° , and orbital period of about 95 minutes. The local time crossing at the equator drifts by about 12 minutes every day. The instrument makes measurements on both upleg and downleg of the orbit. The upleg and downleg of the orbit are at different local times and a cumulative coverage of close to 22 hours is achieved in 60 days. The viewing geometry alternates every 60 days due to a 180° yaw maneuver performed by the TIMED satellite to keep the thermal radiator surfaces away from the Sun. This viewing geometry limits the latitudinal coverage to 83° S to 53° N or 53° S to 83° N depending on the yaw cycle. We plot the geographical and local time coverage of a typical orbit of TIMED over a period of a day is shown in fig. 1.4. The orbits illustrated in fig. 1.4 are the geo-spatial footprints of the observations made

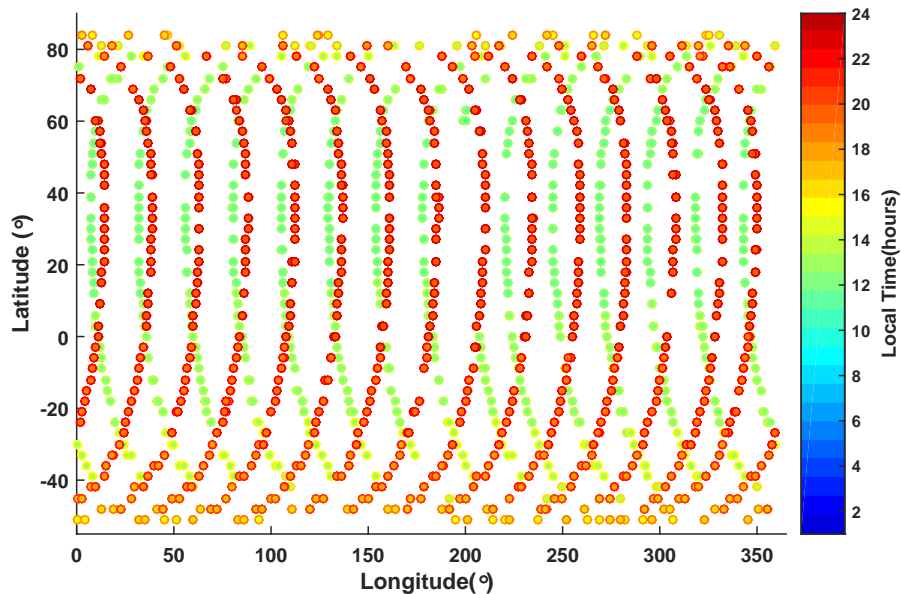


Fig. 1.4: Geo-location of SABER limb measurements made during the course of a single day.

on day 97 of year 2009(2009097) for tangent altitude of 80 km. The orbital parameters of the satellite were chosen to “freeze” the Earth viewing geometry on an annual basis to yield annually synoptic measurements and thus facilitating long-term and climatic objectives [60].

Essentially, TIMED returns to sample exactly the same latitude coordinated on the same calendar day a year later, at about the same local time.

The SABER instrument is an infrared spectrometer measuring limb emission with a spectral range from $1.27\mu\text{m}$ to $17\mu\text{m}$. These emissions are analyzed to provide vertical profiles of volume emission rates of oxygen (O_2), carbon dioxide (CO_2), nitric-oxide (NO) and hydroxide (OH^-) and vertical profile of kinetic temperature. The vertical profile of kinetic temperature from ground up till 140 km of altitude is derived from CO_2 emissions in the $15\mu\text{m}$ channels using nonlinear thermodynamic equilibrium (NLTE) algorithms as described in Mertens et al. [61]. However, diminishing signal and uncertainties with temperature retrieval above 110 km altitude have limited the altitude range of SABER temperature use. The uncertainties in SABER temperatures result from uncertainties in atomic oxygen density, errors in CO_2 mixing ratio and quenching rate. The extent of these errors have not been well-validated above 110 km due to lack of recurrent measurements [62] with the sole exception being the comparison of limited profiles of RAIDS and SABER temperatures by Christensen et al. [63]. They found SABER to match with RAIDS reasonably well until about 110 km with increasing differences at higher altitudes that reach as high as 30 K. However several studies using version 1.07 of SABER temperature data that span years of data have been conducted using data up to 120 km and no unexpected or unusual behavior in temperatures have been reported [64–67]. Hence in this study we use temperatures of 100 - 120 km altitudes. The version of data used here is 1.07 and is obtained from the online repository of SABER data, maintained by GATS Inc. [68]. We use the data from the years 2002 to 2010 for conducting our statistical storm response study.

1.6.2 Proxies for Geomagnetic Storms

The occurrence and progression of geomagnetic storms can be studied using geomagnetic indices [69]. In our study, we use Dst and Kp indices to identify the storm occurrences and their progression.

The Dst index stands for disturbance storm time index and is a measure of the average value of the horizontal component of the Earth’s magnetic field, measured hourly at

near-equatorial geomagnetic observatories. The strength of the magnetic field at low latitudes is inversely proportional to the energy content of ring current which increases during geomagnetic storms and hence serves as a proxy for geomagnetic activity.

The Kp index is a quasi-logarithmic index, derived from deflection of horizontal components of the Earth’s magnetic field. It is measured from 13 geomagnetic observatories between 44 degrees and 60 degrees northern or southern geomagnetic latitude. Both geomagnetic indices are obtained from the online repository maintained by the World Data Center for Geomagnetic Data, Kyoto [70].

1.6.3 Thermospheric Models

The data obtained from several space and ground based techniques have often been used to construct data-driven or semi-empirical models that use measurements supplemented with first principles (in the case of missing observations), to represent the atmosphere. In addition, several physics models which are entirely first principles based, are also used to study the atmosphere. In this study we assess the degree to which NRLMSIS [71] and TIEGCM models [72], which are widely used [73] in the heliophysics community, represent thermospheric storm response.

NRLMSIS model, where NRL stands for US Naval Research Laboratory and MSIS stands for Mass Spectrometer and Incoherent Scatter radar model is an empirical model widely used for predicting state variables of the terrestrial atmosphere [71]. As the name suggests it was initially built from the long-term collection of mass spectrometer and scatter radar measurements along with the more recent drag observations. In this work, we have used NRLMSIS-00 version of this model.

The Thermosphere-Ionosphere-Electrodynamics General Circulation Model (TIEGCM) is a comprehensive, first-principles, three-dimensional, non-linear representation of the coupled thermosphere and ionosphere system developed at National Center for Atmospheric Research [72]. The model solves the three-dimensional momentum, energy and continuity equations for neutral and ion species at each time step, using a semi-implicit, fourth-order, centered finite difference scheme, on each pressure surface in a staggered vertical grid. It

has 29 constant-pressure levels in the vertical, extending from approximately 97 km to 500 km and a 5° latitude by 5° longitude geographic grid. The solar flux inputs are parameterized by F10.7 index, particle precipitation by hemispheric power and the diurnal and semi-diurnal tides by Global Scale Wave Model. The high latitude electric fields can be set using either empirical high latitude models like Weimer model and Heelis model, using data from AMPERE satellite or via means of data assimilation. In this work, the Weimer Model has been used to parameterize the electric field of the high latitudes. Version 1.95 of TIE-GCM model has been used here.

The TIE-GCM model temperatures were obtained by requesting model runs through the Community Coordinated Modeling Center (CCMC) online tool [74]. The NRLMSIS-00 model temperatures were obtained by running the MSIS models available in the MATLAB aerospace toolbox.

1.7 Outline of Dissertation

The chapters following this introductory section are organized into five different sections to provide closure to the objectives of this dissertation.

One of the important steps in conducting this study is to conceptualize a procedure that would isolate the storm response from SABER temperature measurements. The lower thermosphere is often perceived as a shoreline region, home to waves and tides dissipating energy and internally forcing the thermosphere. When measurements from an asymptotic platform such as SABER temperatures are used, these variations could be intertwined with the storm response. We derive a methodology for isolating storm response from SABER measurements in Chapter 2.

We use this methodology derived in Chapter 2 to discern the storm response for a storm interval in Chapter 3. It serves as a case study for detailing the procedure of deriving magnitude and time response of storms. We use these methods from Chapter 2 and 3 to build a decade worth of storm response database in Chapter 4. We use this database of storm response to conduct inferential and descriptive statistical studies on the thermosphere storm response. In Chapter 5, we compare state-of-art thermosphere models with the storm

response findings from satellite data. Finally, we conclude this work by summarizing our findings and making recommendations for future studies.

CHAPTER 2

QUIET TIME VARIATION IN THE LOWER THERMOSPHERE

The process of evaluating the thermospheric response to geomagnetic storms involves isolating differences from its base state (quiet time). Based on the phase of the solar cycle and the length of the storm, the separation between the thermosphere being in its base state and being disturbed due to the geomagnetic storm, can be a few hours to a few days. Separation of a few days or more, could arise from back-to-back geomagnetic disturbances (storms) seen during solar maxima that prevent the thermosphere from setting back to its base state or slow recovery storms that arise from high speed streams and coronal holes during solar minima [75].

Satellites are often favored to observe global phenomena such as geomagnetic storm response. However, evaluating the storm response using satellite data would require us to compare the data collected by the satellite when the thermosphere was in its base-state (quiet interval) with that of the data collected during a geomagnetic storm interval. Such a comparison is not straightforward and taking the difference between the storm interval data and the quiet interval data will not suffice. This is because, based on the satellite orbit and the interval of separation, changes arising from other geophysical phenomena would be convolved along with the storm response in such a difference.

In our study, we use data from the SABER instrument onboard the TIMED satellite, to study the response of the thermosphere to geomagnetic storms. TIMED is an asynchronous satellite with an inclination of 74.1° . Although it provides the advantage of global and near polar-to-polar coverage, it does not return to the same geographic location till the next day and hence provides asynoptic data. This is further compounded with the fact that the satellite orbit is also non-sun-synchronous and hence makes non-integer orbits in a day, resulting in the local time drift of the orbit over time.

To trace the node traversals, we defined a variable, Ω_γ for each latitude θ sampled along

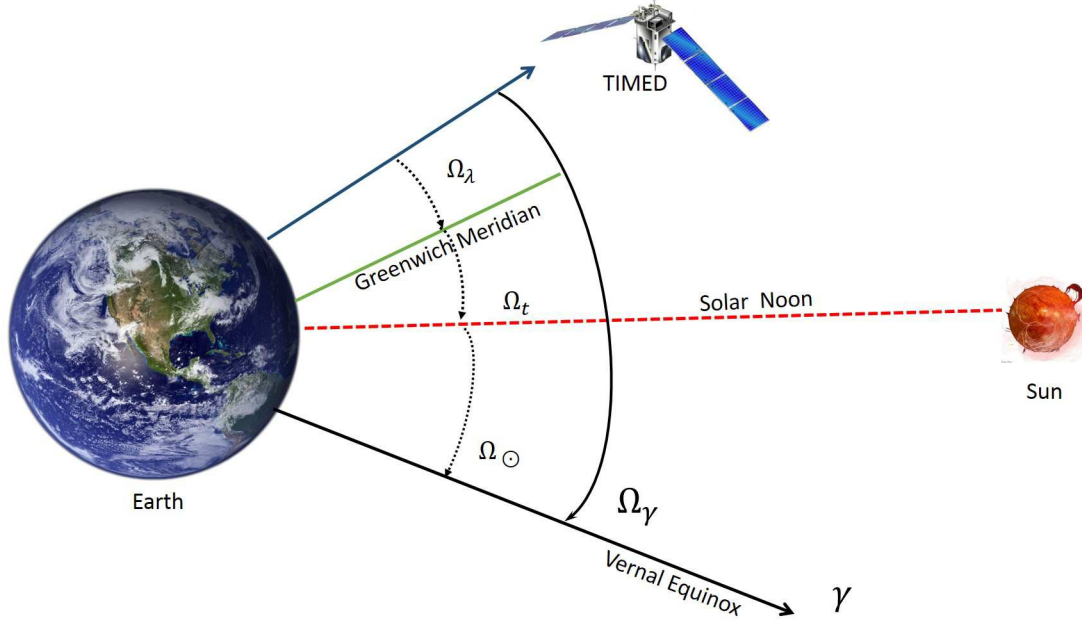


Fig. 2.1: Tracing node traversals made by the TIMED Orbit for a given latitude.

the satellite's orbit as illustrated in fig. 2.1. The satellite scans through range of altitudes along the limb direction for each node. Hence the temperature observations $T(\theta, z, \Omega_\gamma)$, made along the path of the TIMED satellite orbit, can be traced using Ω_γ , for each latitude θ and altitude z .

The variable Ω_γ is the orbital angle, that has been defined in the inertial equatorial coordinate system and is the angle made by the satellite with the vernal equinox line on the equatorial plane of Earth. This coordinate system was chosen due to the convenience of being able to describe the progression of both the satellite and the Earth's orbital periods.

Since the satellite's orbital period is not synchronized with the Earth's rotation, the progression of the orbit has been expressed as the differential progression of universal time and the longitude of the observation point, with respect to the solar noon. The progression of the orbit of the TIMED satellite is hence given by the combination of Ω_t and Ω_λ . $\Omega_t = \omega_t t$ where, $\omega_t = \frac{2\pi}{24}$ and t is the time in hours. $\Omega_\lambda = \omega_\lambda \lambda$, where $\omega_\lambda = \frac{2\pi}{360}$ and λ is the longitude progression since local noon.

To account for the progression of the solar noon due to the Earth's orbit around the

Sun, we define the angle Ω_{\odot} as shown in fig. 2.1. Its progression is determined by the progression of solar days, $\Omega_{\odot} = \omega_{\odot}d$, where, $\omega_{\odot} = \frac{2\pi}{365}$ and d is the day of solar year.

Therefore, based on the progression of Ω_{γ} , the observations made by TIMED will vary as a function of the solar local time progression, solar day progression or both. Any geophysical phenomenon that occur as a function of solar day and solar local time could hence be intertwined in the measurements made along the TIMED orbit. In this chapter, we derive a methodology to identify and isolate such non-storm geophysical phenomenon contributions from the measurements made along the TIMED orbit.

2.1 Thermospheric Quiet Times

Before we define a methodology to isolate quiet times, we need to describe what intervals are classified as quiet intervals in the thermosphere. The strength of geomagnetic activity in the magnetosphere is discerned from the magnitude of the geomagnetic indices [69]. These geomagnetic indices, however, cannot be used on a one-to-one basis for representing thermospheric quiet conditions [76]. This is due to the time delay exhibited by the thermosphere in responding to the external forcing from the magnetosphere. This sluggish response and hence a corresponding sluggish recovery with respect to the forcing from geomagnetic activity, is called the “memory effect” [77, 78].

This time delay is particularly large in the lower thermosphere (90 - 140 km) which is more massive than orbital-altitude-thermosphere (400 - 1000 km) and hence exhibits larger inertia to external forcing. Although, we do not have enough lower thermosphere measurements to discern a suitable time lag for representing the memory effect as a factor of different geomagnetic activity strengths, most thermosphere case studies have attributed 10-15 hours of time lag to intense geomagnetic activity [38, 79, 80]. Hence, the thermospheric recovery back to base state would involve atleast 10-15 hours after the geomagnetic index at quiet levels. Hence we have defined thermospheric quiet intervals as quiet intervals with a history of 24 hours of quiet geomagnetic activity in the magnetosphere, as determined by the geomagnetic index.

In this study, we have used the Kp index for separating the magnetospheric quiet and

active conditions. Kp index derived from the horizontal component of Earth's magnetic field measurements have values ranging from 0 to 9 to represent the various degrees of geomagnetic activity. The magnetospheric quiet conditions that correspond to negligible geomagnetic activity are identified as intervals which have Kp Index < 3 [81]. The magnetospheric active conditions correspond to Kp Index > 2 with disturbed or storm conditions causing the Kp Index to rise upwards of 4 for extended periods of times. Hence thermospheric quiet intervals are those which correspond to Kp index being less than 3 and being preceded by 24 hours of Kp being less than 3.

The interval of 2002 to 2010 that has been used in our study has been divided into thermospheric quiet and active times based on the classification described above. The break-up of the interval into quiet and active thermospheric times is illustrated in fig.2.2. As seen in fig. 2.2 the year 2009 has the highest percentage of quiet days in a given calendar year.

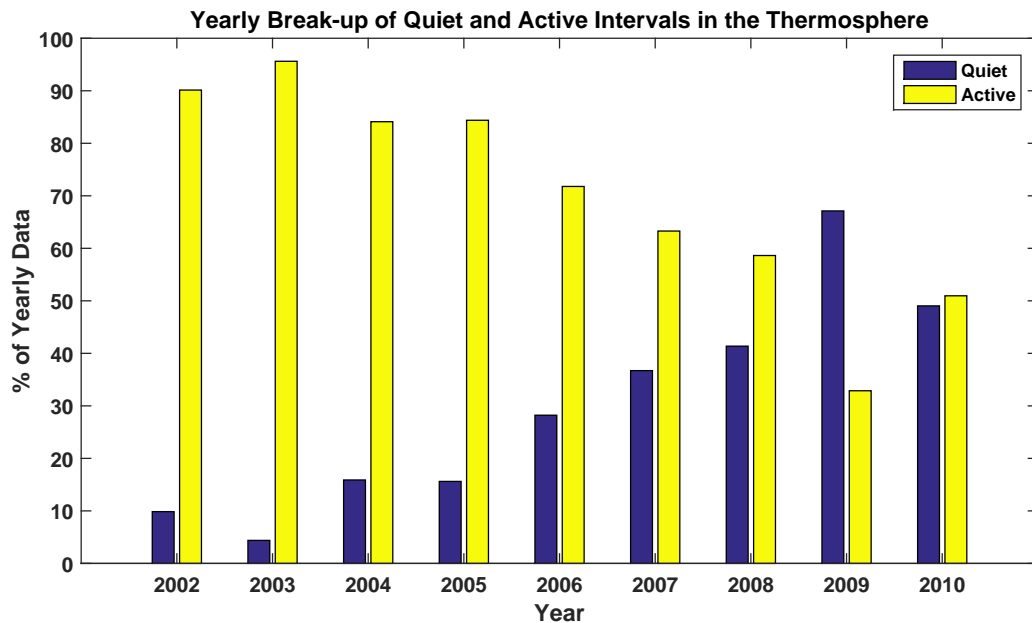


Fig. 2.2: Thermosphere Quiet and Active Times during the 2002-2010 Interval.

One of the objectives of this study is to deduce response and recovery times of the lower

thermosphere to various geomagnetic activity conditions. These findings could be used to suitably revise the 24 hours interval that has been used here for representing the memory effect in future studies.

2.2 Thermospheric Quiet Time Variations

The thermosphere is subjected to a plethora of spatial and temporal perturbations that convolve with one another and collectively set the state of the thermosphere. In this study, we are isolating all such perturbations that are of non-storm origin and are functions of solar day and solar hours. These perturbations are cyclic in nature and can hence be represented as cosine functions that are harmonics and sub harmonics of solar days and solar local time. The Earth's axial tilt and the vertical atmosphere structure result in these temperature perturbations to be defined for each latitude (Θ) - altitude (z) of a geographic grid. In the next section, we present models for each of these major components.

2.2.1 Solar Wind Variation

The solar wind interacts with the Earth's atmosphere in the form of particles that precipitate along the Earth's open magnetic field lines. The heating of the auroral region due to this particle precipitation and the accompanying Joule heating has been observed to imprint a longitudinal variation of the zonal mean state of the thermosphere [66]. We express the resulting temperature perturbation, T_g , as

$$T_g(\Theta, z, \lambda) = T_{0g} + \sum_w j_w \cos(w\Omega_\lambda - \zeta_w), \quad (2.1)$$

where, T_{0g} is the daily mean geomagnetic activity term and j_w and ζ_w are the amplitude and phase of the w harmonics of the geomagnetic activity.

2.2.2 Tidal and Wave Variability

The solar flux variation over local time of a day and its absence in the night results in oscillations of periodic nature called solar thermal tides or solar tides [82]. They are

excited due to periodic solar flux absorption by water, oxygen and ozone molecules in the troposphere and stratosphere. These oscillations propagate to higher altitudes, growing exponentially with height. The eddy diffusion and molecular dissipation in the mesosphere-lower-thermosphere region, between 80 to 150 km, cause the dampening of these tides. This causes them to achieve maximum amplitudes in the MLT region and dominate the metrology of this region [83]. When viewed from an Earth fixed frame, they trace the apparent motion of the sun and are hence called migrating tides. These apparent westward moving oscillations include a 24 hour component as well as sub-harmonics of a solar day such as 12 hours, 8 hours and 6 hours. [64].

These oscillations are further modulated by land-sea differences, and resulting convective activity differences across longitudes, giving rise to longitudinally varying oscillations called non-migrating tides [84, 85]. In addition to this, global-scale oscillations due to a rotating atmosphere around a planet result in longer period oscillations called planetary waves which are integral harmonics of a solar day [86, 87]. Similar to tides, these waves also exhibit longitudinally modulated harmonics. We write these tidal and wave variations seen as harmonics of a solar day, T_{tw} , as follows:

$$T_{tw}(\Theta, z, \lambda, t) = T_{0_{tw}} + \sum_p \sum_q b_{pq} \cos(p\Omega_t + q\Omega_\lambda - \beta_{pq}) \quad (2.2)$$

where, $T_{0_{tw}}$ is the daily mean term, b_{pq} and β_{pq} are the amplitude and phase of the oscillations with frequency, p and wavenumber q . The case of $q = 0$ corresponds to migrating tides and waves in equation (2.2). The eastward moving non-migrating tides have a negative wave number, while the positive wave number denotes westward moving non-migrating tides and waves.

When tides and waves are measured using satellites, the ability to differentiate between the wavenumbers and temporal frequencies depends on the orbit. In a sun synchronous orbit, the satellite is locked in phase with the sun ($\omega_t = \omega_\lambda$) and hence the variations seen by the satellite cannot be resolved into spatial and temporal frequencies. Hence sun-synchronous orbits are not favored to study tides and waves.

In the case of non-sun-synchronous orbits, due to the non-integer number of orbit completions in one solar day, the local time sampled at a given location precesses day to day. When data from such an orbit is collected over a period of time corresponding to 24 hours of local time precession, we will have measurements along the entire phase of the local time and across all longitudes and hence the observed variations can be resolved into temporal and spatial frequencies. The highest frequency (p) and wavenumber (q) of tides and waves that can be discerned from such non-sun-synchronous satellite measurements are deduced using Salby's Nyquist limit for asymptotic sampling [88]. It has been deduced that zonal wavenumbers and frequencies from 0 up to 6 can be resolved for measurements made along the TIMED orbit [89]. In addition, the planetary waves with frequency up to 1 and zonal wavenumbers up to 6 can be resolved [90].

In the lower thermosphere, the tidal waves with frequency up to 3 - diurnal, semi-diurnal and terdiurnal tides, are usually deemed as important along with their corresponding eastward and westward components up to wavenumber 6 [91]. The planetary waves with frequencies $\frac{1}{5}$, $\frac{1}{8}$, $\frac{1}{11}$, $\frac{1}{24}$ are found to contribute to thermosphere variability [86, 87].

Seasonal Variation

The thermosphere exhibits variations which are sub-harmonics of a year or one revolution of the Earth around the Sun [92]. Increasingly well-mixed, large-scale circulation during solstice, seasonal variation of eddy diffusion all have been invoked to explain the mechanisms triggering the seasonal perturbations in the thermosphere state variables [93]. We express the thermosphere temperature variations on the seasonal scale as:

$$T_y(\Theta, z, d) = T_{0_y} + \sum_n s_n \cos(n\Omega_{\odot} - \eta_n), \quad (2.3)$$

where, T_{0_y} is the yearly mean term and s_n and η_n are the amplitude and phase of the n harmonics of the yearly mean term.

2.2.3 Solar Cycle Variations

The solar flux in the EUV range is the primary heating source of the thermosphere during quiet time. The solar flux varies due to solar rotation, solar cycle effects and due to variation in solar insolation from rotation and revolution of the Earth. The solar cycle variations which are harmonics of 11 years, cause larger variation in temperature than the shorter solar rotation driven 27 day harmonics [24]. The perturbation caused in the temperature due to solar flux variations, T_{EUV} , is defined as

$$T_{EUV}(\Theta, z, d) = T_{0EUV} + \sum_m a_m \cos\left(\frac{m\Omega_{\odot}}{11} - \alpha_m\right), \quad (2.4)$$

where, T_{0EUV} is the solar cycle mean term and a_m and α_m are the amplitude and phase of the m harmonics of the 11 year solar cycle. The solar cycle harmonics have period of 11 years, 22 years and so on. Hence, in the above equation, m will be 1, 1/2 and so on.

We can obtain the non-storm variations in the temperature structure between two intervals at any given point of time and space in the lower thermosphere by combining equations (2.1) to (2.4). We design such a quiet time model in the following section.

2.3 Thermospheric Quiet Time Variation Model

The temperature measurements made along the orbit of TIMED satellite over a quiet and storm interval includes the storm response and the variations in the thermosphere arising from quiet time perturbations, that were described in the previous section. We write this as

$$T_s(\Theta, z) - T_q(\Theta, z) = \delta T(\Theta, z, \Omega_{\delta t}, \Omega_{\delta \lambda}, \Omega_{\delta \odot}) + T_{storm}, \quad (2.5)$$

where T_s and T_q are the SABER temperature measurements from orbits s and q that correspond to storm and quiet intervals respectively. $\Omega_{\delta t}$, $\Omega_{\delta \lambda}$ and $\Omega_{\delta \odot}$ are the difference in the local time, longitude and solar declination angle progression made by the satellite in the interval of separation between storm and quiet intervals. $\delta T(\Omega_{\delta t}, \Omega_{\delta \lambda}, \Omega_{\delta \odot})$ is the quiet time perturbation in the interval of separation and T_{storm} is the storm response.

In the remainder of this chapter, we present our methodology to derive a model, which represents the quiet time perturbations, $\delta T(\Omega_{\delta t}, \Omega_{\delta \lambda}, \Omega_{\delta \odot})$ using SABER temperature measurements. It involves fitting the model in a least-squares sense to the SABER temperature measurements and extracting the coefficients that minimize the error between the model and SABER temperature data. The formulation of such a model is dependent on the orbital characteristics of the satellite, data quality and the distribution of the quiet and storm intervals. The factors add bias and variance to the non-observable parameters (model coefficients) derived from the temperature measurements. We describe these factors that add bias and variance in the following section and the resulting model formulation.

2.3.1 Bias and Variance from Storm and Quiet Interval Distribution

Our data set is comprised of temperatures from 2002 to 2010 with quiet and active intervals as shown in fig. 2.2. In principle, any quiet interval in this data set could be used as a reference for calculating the thermosphere perturbations during any of the storm intervals. However, this is contingent upon the knowledge of the coefficients of a model that can describe all the expected non-storm perturbations that arise in the interval of separation. The process of determining these coefficients involves solving the inverse problem [94] of fitting the SABER temperature data to the model of non-storm thermosphere perturbations.

The estimation of coefficients of the quiet time variation model that are robust and can accurately reconstruct the data is contingent upon suitably addressing the sources of bias and variance that affect the estimated parameters. Data sampling and data distribution across the domain of the various predictors are sources of potential bias and variance which, if not accounted for, could cause erroneous estimation of the amplitude and phase of the quiet time variations.

One such source of erroneous estimation of the coefficients of the quiet time variation model is the error arising from omitted-variable-bias. Omitted-variable bias results when we ignore predictors in inverse problems which have a non-zero covariance with respect to other predictors of the model [95]. The storm response T_{storm} is a function of storm strength and storm duration, which in-turn are compounded by the phase of the solar cycle, season, and

local time. However the nature of the relationship of the storm strength and duration with respect to the solar cycle, season and local time is not known. In such a case considering active intervals for isolating the quiet time perturbations and not accounting for local time, seasons and solar cycle variations that are factored in the storm response, T_{storm} , would result in the coefficients of the quiet time perturbations to suffer from omitted-variable bias. Hence, we determine the coefficients of quiet time perturbations using only the quiet time intervals from our data set.

As seen in fig. 2.2, there is a preponderance of quiet intervals in the solar minimum phase of a solar cycle. The model coefficients that are determined from such a data set will be biased towards the solar minimum. Such a bias referred to as selection bias [96], would reduce their reliability in predicting the expected quiet time variation for the solar maximum phase. In order to prevent errors due to selection bias that would arise from our solar-minimum-dominant data set, we devise a piecewise technique of determining the quiet time variation. This piecewise technique involves using the closest quiet interval to the storm being investigated and not a random quiet interval as reference. The TIMED satellite performs a yaw maneuver once approximately every 60 days. There are 6 yaw maneuvers that occur annually and hence there are six yaw cycles. Yaw cycles in year 2009 are used to illustrate the yaw cycle interval in fig. 2.3. It was found that in our data set, there was at least one quiet interval available in every yaw cycle or the period of separation between two successive yaw maneuvers. The breakup of quiet intervals in each 60 day yaw cycle interval is illustrated in fig. 2.4. Note that the yaw cycle 6 extends on to the first few days of the next year, 2010 in the case of fig. 2.4.

Therefore, we have used the quiet interval closest to the storm interval with both intervals present in the same yaw cycle. This means that we only need to account for quiet time perturbations that arise in a yaw cycle which is about 60 days.

The quiet time perturbations that can occur in such an interval of separation with maximum length of 60 days will be due to tides, seasons and solar wind variation. Solar cycle effects are harmonics of a year and hence can be ignored. We define these parameters

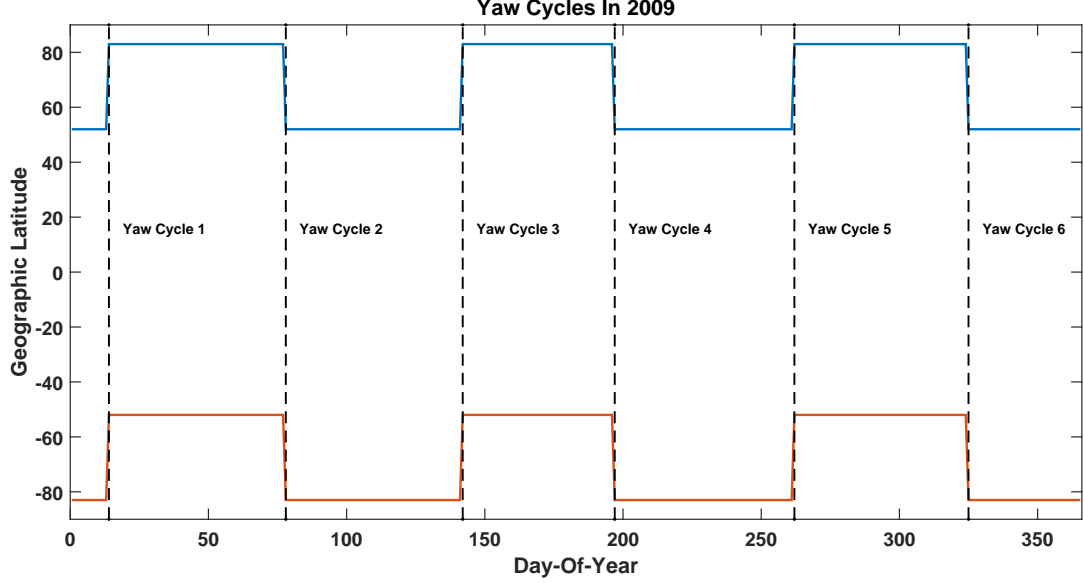


Fig. 2.3: Yaw cycle intervals.

as an additive model of the form

$$\delta T(\Theta, z, \Omega_{\delta t}, \Omega_{\delta \lambda}, \Omega_{\delta \odot}) = T_y(\Theta, z, \delta d) + T_{tw}(\Theta, z, \delta \lambda, \delta t) + T_g(\Theta, z, \delta \lambda). \quad (2.6)$$

Substituting equations (2.1) to (2.3) in (2.6), gives

$$\begin{aligned} \delta T(\Theta, z, \Omega_{\delta t}, \Omega_{\delta \lambda}, \Omega_{\delta \odot}) = & T_{0_g} + \sum_w j_w \cos(w\Omega_{\delta \lambda} - \zeta_w) + T_{0_{tw}} + \sum_p \sum_q b_{pq} \\ & \cos(p\Omega_{\delta t} + q\Omega_{\delta \lambda} - \beta_{pq}) + T_{0_y} + \sum_n s_n \cos(n\Omega_{\delta \odot} - \eta_n). \end{aligned} \quad (2.7)$$

A multiplicative model is chosen when the trend and the longer period components modulate the shorter period components. If we were to represent the thermosphere in its entirety, such a multiplicative model would be suitable to showcase the influence of solar cycle modulation on seasonal cycles and the seasonal modulation of the local time cycles. However, in our case we are looking at 60 day piecewise variations in the thermosphere. This corresponds to a single cycle of solar local time variation sampled by the SABER instrument and hence an additive model is suitable. Also, the solar wind variations are

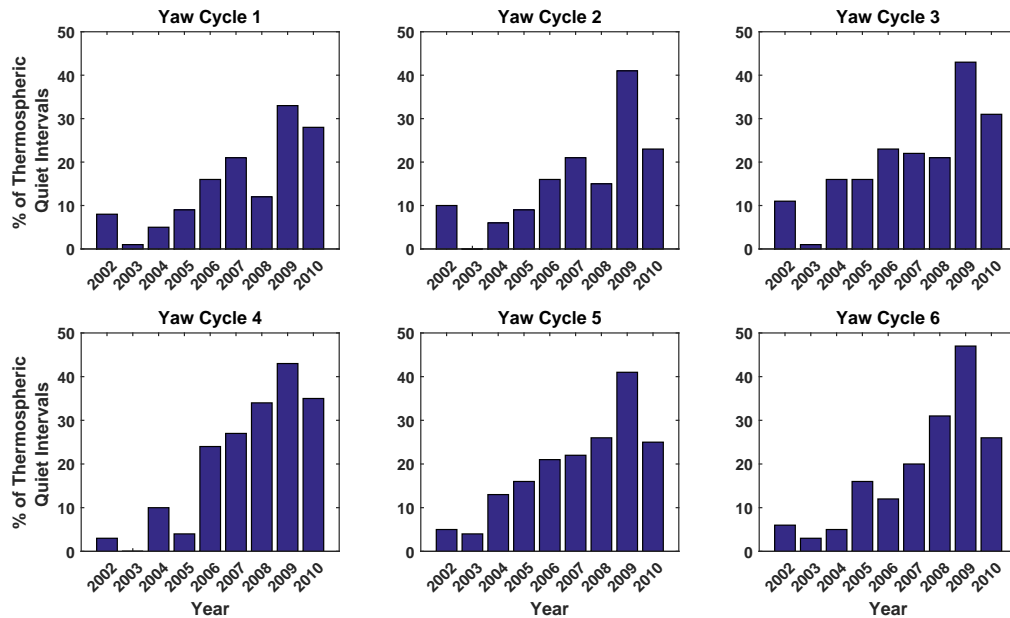


Fig. 2.4: Thermosphere quiet intervals divided as per yaw cycle intervals.

independent of seasonal variations and local time harmonics.

At this point it is important to note that the model of the thermosphere we derive here represents the relative change in temperature of the thermosphere over 60 days of quietitude. This relative change would be the same for any phase of the solar cycle given the same 60 days of the year and the same local times were considered. Although the absolute temperatures for such a 60 day interval would vary yearly due to the modulation effects of solar cycle, the solar cycle modulation over a 60 day interval would be the same and hence the relative change would be a function of season and local time coverage.

This piecewise continuous model which is evaluated separately for each yaw cycle, although free from errors of selection bias, would still not be free from problems of the skewed distribution of the quiet intervals across a solar cycle. The problem arises due to the limited number of quiet intervals in certain yaw cycles of the solar maximum. The inverse problem of determining the coefficients from such yaw cycles would result in an underdetermined system of equations. Using a severely underdetermined setup for solving the inverse problem presents us with the potential risk of our model coefficients to “match

the quiet intervals”, but not “fit them”. Absence of sufficient data points would also mean that partitioning the data set into test and training subsets and cross-validating the training set with the test set to gauge the ability to reconstruct the data, is not a feasible option to assuage any concerns regarding the quality of estimation.

To overcome this, we leverage the fact that the orbital parameters of the TIMED satellite were designed to be optimal for long-term synoptic measurements [60]. To illustrate this, the phase shift of the beta angle from 2002 to 2010 is plotted in fig. 2.5. Beta angle

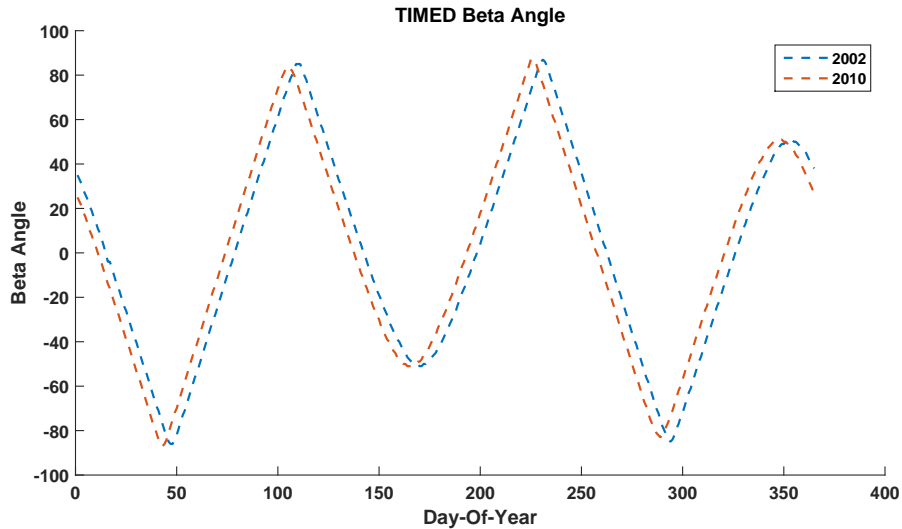


Fig. 2.5: Beta angle progression of TIMED satellite from 2002-2010.

is the angle between the sun-earth line and the complement to the normal of the satellite orbital plane. Tracing β is analogous to tracing of $\Omega_\lambda + \Omega_t$ in fig. 2.1. As seen in in fig. 2.5, the orbital shift for the period between 2002 and 2010 is minimal and was found to be at-most 5 days. The local time precession of the TIMED satellite is 12° a day and hence a shift of 5 days corresponds to a shift of less than an hour of local time. The thermosphere perturbations of periods less than an hour are not significant. The variations resulting from seasons which are functions of the day of year are also negligible when it comes to a span of less than 5 days.

Therefore we approximate the revisit of the satellite to a certain spatial grid to occur

on the same local time for a certain calendar day of any year in the period of 2002-2010. Hence the coefficients of the piecewise model calculated for a certain yaw cycle can be used to represent the relative variations for any year in the 2002-2010 interval, provided that the yaw cycle count is the same .i.e. yaw cycle is representing the same period of the year.

We illustrate the above discussed framework that our piecewise model for quiet time variation is based on, in fig.2.6. The temperature profiles in fig. 2.6 are merely used to explain the piecewise model setup and are not meant to be reflective of the actual SABER temperature measurement profiles. The fig. 2.6 illustrates a schematic of SABER measurements made along a single yaw cycle interval for years M and N . The total number of orbits made during the yaw cycle interval under consideration is X . ${}^K T_i$ represents the SABER temperature measurement for the i^{th} orbit and K^{th} year, for a latitude Θ and altitude z . Due to the TIMED annual revisit scheme, each orbit i for each year K , (K is between 2002 to 2010) can be approximated to sample at the same t , λ for a given Θ and z . Therefore we have

$${}^M T_i(\Theta, z) - {}^M T_j(\Theta, z) = {}^N T_i(\Theta, z) - {}^N T_j(\Theta, z) \quad (2.8)$$

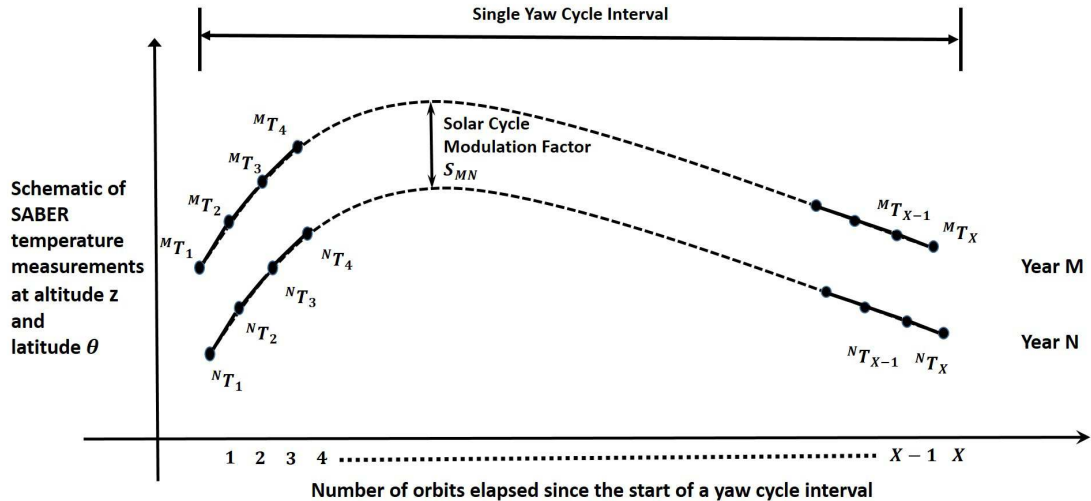


Fig. 2.6: A schematic to illustrate the principles of our piecewise continuous quiet time variation model.

As seen in fig. 2.2, the year 2009, which corresponds to the unusual solar minimum, had very little geomagnetic activity [97]. Hence it had the maximum thermosphere quiet intervals in each of the yaw cycles. Therefore, we deduce the amplitudes and phases from quiet interval SABER data of year 2009 for each of 6 yaw cycles. Using equation (2.8), we write the storm response defined by equation (2.5) as

$${}^K T_s(\Theta, z) - {}^K T_q(\Theta, z) = {}^{2009} \delta T(\Theta, z, \Omega_{\delta t}, \Omega_{\delta \lambda}, \Omega_{\delta \odot}) + {}^K T_{storm}. \quad (2.9)$$

Another principle of the piecewise model, an off-shoot of our assumption of solar cycle effects being negligible for inter-yaw cycle interval orbits, is

$${}^M T_i(\Theta, z) = {}^N T_i(\Theta, z) + S_{MN}(\Theta, z). \quad (2.10)$$

In equation (2.10), M and N are between 2002 and 2010 and i can be anything between 1 and X , where X is the total number of orbits in the yaw cycle. S_{MN} is the constant representing the solar cycle modulation difference between year M and N belonging to the same yaw cycle interval for latitude Θ and altitude z . The implications of the principle defined in equation (2.10) proves to be useful for storm response analysis and will be discussed in Chapter 3. In deriving the piecewise model the solar rotation effects are considered as negligible during quiet times and also the episodic presence of terrestrial weather system effects in the lower thermosphere are not considered.

2.3.2 Bias and Variance from Orbital Characteristics of the TIMED Satellite

Asynchronous satellites like TIMED do not return to the same geodetic location until the next day. Hence any changes with time scales less than a day with respect to a particular geodetic location cannot be discerned. Therefore measurements made by TIMED can only be used to trace the progression of the storm response of the thermospheric mean state over a certain latitude, orbit by orbit.

We integrate the temperature measurements over an interval of 2π with respect to

longitude ($\delta\lambda$) to obtain the thermospheric zonal mean temperatures. On integrating over an interval of 2π , the longitudes will be orthogonal and hence the solar wind variation and non-migrating tides and waves, will disappear. This is desirable from the inverse problem point of view, since fitting the data with a model comprised of fewer coefficients would result in robust fits. The interval of longitude progression by 2π corresponds to 24 hours of SABER measurements. On progressing the orbits used for integration, one orbit at a time, we will be able to capture the zonal mean progression of the thermospheric mean state on an orbit-by-orbit time scales.

Integrating the equation (2.7) with respect to $\delta\lambda$ over an interval of 2π gives us the zonal mean,

$$\delta T(\Theta, z, \Omega_{\delta t}, \Omega_{\delta \odot}) = T_{0_{tw}} + \sum_p b_p \cos(p\Omega_{\delta t} - \beta_p) + T_{0_y} + \sum_n s_n \cos(n\Omega_{\delta \odot} - \eta_n). \quad (2.11)$$

The frequency p of the solar day oscillations include tidal harmonics and the planetary waves. Therefore the domain of p is $1, 2, 3, \frac{1}{5}, \frac{1}{8}, \frac{1}{11}, \frac{1}{24}$. The seasonal variations are dominated by semi-annual or second harmonics of the year, although up to third or fourth harmonic are frequently used to represent the seasonal harmonics. Given that the maximum length of the time series we are investigating is close to 60 days or 24 hours in-terms of universal time, we make use of the small-angle approximation on the slowly progressing seasonal and planetary wave cosine functions. Splitting the solar day oscillations into tides and waves, we apply the small angle approximation for the slow progressing planetary waves and the seasonal variations. On expanding the seasonal and wave cosine functions and using the small angle approximation of $\sin(x) \approx x$ and $\cos(x) \approx 1 - \frac{x^2}{2}$, we get:

$$\begin{aligned} \delta T(\Theta, z, \Omega_{\delta t}, \Omega_{\delta \odot}) = & T_{0_{tw}} + \sum_k b_k \cos(k\Omega_{\delta t} - \beta_k) + \sum_l (b'_l(1 - \frac{l^2\Omega_{\delta t}^2}{2}) + b''_l(1 + l\Omega_{\delta t})) \\ & T_{0_y} + \sum_n (s'_n(1 - \frac{n^2\Omega_{\delta \odot}^2}{2}) + s''_n(1 + n\Omega_{\delta \odot})). \end{aligned} \quad (2.12)$$

In equation (2.12), $s'_n = s_n \cos(\eta_n)$, $s''_n = s_n \sin(\eta_n)$. The tidal harmonics are denoted

by the subscript k and the planetary wave harmonics by the subscript l . Also, $b'_l = b_l \cos(\beta_l)$, $b''_l = b_l \sin(\beta_l)$.

On expanding the summation over the small angle approximations and grouping all similar terms together, we get

$$\delta T(\Theta, z, \Omega_{\delta t}, \Omega_{\delta \odot}) = T_0 + \sum_k b_k \cos(k\Omega_{\delta t} - \beta_k) + S''\Omega_{\delta \odot} + S'\Omega_{\delta \odot}^2 + B''\Omega_{\delta t} + B'\Omega_{\delta t}^2. \quad (2.13)$$

In the above equation, $T_0 = T_{0_{tw}} + T_{0_y} + \sum_n s'_n - s''_n + \sum_l b'_l - b''_l$, $S'' = \sum_n s''_n n$, $B' = \sum_l b'_l l^2/2$, $B'' = \sum_l b''_l l$ and $B' = \sum_l b'_l l^2/2$. The value of k varies from 1 to 3 for the tidal harmonics.

The model described here has been designed for the purpose of representing expected quiet time thermospheric behavior in a collective fashion and not for ascertaining the behavior of the individual quiet time perturbations. Hence the representation in the form of equation (2.13) is suitable as the number of coefficients that need to be fit are reduced. In the following section, this model as described by equation (2.13), will be fit for data corresponding to each of the six yaw cycles to determine the coefficients of quiet time perturbations.

2.4 SABER Data Presentation

The SABER temperature measurements of the thermosphere between 100 - 120 km for all latitudes made along 14.8 orbits corresponding to a single solar day under thermospheric quiet time is illustrated in fig. 2.7. The data plotted represents 91st day of year 2010 and hence belong to the second yaw cycle interval with the southern hemisphere being the dominant hemisphere.

In our analysis, the data from each such orbit is separated into latitude and altitude bins. We bin the temperature data into latitude bins of 20° and altitude bins of 5 km. The temperature data for various latitude bins corresponding to an altitude of 110 km altitude are illustrated in fig. 2.8 corresponding to the year 2009.

In the fig. 2.8, the black vertical lines indicate yaw maneuvers, the red and blue

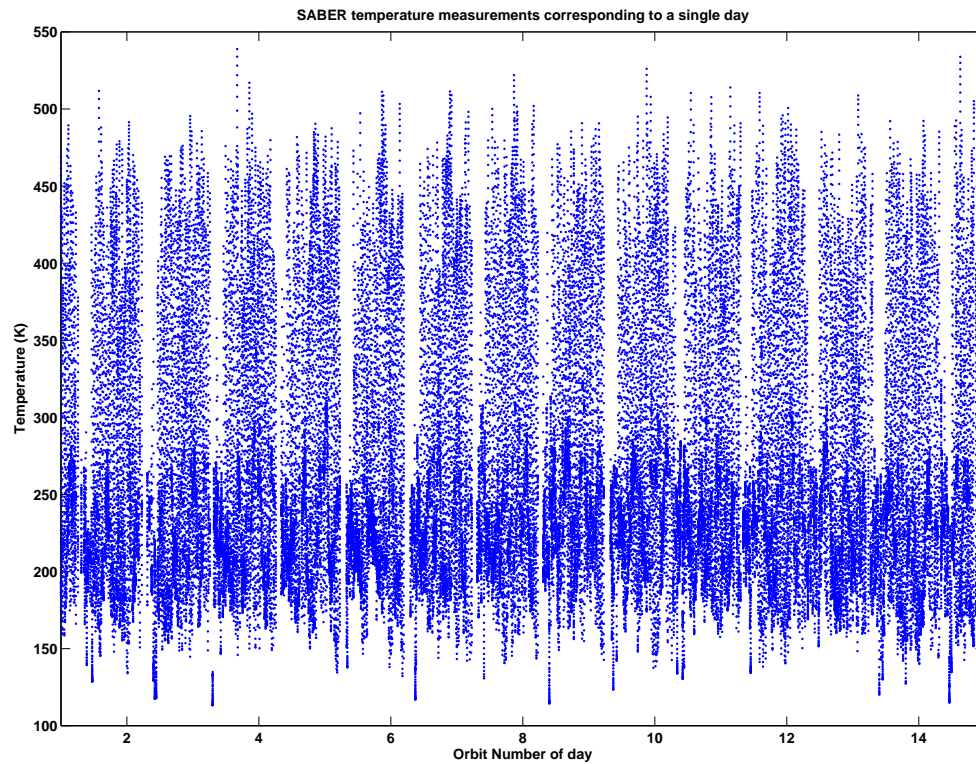


Fig. 2.7: SABER temperature from both upleg and downleg measurements of latitudes -83° to 53° and altitudes 100 to 120 km corresponding to all the orbits made on a single day. These orbits are from day of year 91 for the year 2010.

data points correspond to active and quiet thermosphere intervals respectively. The orbit of year refers to TIMED orbit progression since Jan 1st 0:00 UT. The temperature data point corresponding to each orbit is comprised of both upleg and downleg measurements that occur at different local times, which leads the intra-orbit variability in the fig. 2.8. The progression of solar local time and solar day lend the variability for the inter-orbit measurements seen in fig. 2.8. Since 2009 corresponds to the unusual solar minimum, the active days were fewer in number and the intensity of the storms were lower.

2.4.1 Zonal Mean of Temperature Variation

As seen in fig. 2.8, SABER data has several periods of missing data points within a

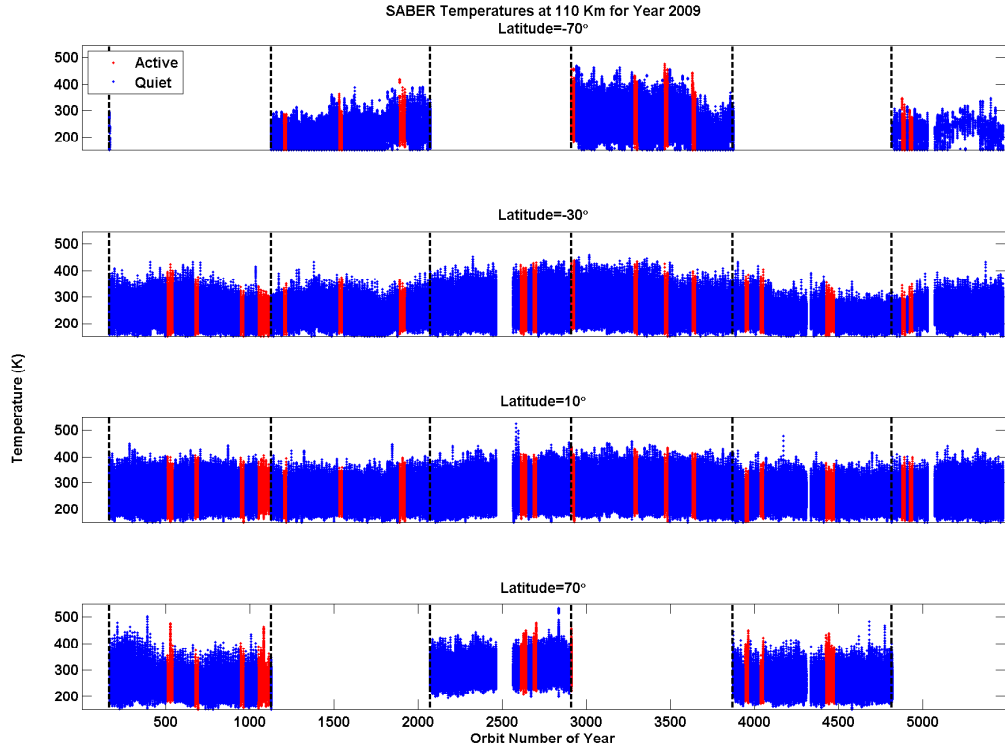


Fig. 2.8: SABER thermosphere temperature measurements at 110 km for the year 2009. The red points correspond to active times and those in blue correspond to quiet intervals of thermosphere.

yaw cycle. This is due to changes in instrument configuration, absence of data collection around local noon, issues with data processing algorithms etc. In such cases, irregular longitudinal sampling and subsequent incomplete zonal coverage occur. This in-turn would result in incomplete removal of non-migrating tidal components from the zonal mean, when $\delta\lambda$ integrated over 2π radians, due to $\cos(p\Omega_{\delta t} + q\Omega_{\delta\lambda} - \beta_{pq})$ being non-orthogonal. In addition, the spatial variations from quiet time solar wind will also not be completely removed due to non-orthogonality of $\cos(w\Omega_{\delta\lambda} - \zeta_w)$.

To account for this, and to prevent aliasing of non-migrating tides and solar wind perturbations into the calculated zonal mean temperatures, we use a procedure similar to the one outlined in Zhu et al. [98] for calculating the zonal mean temperatures. In a 24

hour window of time that is used for calculating the zonal mean temperature, we drop one or more longitude bins whose cosine function values, when summed along with the cosine function value of the longitude bins with missing data, will sum to zero. The zonal mean temperature variation of quiet intervals across various latitudes calculated as defined above is plotted in fig. 2.9.

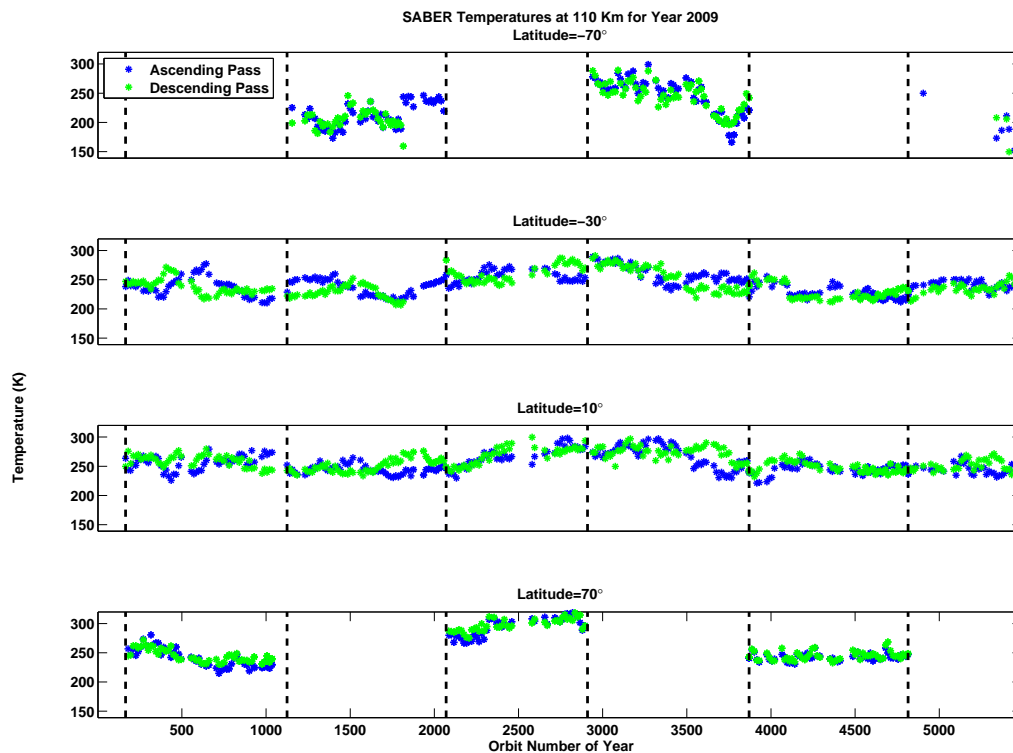


Fig. 2.9: Zonal mean of thermosphere temperature variation at 110 km for quiet intervals in the year 2009.

The temperature measurements are made along both upleg and downleg of the of the TIMED orbit which we refer to as the ascending pass and descending pass measurements respectively i.e. ascending pass is the upward leg measurement from -53° to 83° or from -83° to 53° (based on the yaw cycle).

2.5 Extraction of Coefficients of Quiet Time Thermospheric Perturbations

The zonal mean of temperature variation calculated as described above is used to obtain $\delta T(\Theta, z, \Omega_{\delta t}, \Omega_{\delta \odot})$ to fit the quiet time variation model using equation (2.13). $\delta T(\Theta, z, \Omega_{\delta t}, \Omega_{\delta \odot})$ is the temperature variation between two quiet intervals of a yaw cycle. The extraction of coefficients describing this quiet time variation model involves fitting equation (2.13) to the set of all quiet interval temperature variations $\delta T(\Theta, z, \Omega_{\delta t}, \Omega_{\delta \odot})$ of a yaw cycle.

We define $\delta T(\Theta, z, \Omega_{\delta t}, \Omega_{\delta \odot})$ as the difference in temperature of all quiet intervals with respect to a reference $T_{ref}(\Theta, z)$. We take this reference as the temperature measurement made at the ascending pass of the first quiet interval of the yaw cycle interval. Hence $\delta T(\Theta, z, \Omega_{\delta t}, \Omega_{\delta \odot})$ is calculated by subtracting the zonal mean temperature of the 1st day of yaw cycle under consideration, from all the quiet day zonal mean temperatures of a latitude and altitude bin. Similarly, day of year variation and local time variation at the ascending pass of the 1st interval of yaw cycle interval has been subtracted from all day of year measurements and local times respectively, of the quiet times being fit.

In addition, we normalize the temperature variation $\delta T(\Theta, z, \Omega_{\delta t}, \Omega_{\delta \odot})$ with respect to $T_{ref}(\Theta, z)$ to express the variation as relative change in temperature with respect to our reference $T_{ref}(\Theta, z)$ in terms of percentage. The normalization to obtain the percent variation is to facilitate storm response calculations since the norm is to represent storm response as percent increase in energy. By normalizing temperature variations, our coefficients of the model that will be extracted from the fit will also be in percentage and expressed relative to $T_{ref}(\Theta, z)$. Although the normalized percent form of the model prevents direct interpretation of the model coefficients, the objective here has been to find a model that will represent the collective quiet time variations in the thermosphere and not discern the behavior of individual components of such a model. Therefore, for every x^{th} zonal mean temperatures of a yaw cycle, we have $\delta \tilde{T}_x(\Theta, z) = \frac{T_x(\Theta, z) - T_{ref}(\Theta, z)}{T_{ref}(\Theta, z)} * 100$, where $T_{ref}(\Theta, z)$ is the zonal mean calculated using the ascending pass measurements of the first quiet day of the yaw cycle. Similarly the local time and day of year corresponding to every x^{th} zonal mean will be $t_x - t(o)$ and $d_x - d(0)$. We define the quiet time variation model normalized

with respect to $T_{ref}(\Theta, z)$ and expressed in percentages as

$$\delta\tilde{T}(\Theta, z, \Omega_{\delta t}, \Omega_{\delta\odot}) = \tilde{T}_0 + \sum_k \tilde{b}_k \cos(k\Omega_{\delta t} - \beta_k) + \tilde{S}''\Omega_{\delta\odot} + \tilde{B}''\Omega_{\delta t} + \tilde{S}'\Omega_{\delta\odot}^2 + \tilde{B}'\Omega_{\delta t}^2, \quad (2.14)$$

where, $\tilde{T}_0 = \frac{T_0}{T_{ref}(\Theta, z)}$, $\tilde{b}_k = \frac{b_k}{T_{ref}(\Theta, z)}$, $\tilde{S}'' = \frac{S''}{T_{ref}(\Theta, z)}$, $\tilde{B} = \frac{B''}{T_{ref}(\Theta, z)}$, $\tilde{S}' = \frac{S'}{T_{ref}(\Theta, z)}$, and $\tilde{B}' = \frac{B'}{T_{ref}(\Theta, z)}$.

The distribution of zonal mean quiet time temperature variations $\delta\tilde{T}$ across local time δt and day of year δd is illustrated using two different yaw cycles for various latitudes in fig. 2.10.

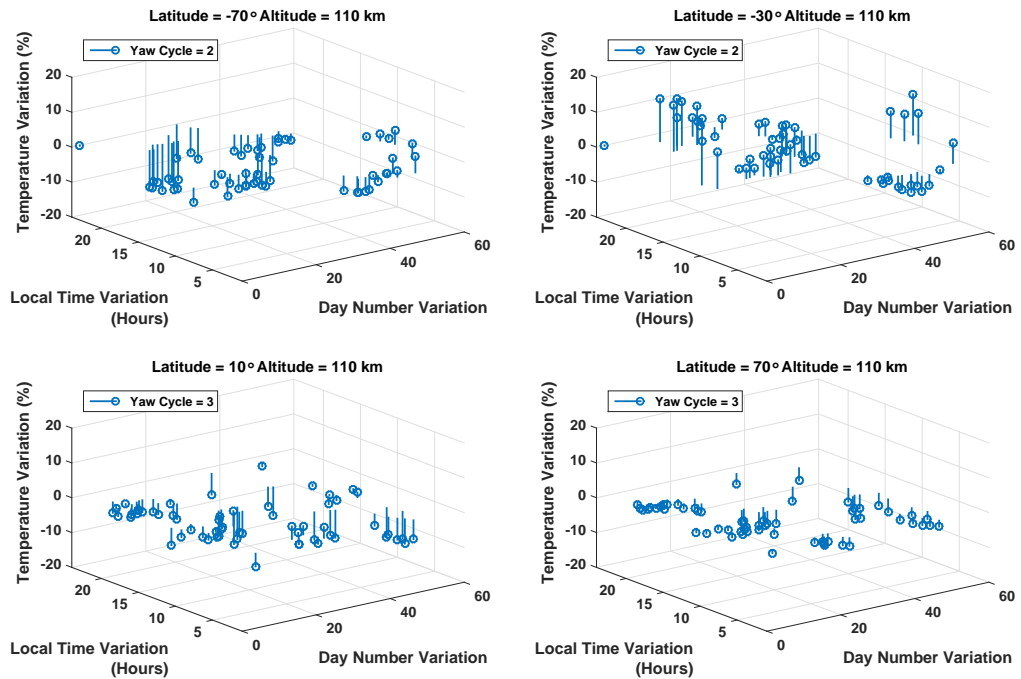


Fig. 2.10: Zonal mean temperature variations at 110 km for quiet intervals in the year 2009 for selected latitudes corresponding to yaw cycles 2 and 3.

The coefficients of the quiet time variation model have been calculated using partial least square regression since the coefficients were found to be highly correlated and to ensure robust solution to the inverse problem, partial least square regression was used. Partial least

square regression [99] constructs new predictors known as PLS components which are linear combination of the predictors of the inverse problem. The PLS components constructed with the minimum number of predictors and which have maximum co-variance with the response variables are used to solve the inverse problem. Hence this approach is free from perils of over-fitting due to multi-collinearity of predictors and over-fitting from limited data points.

We use the *PLSREGRESS* function in MATLAB for calculating the coefficients of quiet time variation. The *PLSREGRESS* function is initially applied to find the minimum number of PLS components needed to express the response variance and using that many components, the *PLSREGRESS* function was again applied to find the unknown coefficients in equation (2.14).

2.6 Discussion and Fitting Results

The process of fitting the quiet time variation model involves determining the coefficients \tilde{T}_0 , \tilde{b}_k , β_k , \tilde{S}'' and \tilde{B}'' that minimize

$$\sum_N [\delta\tilde{T}_N - (\tilde{T}_0 + \sum_k \tilde{b}_k \cos(k\Omega\delta t_N - \beta_k) + \tilde{S}''\Omega_{\delta\odot N} + \tilde{B}''\Omega_{\delta t_N})]^2 \quad (2.15)$$

The data shown in fig. 2.9 were fit using partial least square regression using equation 2.15 and the comparison of the fit and data is illustrated in fig. 2.11. The coefficient of the model calculated are illustrated in fig. 2.12 and fig. 2.13. The coefficients are in percent and the coefficient numbers 1 to 6 refer to \tilde{T}_0 , \tilde{b}_1 , \tilde{b}_2 , \tilde{b}_3 , \tilde{S}'' and \tilde{B}'' respectively. The phase coefficients 1 to 3 refer to β_1 to β_3 respectively. Note that the mean term \tilde{T}_0 and the linear terms \tilde{S}'' and \tilde{B}'' have both negative and positive values. The negative values arise due to the seasonal and local time trend decreasing with respect to the reference point $T_{ref}(\Theta, z)$. It is important to note that the amplitudes are normalized with respect to $T_{ref}(\Theta, z)$ and that they are the expected variation from $T_{ref}(\Theta, z)$ along the SABER orbit for a given yaw cycle. These values do not represent the absolute trend or variations in the thermosphere and are mere snapshots of thermospheric variation expected along the SABER orbit. The

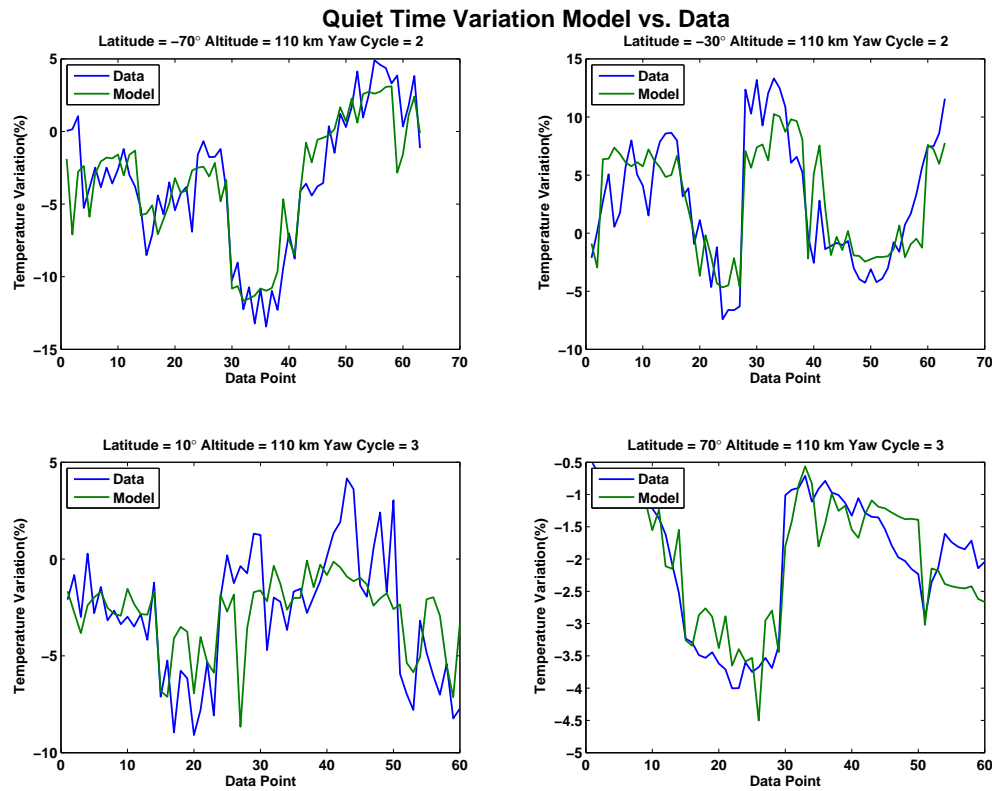


Fig. 2.11: Illustration of fitting results for SABER zonal mean temperature vs. quiet time variation model for thermospheric quiet intervals, for selected latitudes of yaw cycle 2 and 3 for altitude bin of 110 km.

amplitudes and phases of the thermospheric quiet time variation model for all the latitude and altitude bins corresponding to each of the six yaw cycles of SABER are presented in Appendix A.

The objective of this endeavor has been to capture and model the quiet time variations in a collective manner so that they can be isolated from storm time temperature measurements. It is hence pertinent that we investigate this total quiet time variability. The total variability from quiet time will include the variability due to local time and day of year progression along the SABER orbit and the random variability. We refer to the local time and seasonal variability as the systematic variability. The random variability includes the random error left behind from the fitting process. The residual left behind after fitting the

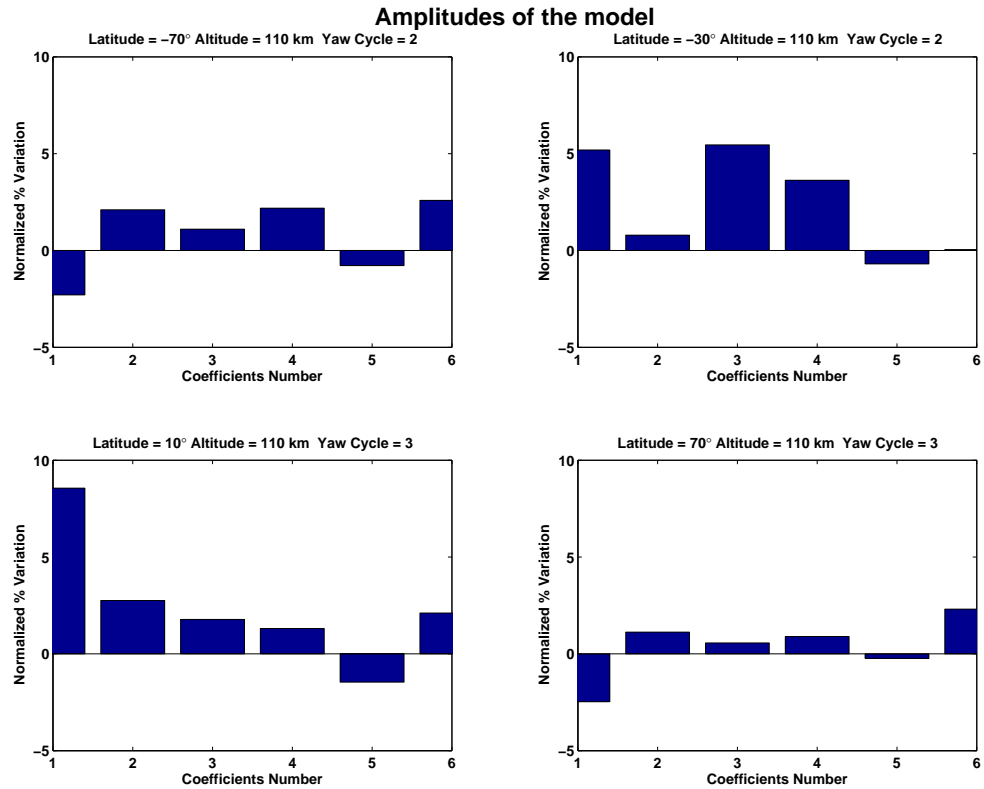


Fig. 2.12: Amplitude coefficients of the quiet time variation model calculated from the fit for selected latitudes of 110 km altitudes. The yaw cycle corresponding to the latitudes are noted at the top of the plot.

quiet time model could be due to irregular factors like gravity wave breaking from terrestrial weather events.

We investigate the maximum systematic variability seen between any two quiet intervals. In our setup, maximum variability refers to any two quiet intervals belonging to the same yaw cycle interval. The maximum value was chosen because the maximum systematic quiet time variation between any two days will serve as an indicator of the amount of variation we can see between storm and quiet interval due to non-storm sources. Hence it is analogous to the maximum amount of quiet time variation that would be aliased into the storm response deductions if a setup like the quiet time variation model was not used.

The maximum systematic variability calculated using our quiet time variation model

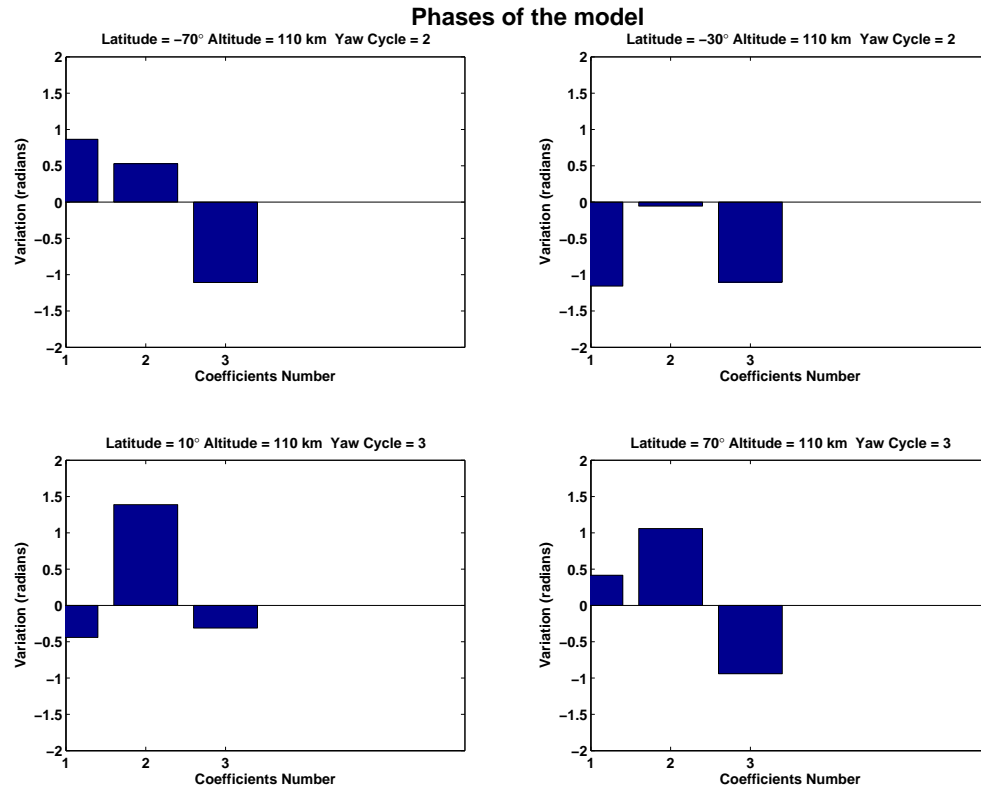


Fig. 2.13: Phase coefficients of the quiet time variation model calculated from the fit for selected latitudes of 110 km altitudes. The yaw cycle corresponding to the latitudes are noted at the top of the plot.

for all the altitudes and yaw cycles for the latitudes that were previously used for illustrating the quiet time model fitting results, is shown in fig. 2.14. It is taken as the maximum of the difference between the quiet time variation model calculated values between any two days of the yaw cycle interval.

The maximum amount of random variation is shown in fig. 2.15. It illustrates the maximum amount of variation that was observed between any two quiet intervals due to random effects.

These variabilities for all latitude-altitude bins are presented in Appendix A. We need to note that the systematic variability that is presented here is the expected quiet time variability observed along the TIMED orbit measurements. The systematic variability might

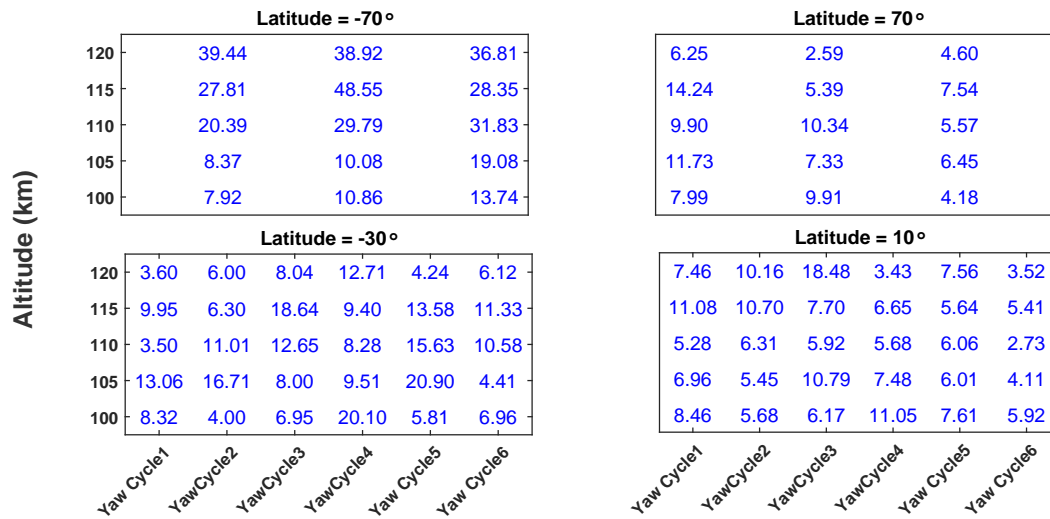


Fig. 2.14: Illustration of maximum systematic variability derived using our quiet time variation model.

be more or less than what was presented here for a satellite orbit having a different local time precession. Unlike the systematic variability, the random variability is not dependent on the satellite orbit and gives the maximum residual obtained after fitting for all known sources of thermospheric non-storm variability. It is also worth noting that the model for thermospheric quiet time variability that is described here, is by no means a complete quiet time variability model. It only accounts for those sources of variation which have been deemed significant in the lower thermosphere by the current state of knowledge.

2.7 Summary

The asymptotic nature of satellite measurements and separation of quiet interval from the storm interval can lead to aliasing of non-storm variations when storm interval measurements are compared to quiet intervals to deduce the storm response. In this chapter, we derived a procedure to extract such non-storm variations and isolate storm response.

The challenges of using a satellite platform and the multi-modal nature of thermospheric quiet time variations were discussed and a procedure which leverages the almost-constant beta angle progression of the TIMED satellite was derived. A key feature of this

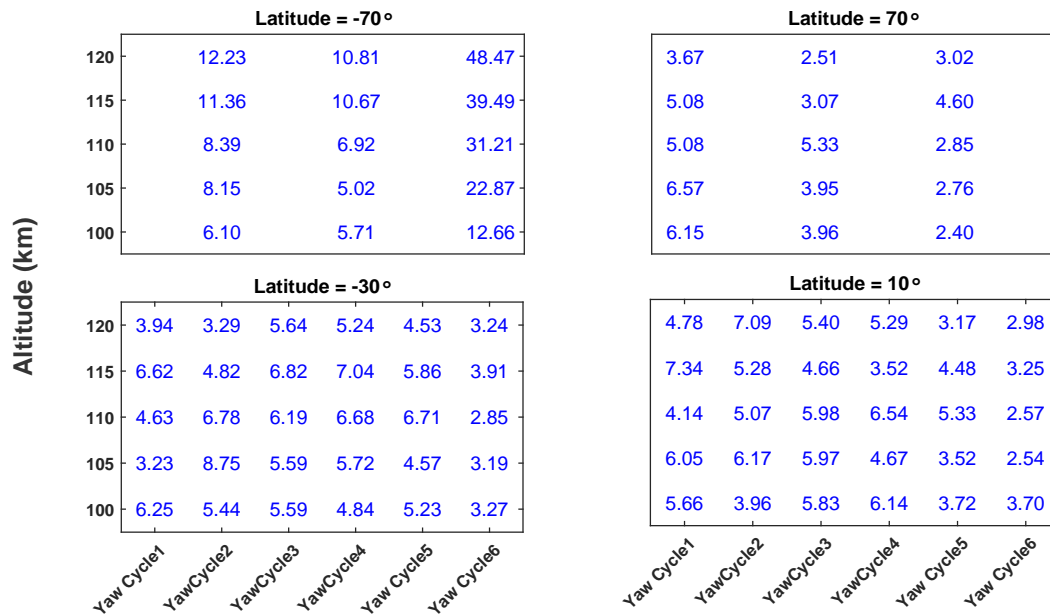


Fig. 2.15: Illustration of maximum random variability derived using our quiet time variation model.

procedure was the use of data from the unusually low solar minimum of solar cycle 23. The data with large number of geomagnetically quiet days was the key in overcoming the bias and variance associated with the satellite orbital characteristics.

The procedure we call piecewise quiet time variation model, expresses the relative variation one would see between any two given days in the same yaw maneuver interval. By using this, we can successfully remove the non-storm variations in the storm-quiet data and isolate storm response.

We also explored the expected quiet time variability that stems from tidal and seasonal harmonics for all latitude and altitude bins and they were found to be around 20% - 40% for high latitudes and around 5% - 20% for the lower latitudes.

CHAPTER 3

SABER TEMPERATURE RESPONSE TO GEOMAGNETIC STORMS

Geomagnetic storms are intense disturbances in the Earth's magnetosphere [100]. They occur when plasma and magnetic fields ejected from the solar corona are geo-effective and have high speeds, abrupt density changes and prolonged southward IMF [9, 13]. During such conditions, the northward oriented geomagnetic field of the Earth connects with the southward IMF on the dayside magnetopause, injecting particles and energy into the Earth's magnetosphere and building energy stored in the magnetosphere. The magnetic and particle energy in turn energize the Earth's atmosphere via the magnetosphere-ionosphere currents. This magnetic and particle energy are converted to internal and kinetic energy of the atmosphere, which then undergoes a global redistribution, causing a change in the dynamics and energetics of the Earth's thermosphere and the ionosphere.

Understanding this global response requires us to investigate the spatial-temporal changes brought about by this energy redistribution. Observations of the thermosphere state variables are used to discern this energy redistribution by comparing the changes in their behavior during a storm, relative to their steady state values. The storm response so deduced is then used to infer the neutral atmospheric energetics that occur due to the storm.

In this chapter, we investigate the redistribution of the storm energy in the lower thermosphere using SABER measurements. We compare the SABER temperatures during a storm interval with that of SABER measurements made during thermospheric quiet intervals. Using satellite measurements to isolate storm response requires us to remove the non-storm artifacts from the temperature measurements. We use the quiet time variation model derived in Chapter 2 to do this. The morphology of the derived storm response is then investigated across various latitudes to understand the process of global energy redistribution.

3.1 Thermospheric Storm Intervals

The occurrence and progression of geomagnetic storms are most commonly traced using geomagnetic indices, and in this study, we use two such indices, Kp index and Dst index. The progression of Kp index above 4 indicates the occurrence of a geomagnetic storm [100]. The recovery of the magnetosphere to quietude is marked by Kp index values of 2 and lower [81].

However, the thermosphere and magnetosphere do not have a one-to-one correspondence when it comes to charging and discharging of solar wind energy [77]. Hence we take the end of a storm period in the atmosphere as 24 hours after the magnetosphere has achieved quietude. The time period of 24 hours is chosen because the lower thermosphere is currently believed to achieve complete recovery 15-21 hours following the cessation of storm energy [79].

Being mindful of this thermospheric recovery time, for the case of successive storm intervals we require at least 24 hours of separation between the cessation of one and the onset of the other, for them to be classified as two separate storm intervals. In cases with successive storm intervals with less than a day of separation between the two, we combine them and consider them as a single prolonged storm interval.

3.2 Isolation of Storm Response from SABER Measurements

We deduce the storm response by discerning the differences seen in the storm interval measurements with respect to that of quiet interval. To ensure we remove non-storm variations from the difference between the two, we formulated the piecewise quiet time variation model in Chapter 2. Using this model, we isolate the storm response using

$$\left(\frac{S_{K2009} + {}^K T_s(\Theta, z) - {}^{2009} T_{ref}(\Theta, z)}{{}^{2009} T_{ref}(\Theta, z)} \right) * 100 - \left(\frac{S_{K2009} + {}^K T_q(\Theta, z) - {}^{2009} T_{ref}(\Theta, z)}{{}^{2009} T_{ref}(\Theta, z)} \right) * 100 = {}^{2009} \delta \tilde{T}_s(\Theta, z, \Omega_{\delta t}, \Omega_{\delta \odot}) - {}^{2009} \delta \tilde{T}_q(\Theta, z, \Omega_{\delta t}, \Omega_{\delta \odot}) + \tilde{T}_{storm}(\Theta, z). \quad (3.1)$$

In eq. 3.1, ${}^K T_s$ and ${}^K T_q$ are the zonal mean temperatures of the storm and quiet interval respectively for latitude Θ and altitude z . ${}^{2009} \delta \tilde{T}_s(\Theta, z, \Omega_{\delta t}, \Omega_{\delta \odot})$ and ${}^{2009} \delta \tilde{T}_q(\Theta, z, \Omega_{\delta t}, \Omega_{\delta \odot})$

are the quiet time variations deduced using the piecewise quiet time variation model described by eq. 2.14, for the storm and quiet intervals respectively, with reference to the reference interval, ‘ref’. As discussed in Chapter 2, the interval ‘ref’ corresponds to the ascending node of the first quiet day since the onset of the yaw cycle being considered in 2009. ${}^K T_{ref}$ is the temperature of this interval in year K. The interval in year K corresponding to ${}^{2009} T_{ref}$ i.e. ${}^K T_{ref}$ might not necessarily be geomagnetically quiet in every storm interval. Therefore, we use ${}^{2009} T_{ref}$ in eq. 3.1. As shown in eq. 2.10, we represent the solar modulation effects by using S_{K2009} to account for inter-solar cycle year temperatures. This enables us to use the ${}^{2009} T_{ref}$ in our setup for any ${}^K T_s$, as long as we are within the confines of the piecewise quiet time model set up illustrated in fig. 2.6. \tilde{T}_{storm} is the storm response in percentage. Simplifying eq. 3.1

$$\begin{aligned} & \left(\frac{{}^K T_s(\Theta, z) - {}^{2009} T_{ref}(\Theta, z)}{{}^{2009} T_{ref}(\Theta, z)} * 100 \right) - \left(\frac{{}^K T_q(\Theta, z) - {}^{2009} T_{ref}(\Theta, z)}{{}^{2009} T_{ref}(\Theta, z)} * 100 \right) \\ & = {}^{2009} \delta \tilde{T}_s(\Theta, z, \Omega_{\delta t}, \Omega_{\delta \odot}) - {}^{2009} \delta \tilde{T}_q(\Theta, z, \Omega_{\delta t}, \Omega_{\delta \odot}) + \tilde{T}_{storm}(\Theta, z). \end{aligned} \quad (3.2)$$

The storm response $\tilde{T}_{storm}(\Theta, z)$, as per the quiet time model set-up will give the storm response in Kelvin, on multiplying ${}^{2009} T_{ref}(\Theta, z)$. The ${}^{2009} T_{ref}(\Theta, z)$ values for all yaw cycles and latitude-altitude bins is illustrated in Appendix B.

3.3 Storm Interval Under Investigation

In the remainder of this section, we use observations corresponding to a single storm interval to illustrate storm response features and the lower thermospheric behavior under the influence of geomagnetic storm energy. This is intended to serve as a primer for the statistical study to be discussed in Chapter 4. We discuss the morphology of the observed storm response and derive storm response variables which represent the salient features of this morphology and are key to conduct the statistical study. To facilitate this, we chose a storm interval that exhibited variety in its storm response morphology across the various latitude-altitude bins and hence serves as an excellent source for discussing the variation in storm morphology features and the corresponding storm response variables. We illustrate

the chosen storm interval using Kp index as well as Dst index in fig. 3.1. The onset of this storm interval was on 6th May 2003 at 12:00 UT. The interval in fig. 3.1 corresponds to 72

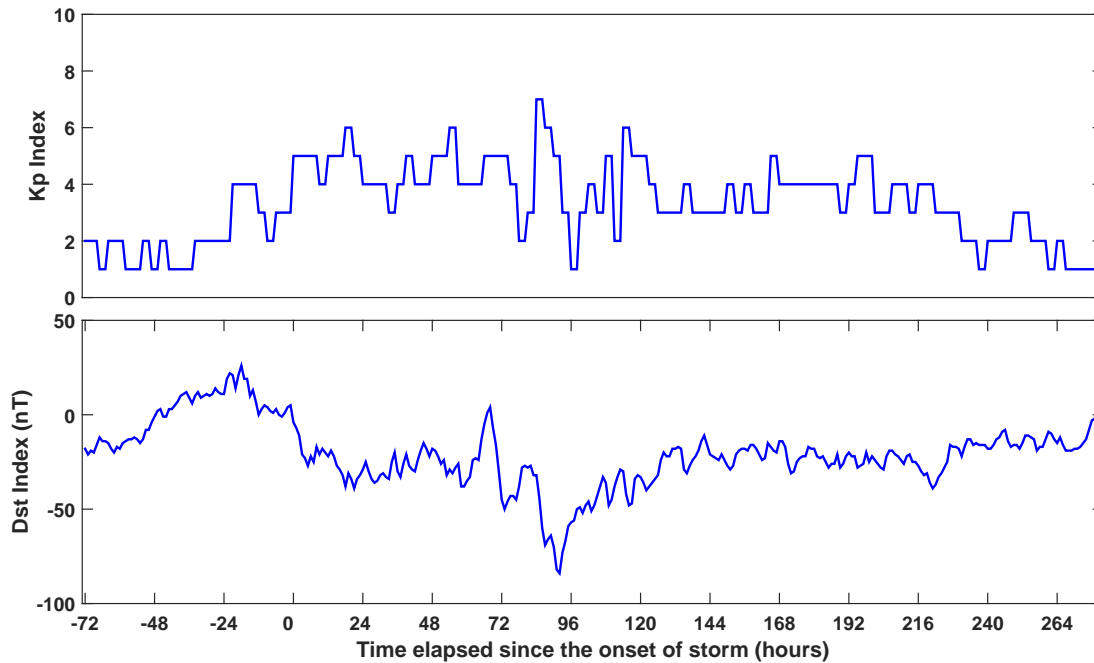


Fig. 3.1: Dst index and Kp index for the 6-May-2003 geomagnetic storm interval.

hours of data prior to the storm occurrence and extends 24 hours after the thermospheric storm interval has ended. The extended period of Dst and Kp index prior to the storm is also illustrated in fig. 3.1, to show the closest quiet interval to the storm. At this point we would like to recall that the thermospheric quiet intervals are defined as intervals with Kp index < 3 and, which are preceded by a 24 hour interval of Kp index < 3 . Hence the period from 24 - 48 hours prior to the storm onset corresponds to the thermospheric quiet interval in fig. 3.1.

In addition, we also illustrate the Dst index for the storm interval in fig. 3.1. The Dst index having a cadence of every hour, serves as an excellent supplement in our storm analysis, particularly for tracing the progression of storms on an hourly basis. Although unlike Kp index, demarcation of Dst index into quiet, active and storm is not clearly defined

but, Dst index < -30 nT is usually classified as a storm [101]. The start of Dst taking on a positive slope after going southwards of -30 nT indicates the cessation of solar wind energy input into the magnetosphere. The discharge of magnetospheric storm energy is marked by Dst index's continued positive slope for an extended period of time.

Isolating Storm Response

The application of the quiet time variation model requires us to conduct our analysis using zonal mean temperatures. These zonal mean temperatures are calculated by integrating the temperatures over a period of 24 hours, as elaborated in Chapter 2. By progressing the integration interval one orbit at a time, we can construct a time series of the zonal mean temperatures.

The time series for the storm interval has been constructed such that the zonal mean temperature for the storm onset is formed by integrating data from the orbit corresponding to the storm onset, along with the preceding 13/14 orbits that would constitute an interval of 24 hours (SABER completes 14.8 orbits in a day). This interval is progressed forward one orbit at a time. The last point would include the orbit corresponding to the conclusion of the storm interval followed by its succeeding orbits that would constitute a 24 hour interval.

The time series so constructed is essentially the application of a moving average filter with the filter delay being compensated by the inclusion of data before and after the storm interval. This ensures the phase of the variation being captured by the filtered data matches with that of the raw data. Since the SABER orbit is 1.6 hours long, the construction of the time series of the zonal mean temperatures consist of data from the storm interval would essentially consist of data from 22.5 hours before the storm onset and 22.5 hours after the atmospheric quietude is reached.

In addition to the zonal mean, the quiet time variation model requires the use of quiet intervals that are from the same yaw cycle as that of the storm interval. The quiet interval closest to the storm represented in fig. 3.1, was found to be 4th May 2003 12:00 UT to 5th May 2003, 12:00 UT, and the zonal mean temperature of this 24 hour quiet interval was calculated at each latitude and altitude to serve as the steady state reference, to isolate the

storm time disturbances from SABER temperatures. The storm interval is part of the yaw cycle 2 of SABER and hence the data coverage consists of -70° to 50° latitudes. The storm response will continue to be expressed in latitude bins of 20° , altitude bins of 5 km and in geographic or geodetic coordinates.

We use the Dst index to track and measure the storm energy progression owing to its hourly availability. To ensure the phase of Dst index is in-sync with SABER storm response, we integrate Dst index over 24 hour intervals on a rolling basis. The zonal mean temperatures of the storm interval and of the quiet interval are illustrated for the -70° latitude bin and 110 km altitude bin, and the corresponding Dst index in fig. 3.2.

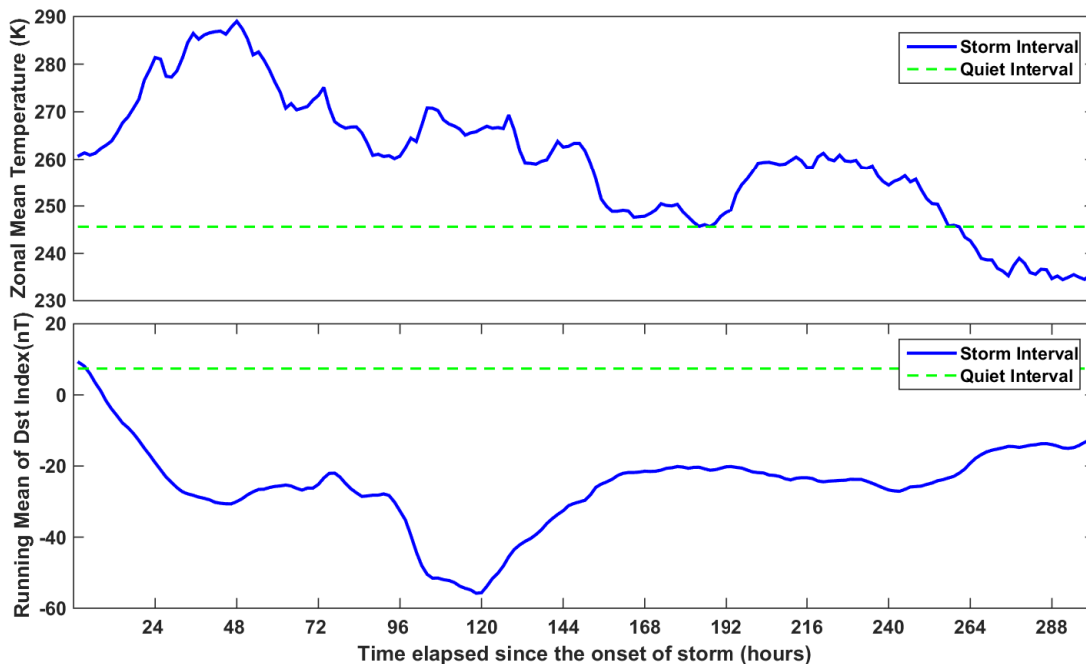


Fig. 3.2: Dst Index and zonal mean temperatures of the thermosphere at the 110 km altitude and -70° latitude bin for the 6-May-2003 storm interval.

The storm response is calculated using equation 3.2. The storm response before removing the quiet time variations, the quiet time variation aliased into the storm response as determined by the quiet time variation model, the isolated storm response after removing the quiet time variations, along with the storm interval Dst variation with respect to

the quiet interval Dst index, are all plotted in fig. 3.3. The storm response before removing the quiet time variations refers to equation 3.2 where $^{2009}\delta\tilde{T}_s(\Theta, z, \Omega_{\delta t}, \Omega_{\delta\odot})$ and $^{2009}\delta\tilde{T}_q(\Theta, z, \Omega_{\delta t}, \Omega_{\delta\odot})$ are not removed using the quiet time variation model. The quiet time variation aliased into the storm response is $^{2009}\delta\tilde{T}_s(\Theta, z, \Omega_{\delta t}, \Omega_{\delta\odot})$ and $^{2009}\delta\tilde{T}_q(\Theta, z, \Omega_{\delta t}, \Omega_{\delta\odot})$, calculated using the quiet time variation model.

As noted earlier, the quiet interval considered for the storm under study, consists of the interval 24 to 48 hours prior to the onset of the storm interval. Hence the local time and day-of-year difference between the quiet and storm interval increases with the progression of storm. This explains the trait of increasing contribution of the quiet time variations with the storm progression seen in fig. 3.3. In the following section, we examine the morphology of the storm response for various latitude and altitude bins, to discern the storm induced energy redistribution in the thermosphere.

3.4 Morphology of Storm Response

To illustrate the storm induced temperatures changes occurring globally in the 100 - 120 km thermosphere, we continue to present the storm response for the 6-May-2003 storm interval. In figs. 3.4 - 3.6, we present the storm response for various altitude-latitude bins for the storm period under discussion, to illustrate the typical morphology of storm response observed in our study.

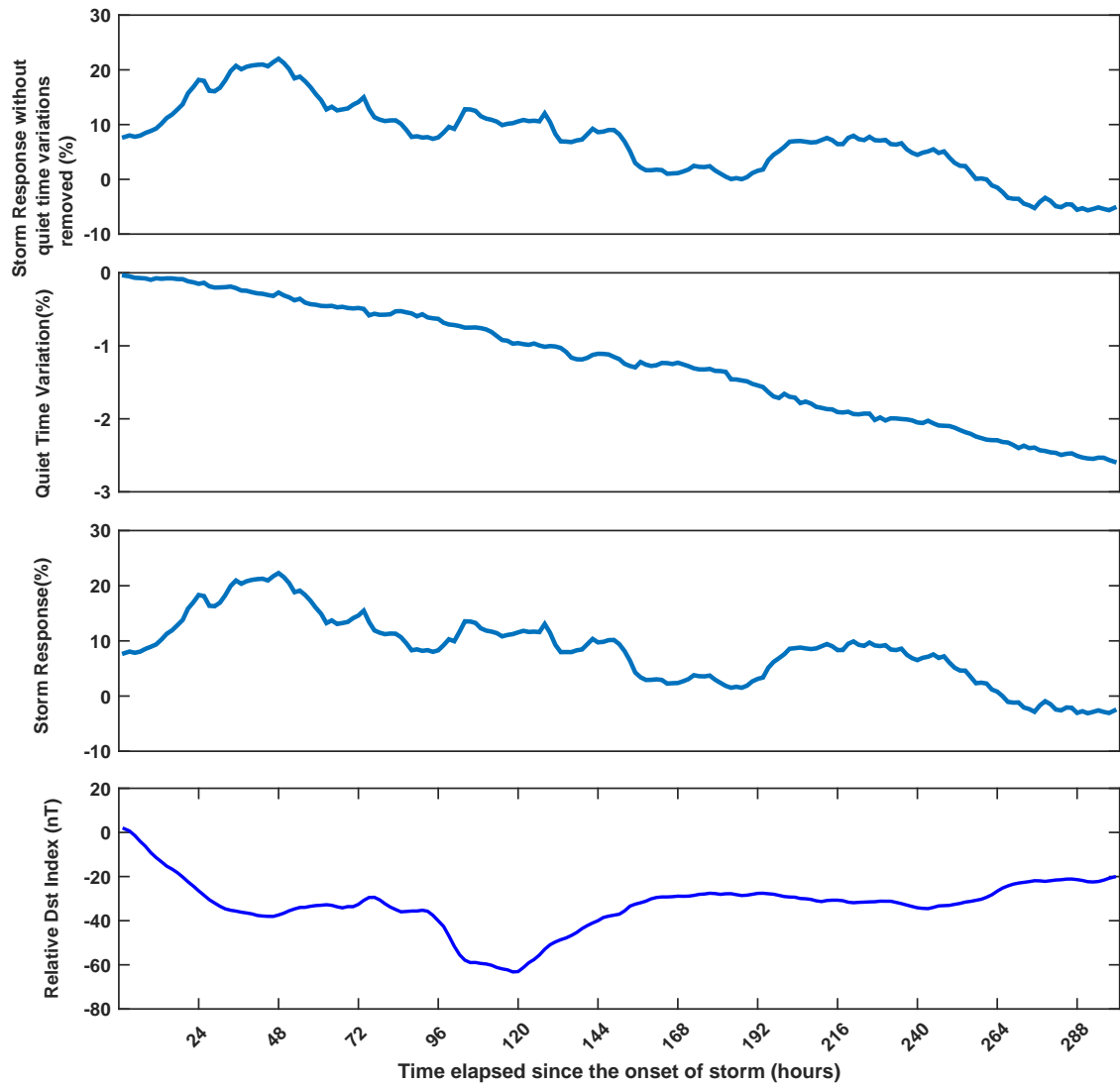


Fig. 3.3: Thermospheric storm response at 110 km altitude and -70° latitude for the 6-May-2003 storm interval.

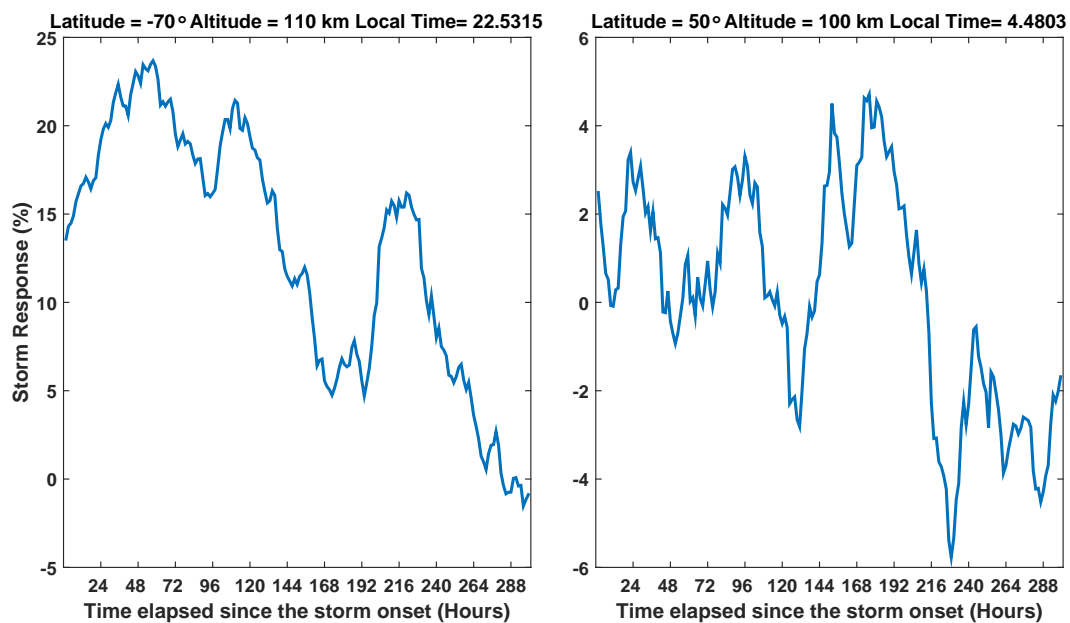


Fig. 3.4: Thermospheric response to May 6th 2003 storm observed at the latitude bins of -70° (left panel) and 50° (right panel). The altitudes, and the local time at which SABER samples the two latitude bins, is noted at the top of the plot.

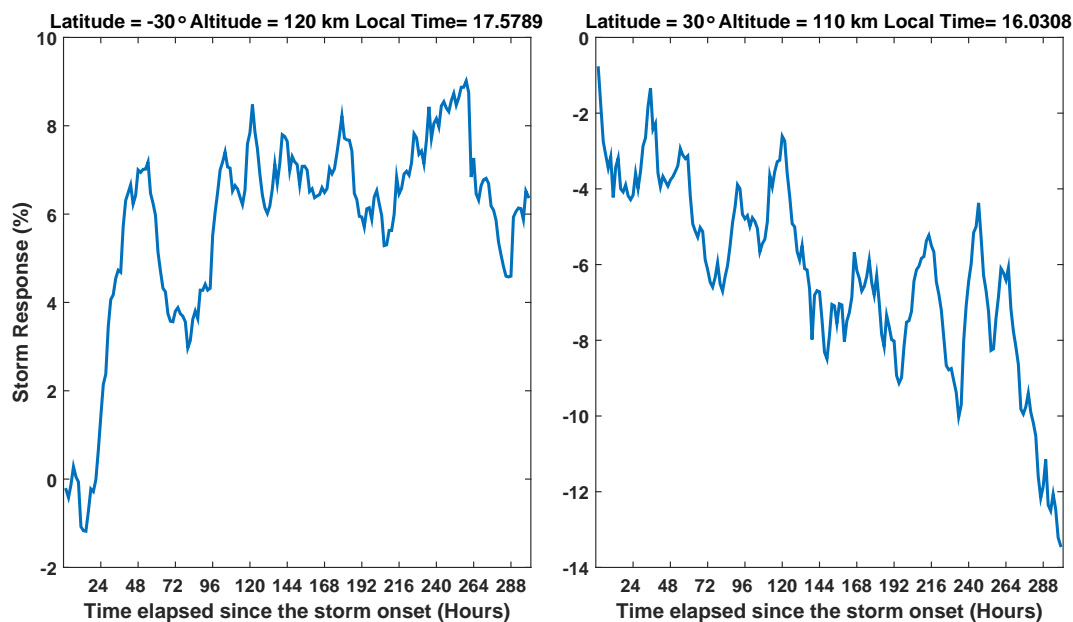


Fig. 3.5: Thermospheric response to May 6th 2003 storm observed at the latitude bins of -30° (left panel) and 30° (right panel). The altitudes, and the local time at which SABER samples the two latitude bins, is noted at the top of the plot.

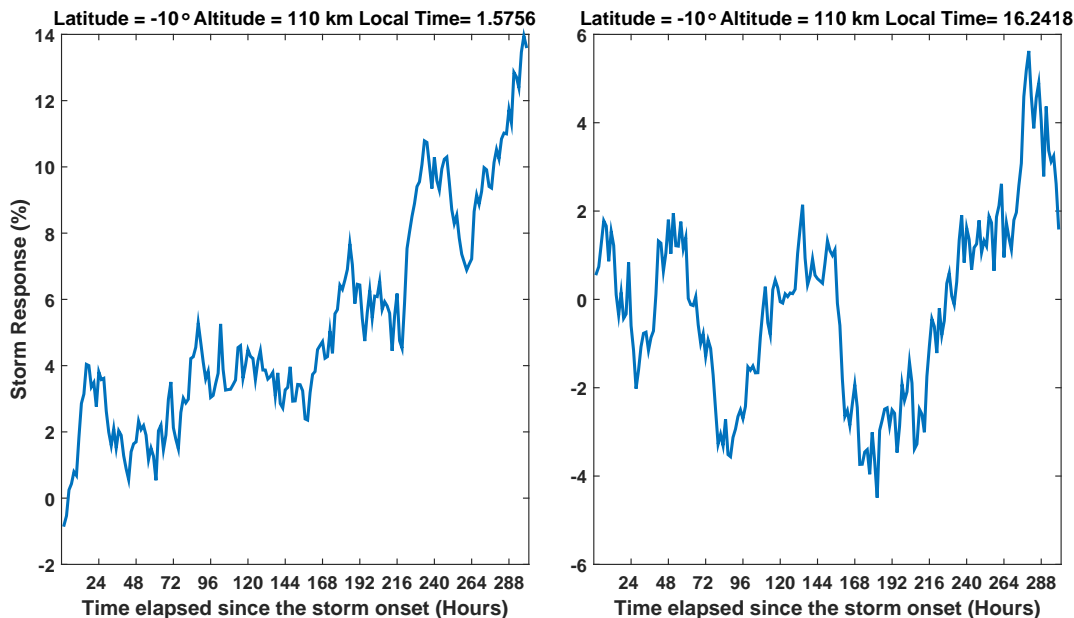


Fig. 3.6: Thermospheric response to May 6th 2003 storm observed at the latitude bins of -10° (left panel) and 10° (right panel). The altitudes, and the local time at which SABER samples the two latitude bins, is noted at the top of the plot.

One of the persistent feature that we can see from figs. 3.4 - 3.6, is the presence of wavelike structures on several scales. These waves with periods of a few hours to days have been observed in various thermospheric studies and are attributed to generation and progression of gravity waves globally [32,36]. We point the readers to the investigation by Brusnima et al. [36], and the references within, for understanding the characteristics and triggers of these waves across various latitudes under storm conditions.

The -70° latitude bin, illustrated in fig. 3.3 and also in fig. 3.4, corresponds to the region subjected to *in situ* heating from the convergence of the magnetosphere energy. This *in situ* heating drives the morphology of the temperature response to mimic the storm energy morphology, with the storm response exhibiting three distinct pulses in response to the three pulses that form the storm energy time series as seen in fig. 3.3.

Unlike the polar latitudes, the storm response morphology in the sub-polar latitude bins does not mimic the progression of storm energy and the morphology of the response

varies widely. This is because the latitude bins southward of -70° do not undergo any *in situ* heating and the temperature increase is attributed to the heat being transported from the polar disturbance regions in both the hemispheres by various transport processes like advection, conduction, adiabatic heating and diffusion.

The larger scale wave-like structures comprising alternate increasing and decreasing temperatures with periods of tens of hours are seen in the sub-polar latitudes. These could be attributed to the imprint of traveling atmospheric waves (TADs) triggered at high latitudes, or an indication of the upwelling and downwelling from a convective cell set-up as part of the storm energy circulation. These waves are also accompanied by an increasing background trend in some cases, as illustrated in the first plot of fig. 3.5. This increasing trend might be an indication of background heating through advection or that the waves deposit energy nonlinearly as they propagate. There is also the occurrence of a decreasing temperature trend, as illustrated in fig. 3.6, indicating energy divergence is also seen in some latitudes. This could be attributed to the lack of storm energy persistence in the given latitude-altitude bin and instead indicate transport of energy to a different latitude-altitude bin. The storm response can also be a steady increase in temperature without any large scale wave activity as seen in the first plot of fig. 3.9. This could be indicative of strong horizontal advection, set-up without any delays. However, it could also be an indication of an energy front rapidly moving equatorward indicating conduction, as speculated in a case study of upper thermospheric response to storms, where increasing horizontal winds without a corresponding composition variation were observed [39].

Although TADs can be identified by the presence of phase shifts in the large scale waves for successive latitudes, we would need wind and composition measurements to decipher each feature of the storm response morphology as a symptom of a certain transport process. Hence, the temperature measurements alone cannot successfully reveal the physical process responsible for transporting the storm energy.

However, by looking at the energy convergence and divergence, we can trace the temporal and spatial manner in which energy is redistributed following a storm. The storm

energy convergence, irrespective of the transport mechanisms will be seen as an increasing temperature trend. Discerning the times and magnitudes of the increasing trend will reveal the extent of variation that the storm causes in a given latitude-altitude bin. By tracing the subsequent temperature decrease following the peak positive temperature, we can learn how the thermosphere recovers following the storm. By applying this to each latitude and altitude bin, we can reveal the effects of a storm spatially and temporally.

Hence in this study, where only the thermosphere temperature data is used, the storm response will be analyzed in the context of spatial and temporal energy redistribution alone.

To trace the storm-induced spatial and temporal variations in the thermosphere, we define a set of storm response variables, which are essentially the times and magnitudes of energy (temperature) convergence (increase) and divergence (decrease), serving as indicators of energy redistribution. These storm response variables will be calculated for each latitude-altitude bin.

The main reason to conceptualize these variables is to facilitate the statistical study of storm response. The temperature patterns and trends cannot be manually investigated to reveal the energy redistribution when dealing with a decade worth of storms. These storm response variables will serve as features which can be used to automate the extraction of storm effects from the morphology of the temperature response to storms, and aid in revealing statistically useful insights.

The storm response variables that we will use to represent the storm energy redistribution are illustrated 3.7 in and are defined as follows:

- **Time Delay:** This variable represents the time scales of energy transport to regions of non *in situ* heating. It is defined as the time taken for the storm energy to reach the latitude-altitude bin following the onset of storm. It is measured as hours elapsed since the storm onset. The energy reaching a given latitude-altitude bin is discerned by the presence of an increasing trend in the storm response. The time in hours since the storm onset, measured with respect to the first point of the increasing trend is hence the time delay.

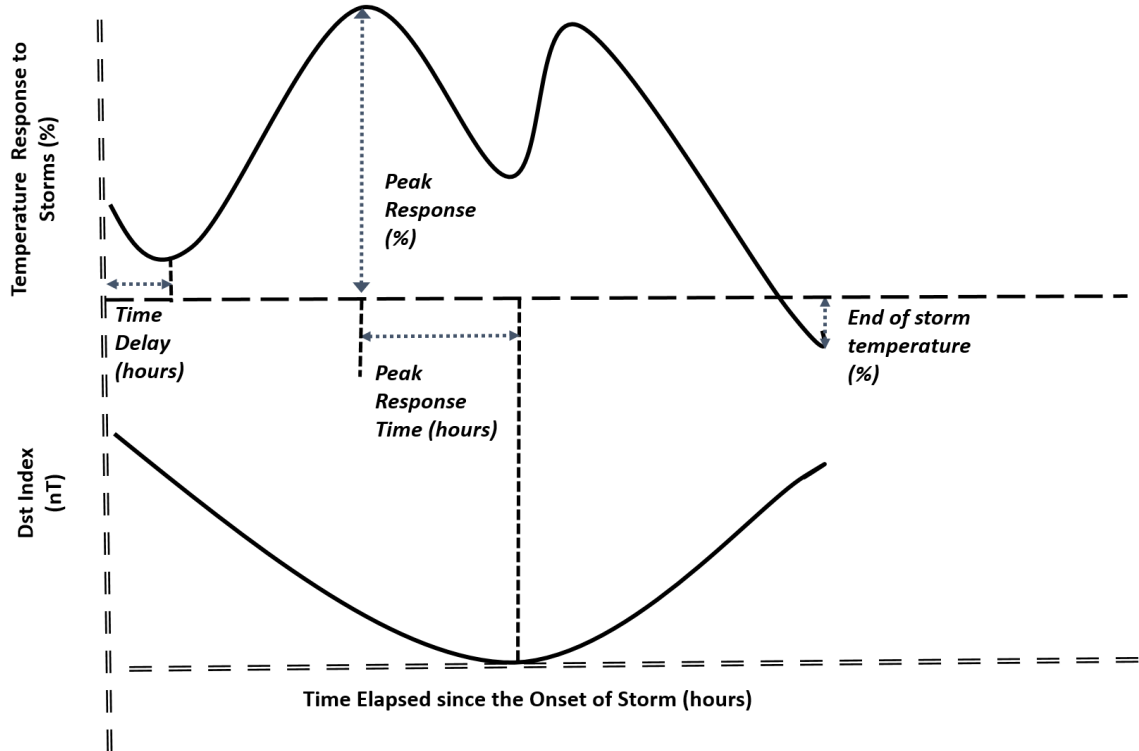


Fig. 3.7: Schematic to illustrate Storm Response Variables.

- **Peak Response:** It is defined as the maximum temperature increase seen during the storm interval. Since we are expressing storm response in percent, this will be in percentage. This variable measures the magnitude of storm energy disruption globally.
- **Peak Response Time:** It is defined as the time taken for the storm energy to reach its peak convergence in each latitude-altitude bin. It is measured as time elapsed since the time corresponding to the peak of storm energy. Since we are using Dst index for tracing the storm energy progression, the peak storm energy refers to the lowest Dst index value. This variable represents the gross morphology of energy convergence and divergence patterns of the storm energy in a given latitude-altitude bin.
- **End-of-Storm Response:** It is defined as the temperature at the completion of the storm interval. This will be expressed in percentage. The end of storm magnitude is

useful to ascertain if the period of 24 hours is indeed sufficient for the thermosphere to recover to its quiet time values after the storm energy ceases.

Note that the schematic 3.7 is an idealized version and does not necessarily reflect all the nuances of the storm response. It is merely drawn to illustrate the definition of different storm response variables. One particular feature that might not be easily discerned from the schematic would be the case of storms with increasing or decreasing trends, which are not succeeded by a subsequent decrease or increase respectively. For instance, the 110 km altitude and 10° latitude, illustrated in fig. 3.6, the temperature continues to increase throughout the storm interval and hence the end of storm response and peak response would coincide. Another instance would be the mid latitude response at 110 km 30° latitude, illustrated in fig. 3.5, which exhibits a decreasing trend. The response to storm is seen after a delay, as a mild temperature increase. This is followed by a decreasing trend, with the end of storm response having the highest variation from pre-storm values and hence being equal to the peak storm response value.

3.5 Magnitude and Time Response of the Thermosphere to Geomagnetic Storms

We apply a temporal smoothing filter to iron out small scale variations from the storm response and facilitate derivation of the storm response variables of interest. We use the *findpeaks* function in MATLAB to isolate and analyze peaks of interest from the storm response morphology. We have chosen the filter length to be 24 hours. Since we use Dst index to trace the input of storm energy, a smoothing filter of the same length as the temperature response is applied to Dst index to synchronize it with the storm response and facilitate their comparison. We illustrate the smoothed Dst index and storm responses for all the altitude-latitude bins discussed earlier as well as few other latitude-altitude bins to demonstrate the global storm response in the figs. 3.9 - 3.20 .

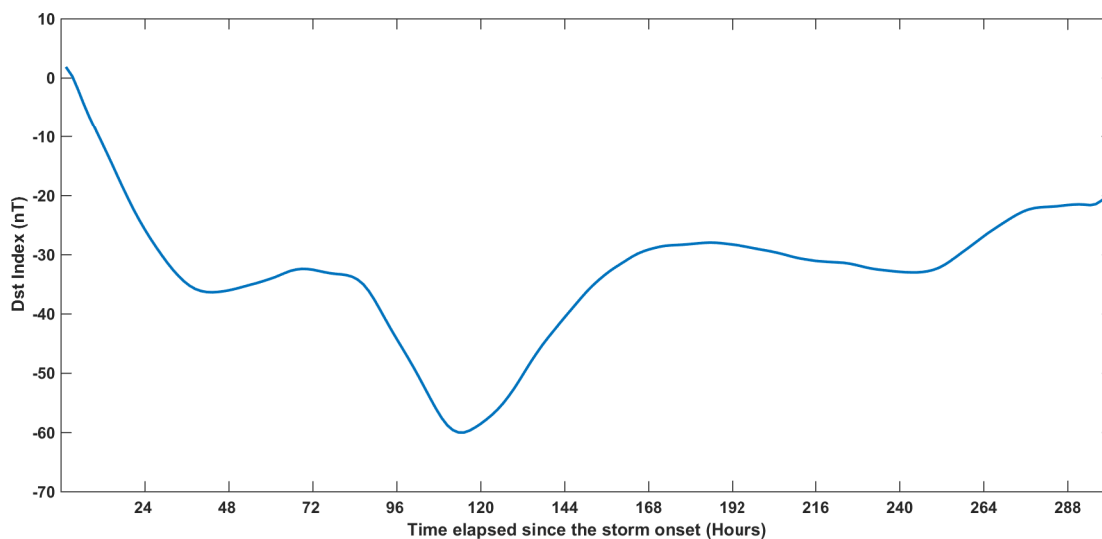


Fig. 3.8: Temporally smoothed relative Dst index for the May 6, 2003 storm interval, where the relative Dst index corresponds to the the storm time Dst expressed as relative variation with respect to the quiet interval Dst index.

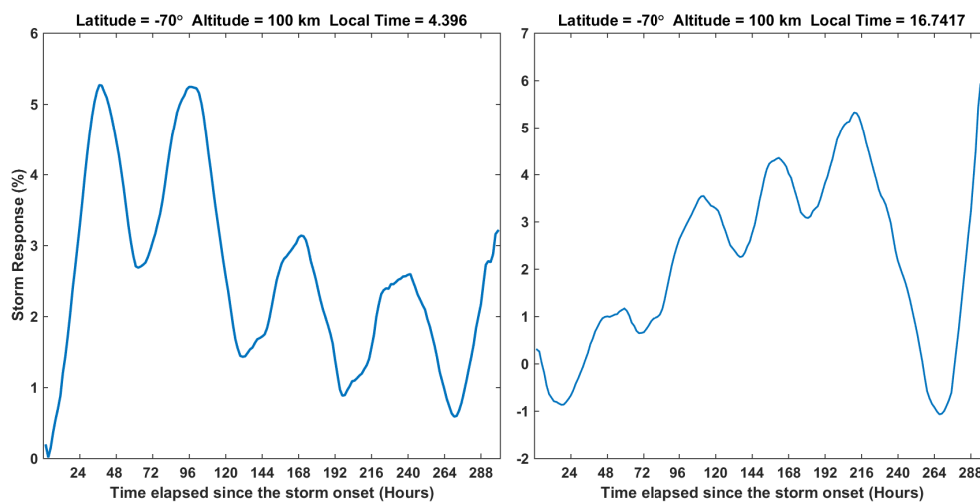


Fig. 3.9: Thermospheric storm response at 100 km altitude and 70° latitude for the 6-May-2003 storm interval. The left and right panels in the figure represent the ascending pass measurements and descending pass measurements respectively. The local time at which SABER samples the latitude bin for the two passes are illustrated at the top of the panels.

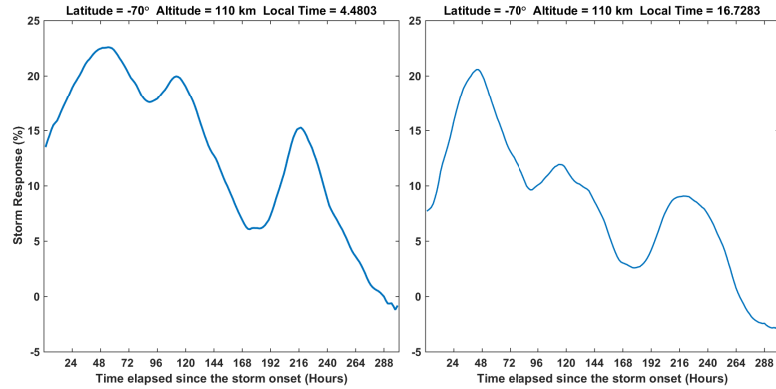


Fig. 3.10: Thermospheric storm response at 110 km altitude and 70° latitude for the 6-May-2003 storm interval. The left and right panels in the figure represent the ascending pass measurements and descending pass measurements respectively. The local time at which SABER samples the latitude bin for the two passes are illustrated at the top of the panels.

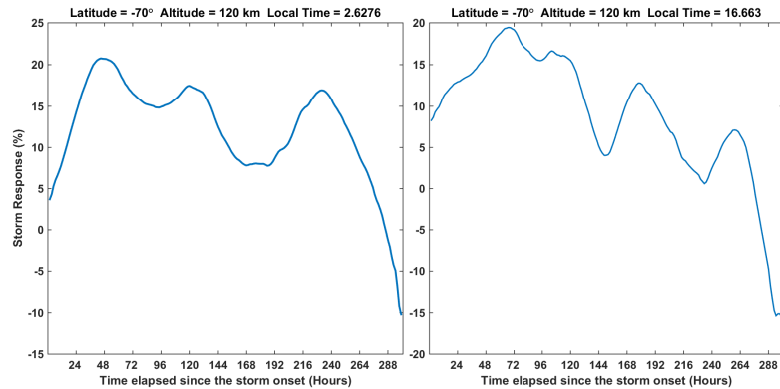


Fig. 3.11: Thermospheric storm response at 120 km altitude and 70° latitude for the 6-May-2003 storm interval. The left and right panels in the figure represent the ascending pass measurements and descending pass measurements respectively. The local time at which SABER samples the latitude bin for the two passes are illustrated at the top of the panels.

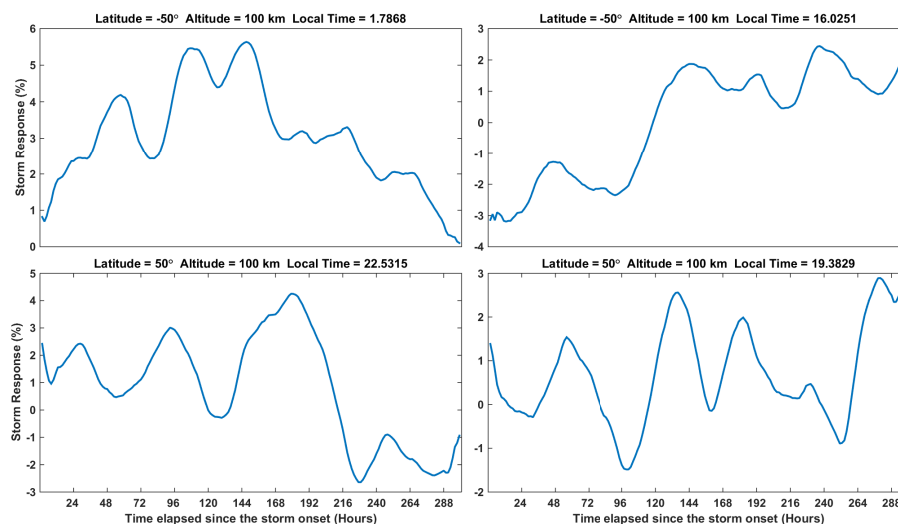


Fig. 3.12: Thermospheric storm response at 100 km altitude and 50° and -50° latitudes for the 6-May-2003 storm interval. The left and right panels in the figure represent the ascending pass measurements and descending pass measurements respectively. The local time at which SABER samples the latitude bin for the two passes are illustrated at the top of the panels.

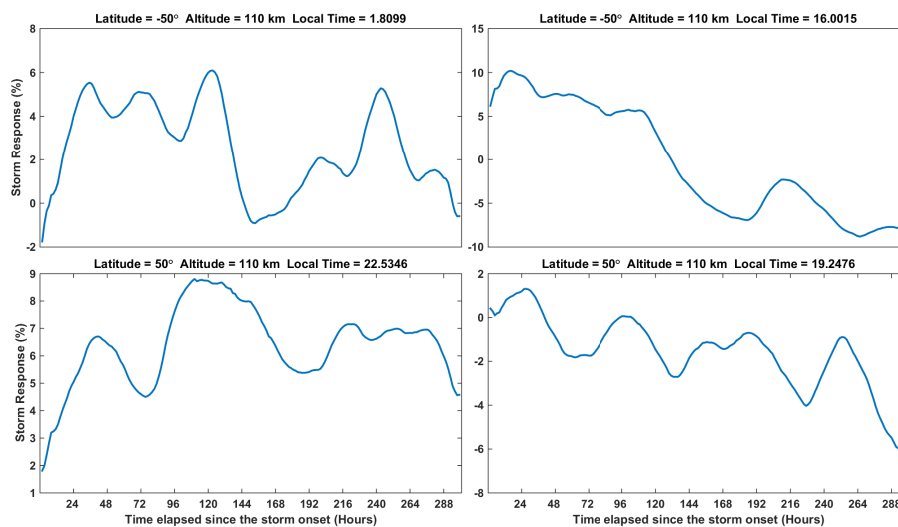


Fig. 3.13: Thermospheric storm response at 110 km altitude and 50° and -50° latitudes for the 6-May-2003 storm interval. The left and right panels in the figure represent the ascending pass measurements and descending pass measurements respectively. The local time at which SABER samples the latitude bin for the two passes are illustrated at the top of the panels.

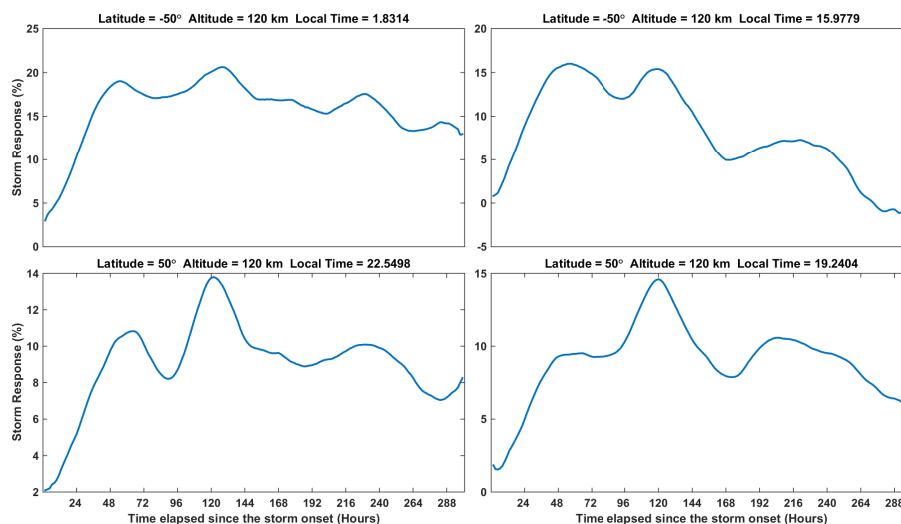


Fig. 3.14: Thermospheric storm response at 120 km altitude and 50° and -50° latitudes for the 6-May-2003 storm interval. The left and right panels in the figure represent the ascending pass measurements and descending pass measurements respectively. The local time at which SABER samples the latitude bin for the two passes are illustrated at the top of the panels.

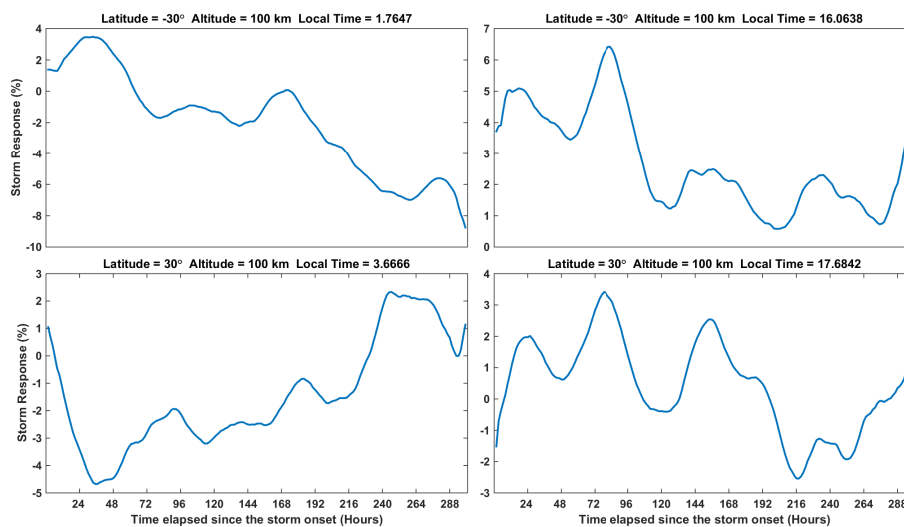


Fig. 3.15: Thermospheric storm response at 100 km altitude and 30° and -30° latitudes for the 6-May-2003 storm interval. The left and right panels in the figure represent the ascending pass measurements and descending pass measurements respectively. The local time at which SABER samples the latitude bin for the two passes are illustrated at the top of the panels.

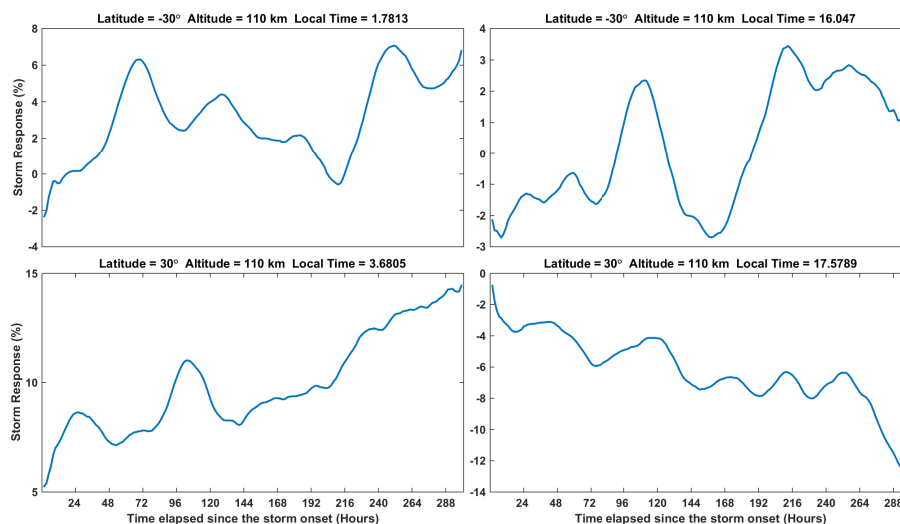


Fig. 3.16: Thermospheric storm response at 110 km altitude and 30° and -30° latitudes for the 6-May-2003 storm interval. The left and right panels in the figure represent the ascending pass measurements and descending pass measurements respectively. The local time at which SABER samples the latitude bin for the two passes are illustrated at the top of the panels.

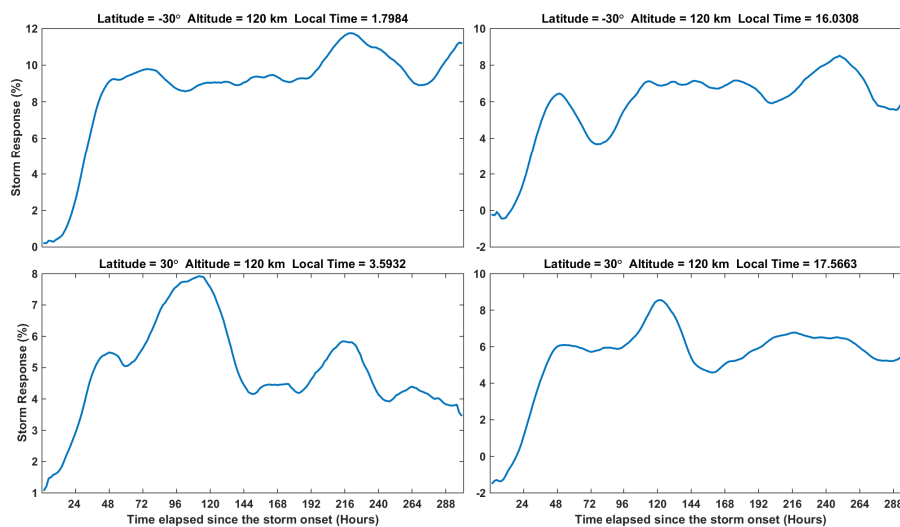


Fig. 3.17: Thermospheric storm response at 120 km altitude and 30° and -30° latitudes for the 6-May-2003 storm interval. The left and right panels in the figure represent the ascending pass measurements and descending pass measurements respectively. The local time at which SABER samples the latitude bin for the two passes are illustrated at the top of the panels.

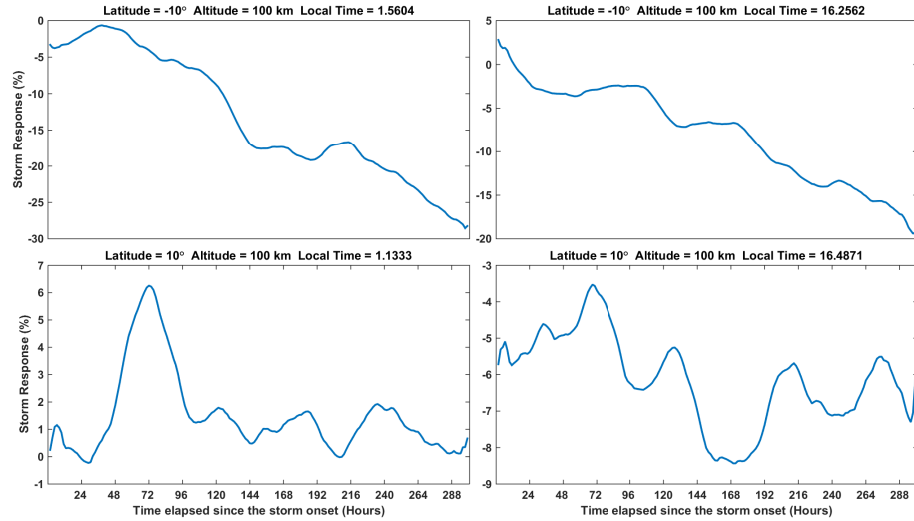


Fig. 3.18: Thermospheric storm response at 100 km altitude and 10° and -10° latitudes for the 6-May-2003 storm interval. The left and right panels in the figure represent the ascending pass measurements and descending pass measurements respectively. The local time at which SABER samples the latitude bin for the two passes are illustrated at the top of the panels.

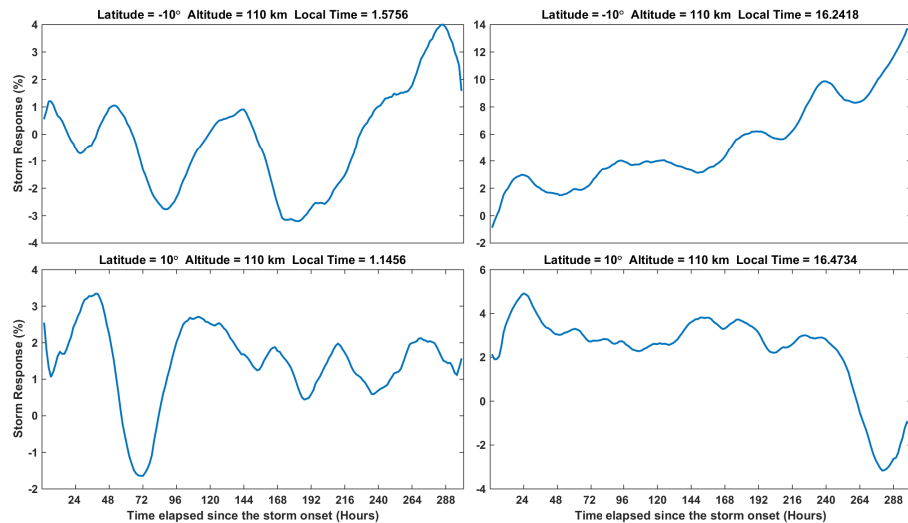


Fig. 3.19: Thermospheric storm response at 110 km altitude and 10° and -10° latitudes for the 6-May-2003 storm interval. The left and right panels in the figure represent the ascending pass measurements and descending pass measurements respectively. The local time at which SABER samples the latitude bin for the two passes are illustrated at the top of the panels.

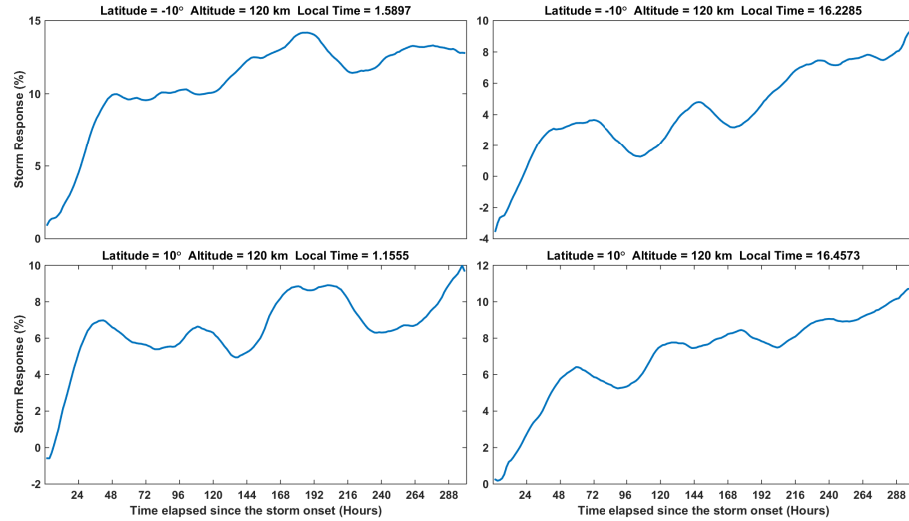


Fig. 3.20: Thermospheric storm response at 120 km altitude and 10° and -10° latitudes for the 6-May-2003 storm interval. The left and right panels in the figure represent the ascending pass measurements and descending pass measurements respectively. The local time at which SABER samples the latitude bin for the two passes are illustrated at the top of the panels.

The orbital period of TIMED sets the cadence of the observed storm response. Hence temperatures that increase from the first orbit does not necessarily mean the storm response is instantaneous but rather that the response was seen within 1.6 hours (orbital period of TIMED). We present the storm response variables for all the altitude-latitude bins whose responses were illustrated in figs. 3.9 - 3.20 and in tables 3.1 - 3.4. The storm occurrence is closer to summer solstice in the norther hemispheres, implying the summer hemisphere is north and the winter hemisphere is southern hemisphere in this case study. SABER makes measurements at two local times which were around 01:00 and 16:00 local time for all latitude bins between -30° and 70° and around 19:00 and 22.00 local time for the -50° bin. We index the storm response variables using the labels winter, summer and night and day, to facilitate the analysis of the time and magnitude response as a function of season and local time. Also, the peak response time is measured with reference to Dst and positive values of this variable indicate that peak response occurred after the peak of Dst index and negative values indicate that the peak response occurred before the Dst hit its lowest peak.

Altitude (km)	Latitude (Geodetic Coordinates)													
	70		50				30				10			
	Winter		Winter		Summer		Winter		Summer		Winter		Summer	
	Day	Night	Day	Night	Night	Night	Day	Night	Day	Night	Day	Night	Day	Night
	TIME DELAY (hours)													
100	17.6	3.2	12.8	<1.6	32	8	<1.6	8	<1.6	54.4	56	4.8	<1.6	<1.6
105	<1.6	<1.6	32	<1.6	75.2	9.6	<1.6	<1.6	<1.6	<1.6	<1.6	<1.6	<1.6	57.6
110	<1.6	<1.6	<1.6	<1.6	4.8	<1.6	8	<1.6	17.6	<1.6	<1.6	<1.6	3.2	6.4
115	<1.6	<1.6	<1.6	<1.6	3.2	<1.6	19.2	27.2	16	<1.6	8	<1.6	<1.6	4.8
120	<1.6	<1.6	<1.6	<1.6	4.8	<1.6	9.6	<1.6	<1.6	<1.6	<1.6	<1.6	3.2	<1.6

Table 3.1: Time delay observed across all latitude-altitude bins for the 06-May-2003 storm interval.

Altitude (km)	Latitude (Geodetic Coordinates)													
	70		50				30				10			
	Winter		Winter		Summer		Winter		Summer		Winter		Summer	
	Day	Night	Day	Night	Night	Night	Day	Night	Day	Night	Day	Night	Day	Night
	PEAK RESPONSE (%)													
100	6.13	5.2	2.7	5.6	3	3.9	6.4	-8.7	3.4	-3.5	-19.2	-28.2	-6.1	6.9
105	8	7.8	1.6	7.2	-7.2	7.5	6.6	9.4	-10.6	15.5	8.7	-14.7	-17.3	3.6
110	20.5	22.6	10.1	6.1	-5.8	8.8	3.4	7.1	-13.4	11.1	13.6	4	5	3
115	26.5	31	15.5	15	8.5	7.7	7.2	14.5	3.4	2.7	10.8	15.7	10.5	4.5
120	19.4	20.7	15.9	20.6	14.6	12.6	8.5	11.7	8.6	7.5	9.6	14.2	10.5	9.9

Table 3.2: Peak response observed across all latitude-altitude bins for the 06-May-2003 storm interval.

Altitude (km)	Latitude (Geodetic Coordinates)													
	70		50				30				10			
	Winter		Winter		Summer		Winter		Summer		Winter		Summer	
	Day	Night	Day	Night	Night	Night	Day	Night	Day	Night	Day	Night	Day	Night
	PEAK RESPONSE TIME (hours)													
100	184	-78.4	184	32	184	64	-32	184	-36.8	184	184	184	184	-43.2
105	-68.8	-60.8	184	20.8	184	41.6	184	-51.2	184	169.6	184	184	184	129.6
110	-70.4	-60.8	-99.2	8	184	-4.8	97.6	136	184	184	184	171.2	-91.2	-76.8
115	-51.2	-72	-49.6	11.2	-1.6	12.8	134.4	184	136	-78.4	184	184	184	182.4
120	-48	-70.4	-59.2	12.8	4.8	6.4	134.4	105.6	6.4	-64	184	72	184	184

Table 3.3: Peak response time observed across all latitude-altitude bins for the 06-May-2003 storm interval.

Altitude (km)	Latitude (Geodetic Coordinates)													
	70		50				30				10			
	Winter		Winter		Summer		Winter		Summer		Winter		Summer	
	Day	Night	Day	Night	Night	Night	Day	Night	Day	Night	Day	Night	Day	Night
	END-OF-STORM RESPONSE (%)													
100	6.1	3.2	2.7	0.1	3	-1.6	2.4	-8.7	3.1	-3.6	-19.3	-28.2	-6.1	-0.5
105	7.9	1.8	1.6	0.3	-7.2	-0.2	6.6	3.9	-10.7	14.8	8.7	-14.7	-17.3	2
110	-2.6	-0.8	-8.7	-0.6	-5.9	5.4	3	6.8	-13.4	11.1	13.6	1.6	-1	-0.3
115	-18.1	-6.8	-13.7	6.5	3.8	6.4	7.1	14.5	-0.2	-0.9	10.8	15.7	10.5	4
120	-15.5	-10.2	-0.1	12.9	6.5	8.1	6.4	11.2	4.9	3.5	9.6	12.8	10.5	9.9

Table 3.4: End-of-storm response observed across all latitude-altitude bins for the 06-May-2003 storm interval.

Polar Latitude Response

The high latitude bins (-70°) which are subjected to *in situ* heating from the incoming magnetosphere energy, exhibit an immediate response at all altitudes, except at 100 km. The 100 km bin comprises data from 97 to 102 km and the magnetosphere energy converging at these altitudes is mostly from particle precipitation [27]. We speculate the delay observed in the temperature increase has to do with particle precipitation being not as efficient as Joule heating in causing *in situ* heating at 100 km and thereby hinting that the energy is most likely transported from other altitudes.

The peak responses in the high latitude bin were highest at 115 km in this case study. Given that we don't have the measurements of entire thermosphere below 200 km, which corresponds to the peak energy convergence, we cannot associate this peak response altitude as the altitude of highest energy convergence.

We can also see that peak response times are all negative in the region of direct heating, indicating that the high latitude bin does not get energized beyond a certain point in the storm interval, despite continued storm energy deposition. This could be attributed to the initiation of transport process set up to quench the global temperature gradients, following the storm onset. This could be responsible for tempering the temperature from increasing in proportion to the intensity of the storm energy.

The end-of-storm interval response indicates complete recovery to the tune of over-cooling at all altitudes corresponding to *in situ* heating. However, the 100 km altitude bin which exhibits a time delay in response does not recover completely back to its quiet time value in the 24 hours following the storm end.

Sub-polar Latitude Response

The sub-polar latitudes exhibit a time delay of less than 1.6 hours to few tens of hours. The largest time delay for the sub-polar latitude bins are preset at altitudes bins of 100 km and 105 km. The distribution of time delays at a given height is not an increasing sequence from poles to equator. This could be hinting that compression heating from strong downward winds that are triggered by circulation cells in the auroral regions set up at the

onset of the storm to quench the temperature gradients, may be primarily responsible for the initial equatorward transport. Instead, if it were dominated by horizontal advection, we would see a smooth increase in time delay at a given altitude, as we progress from the poles to the equator, which is not the case here. However, it does not mean that horizontal winds or conduction are not playing a role in energy transport, but rather that they are not the dominant transport process for the initial phase of the equatorward transport at these altitudes. We also need to be mindful that drawing any conclusions on transport processes with certainty requires corresponding measurements of other thermosphere state variables.

The peak responses are both positive and negative, with some latitude-altitude bins exhibiting magnitudes comparable to polar responses. These negative signs indicate that the largest change in some latitude-altitude were due to energy divergence triggered by the storm energy transport.

The peak response times are mostly positive indicating that the latitude-altitude bins continue to increase for several hours after Dst index starts its recovery. The latitude-altitude bins do not seem to exhibit a correlative behavior between time delay and peak response time, indicating that longer peak response times are not necessarily indicative of delayed response and *vice versa*.

When peak response times for each latitude-altitude bin are observed in tandem with its corresponding end of storm response and peak response, we can discern that the recovery from the storm energy is yet to be triggered. This suggests that in the case of prolonged storms as the one under consideration, the recovery of the thermosphere at lower latitudes and altitudes which are not subjected to *in situ* heating, could perhaps be longer than the current assumption of 24 hours.

3.5.1 Season and Local Time Influence on Thermospheric Storm Response

The TIMED satellite makes observations of both winter and summer hemispheres and at two local times corresponding to the ascending and descending pass for each latitude-altitude bin. Hence we use the storm response to test if our current understanding of season and local time influence on the storm response can sufficiently explain the storm response

observations.

The influence of seasons and local time on the storm response magnitude has been linked to the Joule heating efficiency. It is believed that Joule heating efficiency is greater in the presence of lower EUV radiation and hence winter hemispheres and nightside are expected to exhibit higher storm induced changes [48]. In this case study, we see this to be true for only limited altitude-latitude bins. For instance above 110 km, the nighttime temperatures are higher than daytime temperatures for the polar latitude bins. Similar winter *vs.* summer surges are seen in altitude bins of 115 and 120 km, with nightside winter exhibiting the highest response in those bins. However we do not see such a consistent pattern of summer *vs.* winter and night *vs.* day in other altitude-latitude bins.

The effect of season and local time on the efficiency of storm energy transport is also explained with similar undertones [48]. It is hypothesized that the hemispheres and local times with default circulation being equatorward aid the equator-bound storm energy, resulting in faster storm energy transport in such cases. The default circulation during quiet times is from summer to winter hemisphere, poles to equator in night, and equator to poles during day. Hence summer hemisphere and night are expected to see faster equatorward convergence of storm energy [40] than winter and day respectively. We examine if this is true by observing the delay times. We observe that the storm response between the day and night are random in their trend.

We would like to draw attention to a similar study of CHAMP density data that was carried out to observe the effects of local time and seasons for three different storms [49]. The authors of this case study report the absence of a consistent pattern in the local time and season effect, leading them to speculate that the local time and season effects are multifaceted, and that the variation of local time and seasons are compounded by other factors.

The variation observed in CHAMP density case studies, as well as in this case study, point to the necessity of observing more than a few isolated storms. Also, given that solar cycles and storm intensity also influence storm responses, we carry out a statistical study of

storms to understand the influence of all of these variables on the thermospheric response to storms, in the next chapter.

3.6 Summary

In this chapter, we illustrated the lower thermospheric storm response analysis using SABER data, where the storm response was deduced using the quiet time variation model. A scheme to represent the so-derived storm response, using variables which would help in conducting large scale statistical studies, was devised. The four storm response variables, namely, peak response, end-of-storm response, delay time and peak response time, were derived for a single storm interval to illustrate how these variables could be used to study the attributes of the storm response. The key findings from this case study were:

- The peak response was highest above altitude of 110 km.
- The delay times are indicative of complex horizontal and vertical transport processes which take from an hour to tens of hours of time for sub-polar energy transport.
- The deal times at 100 km was always more than an orbit, indicative of transport from other altitudes and not of *in situ* heating.
- The thermosphere does not indicate complete recovery in the assumed 24 hours post magnetosphere index going back to quiet time values.
- Current understanding of factors influencing storm response were challenged, with the storm response analysis hinting at a more complex, multifaceted nature of the storm response.

CHAPTER 4

STATISTICAL STUDIES OF THE STORM TIME THERMOSPHERE USING SABER TEMPERATURES

In the current age of big data, we are both challenged and rewarded with the exuberance of the information that is dispensed by large data sets. The operation of various aeronomy missions hitting the decade mark has put us in the sweet spot of big data, by rewarding us with fresh insights on Geospace, without having to worry about the logistics of the big data yet. These decade-long-and-growing datasets allow experiments involving multiple instances of the phenomena under study, referred to as a statistical study.

Statistical studies are classified as being descriptive or inferential, based on the nature of the question posed by the study [102]. A descriptive study, also referred to as exploratory analysis, is aimed at finding the properties of the dataset such as: maximum, mean, probability distribution of the dataset etc., which summarize the data. Inferential studies could be of two types: inductive studies and predictive studies. Inductive studies test various hypothesis by using the dataset as a testing tool, and estimate the conclusions that can be drawn about the information contained within the data. They involve using independent variables or predictors whose influence on the data set being studied, known as the dependent variable, is assessed. Predictive studies build on top of the inductive studies to extrapolate the induced information and predict outcomes about the population of the data set from the sample set.

Statistical studies of the thermosphere, inferential or descriptive, have been rare owing to the presence of limited long term datasets. Prior to the era of big data and global observations, ground based measurements provided statistical view point from a regional perspective on the Geospace environment. However, with long term operation of satellite missions like CHAMP, GRACE and TIMED, we are now in possession of larger sample sizes of aeronomy state variables; opening doors to new questions on global perspectives of

the geospace that could be answered using statistical studies.

In this chapter, we conduct the very first descriptive and inferential studies of the lower thermospheric temperature response to storms. We use decade-long thermospheric global storm responses, obtained from the SABER instrument on-board the TIMED satellite. We investigate the storm response variables that were defined in Chapter 3 from a statistical standpoint for our sample set of storms and summarize their properties. We then conduct inferential studies that test the relative significance of the quiet time vs. storm time variations and gauge the influence of the variables influencing the storm response. These variables influencing the storm response which we refer to as storm response predictors include: local time, seasons, solar cycle, storm intensity and length of the storm. We finally conclude by summarizing our findings.

4.1 Sample Set for the Statistical Studies

The sample set consists of storm responses calculated for all the storm intervals that occurred between 2002 and 2010 for which SABER data was available. There were 145 such storm intervals, which are illustrated in fig. 4.1.

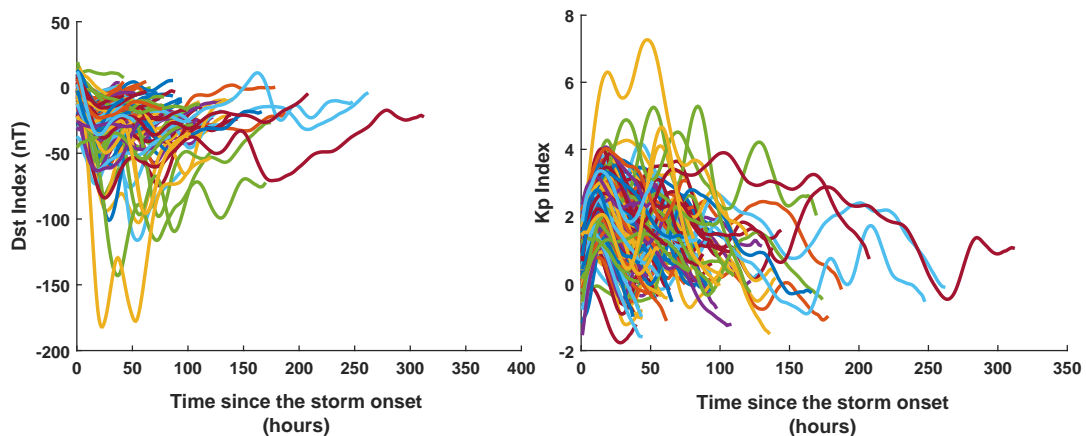


Fig. 4.1: Sample set of the storm intervals, illustrated using geomagnetic indices. The left and the right panel represent the Dst and Kp indices respectively for all the storm intervals, referenced with their respective quiet interval Dst and Kp indices.

We illustrate the thermosphere response for all the storm intervals that are used in this statistical study in fig. 4.2.

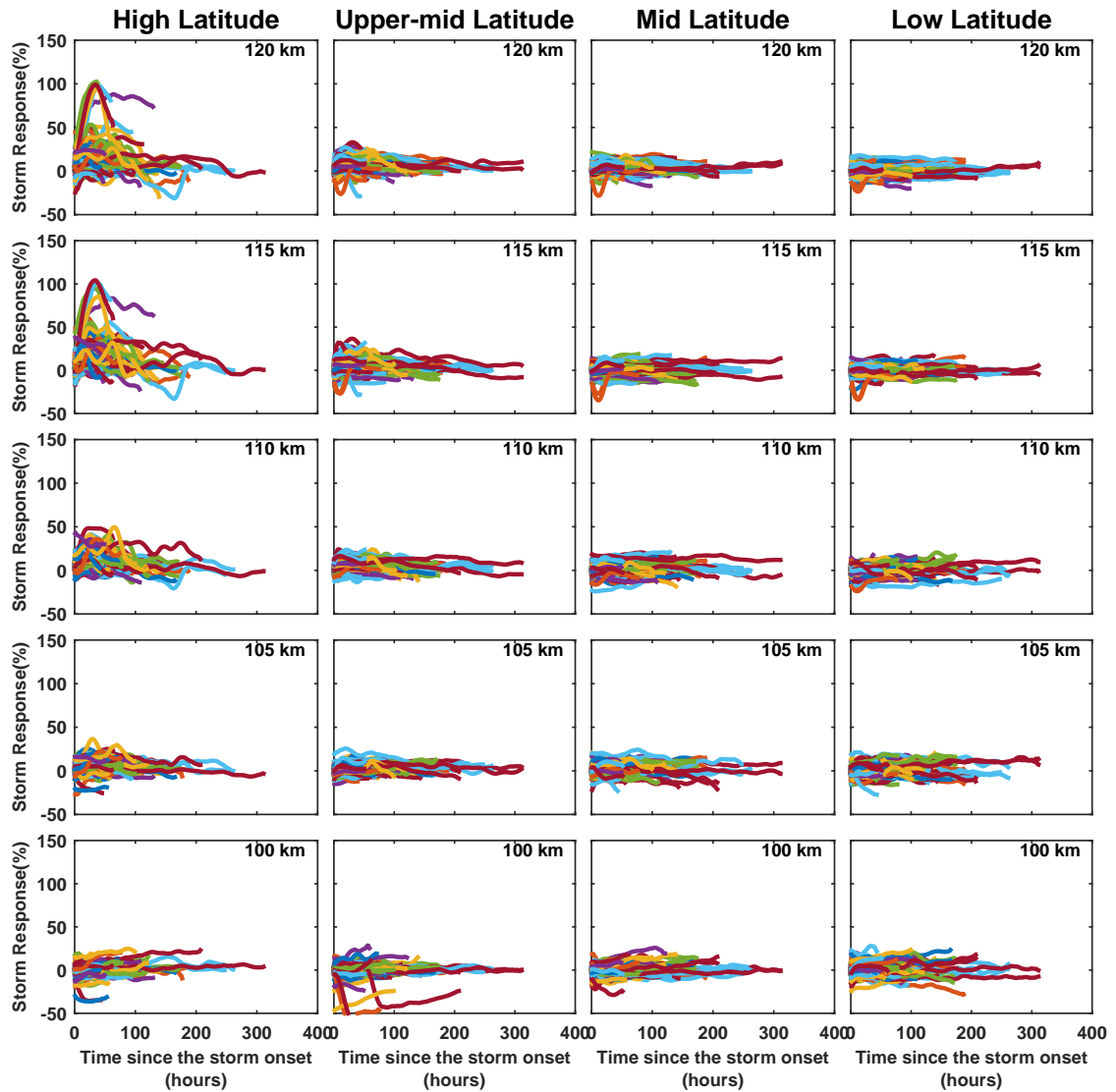


Fig. 4.2: Sample set of the storm response across all latitude bins for the 100-120 km altitude range which is used for the statistical study of the thermosphere storm response.

Each unique combination of storm response predictors forms one storm instance or storm sample of our sample set. SABER measures every latitude-altitude bin at two different local times for each orbit. Hence each storm interval will give rise to two storm

samples for every unique altitude-latitude bin. This is because we are analyzing the influence of seasons, local time and solar cycle in addition to the storm type. Hence although the values of storm interval, seasons and solar cycle, are the same, the two different local times at which the global storm response is measured, translates into two separate storm analysis or two separate storm samples.

So far we analyzed every altitude-latitude bin separately (altitude-latitude bins are 5 km long and 20° wide bins and the average response across such a bin is used). However in this chapter, for a given altitude, a latitude and its conjugate will be labeled as two samples of a single bin and their statistical properties will be collectively analyzed. We define conjugate latitude as a pair of geodetic latitudes which are equal in value but belong to the opposite hemispheres. For instance, -20° and 20° latitude bins form a pair of conjugate latitude bins.

We collectively analyze the conjugate latitude bins because the philosophy behind the storm response in both hemispheres is the same - energy deposited at polar latitudes and carried towards the lower latitudes by various transport process from the polar latitudes. The storm response variables measure how much and how soon the storm energy converge across these various bins. The conjugate sub-polar bins in both hemispheres are equidistant from the respective polar bins. Any asymmetry in the Joule heating and particle precipitation patterns between the two hemispheres can cause a corresponding asymmetry in the *in situ* heating pattern of the two hemispheres. However, the latitude bins used in this study are 20° wide and the storm response is a zonal average of the response seen across this bin. The large bin sizes and zonal averaging will hence permit the two conjugate hemisphere latitude bins to be considered to be free from any bias from the asymmetry of the storm energy in the two hemispheres.

In in this case of longitudinally averaged (zonal mean) response, the difference in the characteristics of the storm response at these two conjugate latitude bins will be due to the difference in the solar inclination angle (seasons) and the local time at which the satellite samples the two hemispheres. These differences will serve as different values of the predictors

(local time and seasons) of the storm response. Hence for each storm interval, the two conjugate latitudes will form four storm samples identified by a unique combination of local time and season.

Using this principle, the latitude bins for each altitude bin will now be labeled as follows: polar latitude bin comprising of 70° and -70° bins, upper mid latitude bin consisting of -50° and 50° bins, mid latitude consisting of 30° and -30° bins and low latitude bin consisting of -10° and 10° bins. Note that SABER measurements cover polar latitude in only one hemisphere for any given storm interval, with this hemisphere being dependent on the yaw cycle interval that the storm interval is part-of.

As stated earlier, our sample set comprises 145 storm intervals. Hence the polar latitude bin for each of the five altitude bins will have 290 number of samples available for the statistical study. The sub-polar latitude bins with both hemisphere coverage will hence have 580 samples in each of the three latitude bins defined for each of the five altitude bins. This widespread sample set of almost a decade worth of storms has been chosen to ensure we have ample instances of storms under all seasons, local times, phase of the solar cycle and storm intensities. The larger data set is chosen with the assumption that the resulting sample size will have larger statistical power and facilitate testing of the relative importance of each of the storm response predictors.

The sample set described above and derived from the storm intervals shown in fig. 4.1, is described using a plot matrix representation in fig. 4.3. It illustrates the distribution of the storm predictors that constitute the sample set for our statistical study. The main diagonal elements of the plot matrix represents the individual distribution of the variables and the rest of the elements illustrate their distribution as a function of other variables. In the plot matrix of fig. 4.3, the solar cycle phase is represented by the variable 'year'. The variable 'day of year' represents the seasons and the rest of the variables being self explanatory. The earlier years upto 2005 include the data corresponding to solar maximum of Solar Cycle 23 with the later part corresponding to solar minimum comprised of declining part of solar cycle 23 and onset of solar cycle 24. As expected, the higher intensity storms,

illustrated by lower Dst values, are more common during the solar maximum.

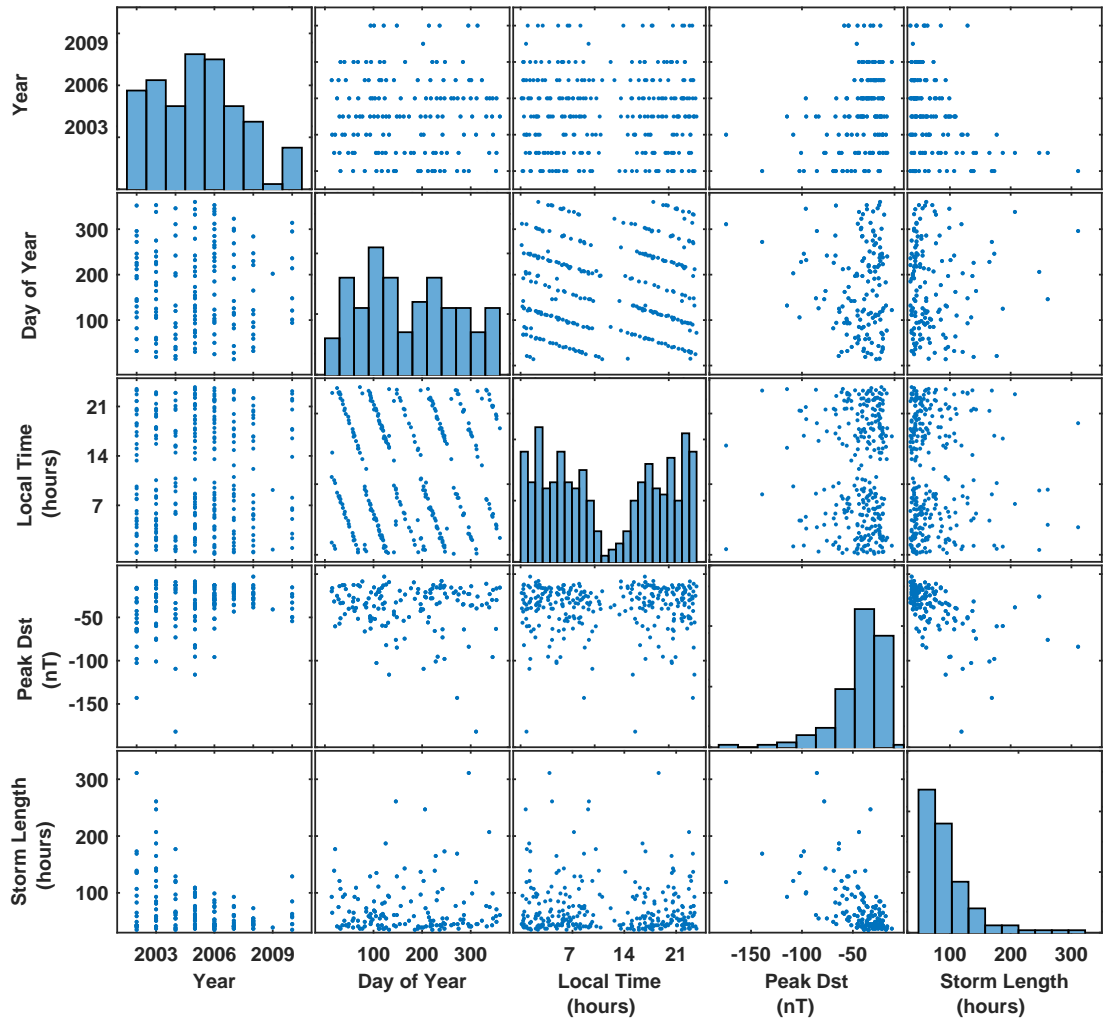


Fig. 4.3: Plotmatrix illustration of the storm predictors constituting our sample set. The plot matrix illustrated here is representation of the 50° latitude-altitude bin.

However, lower Dst or intense storms with longer length are limited and having sporadic occurrences along the domain of other variables. The seasons and local time are well represented with reference to both solar cycle and storm intensity, with the exception

of intense storms. The limited measurements around noon is an artifact of the SABER instrument sampling requirement that was explained in Chapter 1.

4.2 Descriptive Statistics of the Lower Thermosphere Storm Response

The descriptive statistics of the thermospheric storm response will shed light on the range and distribution of the storm response of the lower thermosphere temperatures. The storm response variables defined in Chapter 3, namely, delay time, peak response, peak response time and end-of-storm temperature, will be calculated for each of the storms of our sample set. They will be collectively used to statistically summarize the storm response of the lower thermosphere. We plot the storm response variables for all the storm intervals of our sample set at each latitude-altitude bin in fig. 4.4 and fig. 4.5. Hence each box plot in fig. 4.4 and fig. 4.5 summarizes the global lower thermospheric magnitude response and time response to storms for an altitude-latitude bin respectively.

The box plots in the fig. 4.4 and fig. 4.5 represent the frequency distribution with the red horizontal line highlighting the median. The box extremities represent the 25th and 75th percentile of data and hence the box represents the range of the 50% of the data. The whiskers of the box plot, depicted in black, represent the 5th and 95th percentile of data and hence data contained within the two whiskers account for 90% of the total data. The red '+' signs are the data extremities which account for remaining 10% of the data.

We can see from the top panels of fig.4.4 that the highest peak response occurs at polar bins at altitude bins of 110 km and higher. The storm energy converges predominantly in the form of particle precipitation at altitudes below 110 km. The intensity of the storm response seen at these altitudes in fig. 4.4 is markedly lower than the higher altitudes of combined Joule heating and particle precipitation. We can also observe that the temperature response at the sub-polar latitudes do not exhibit strong altitude dependence. In general, the sub-polar latitude bins do not exhibit a large dispersion of the storm time temperature variations. We also observe a few negative peak responses, with sub-polar latitudes having higher frequency of these than the polar latitudes. These are indicative of a decreasing trend morphology of storm response that was discussed in Chapter 3. As explained earlier,

such negative peak responses could be attributed to the storm energy not persisting in the given latitude-altitude bin.

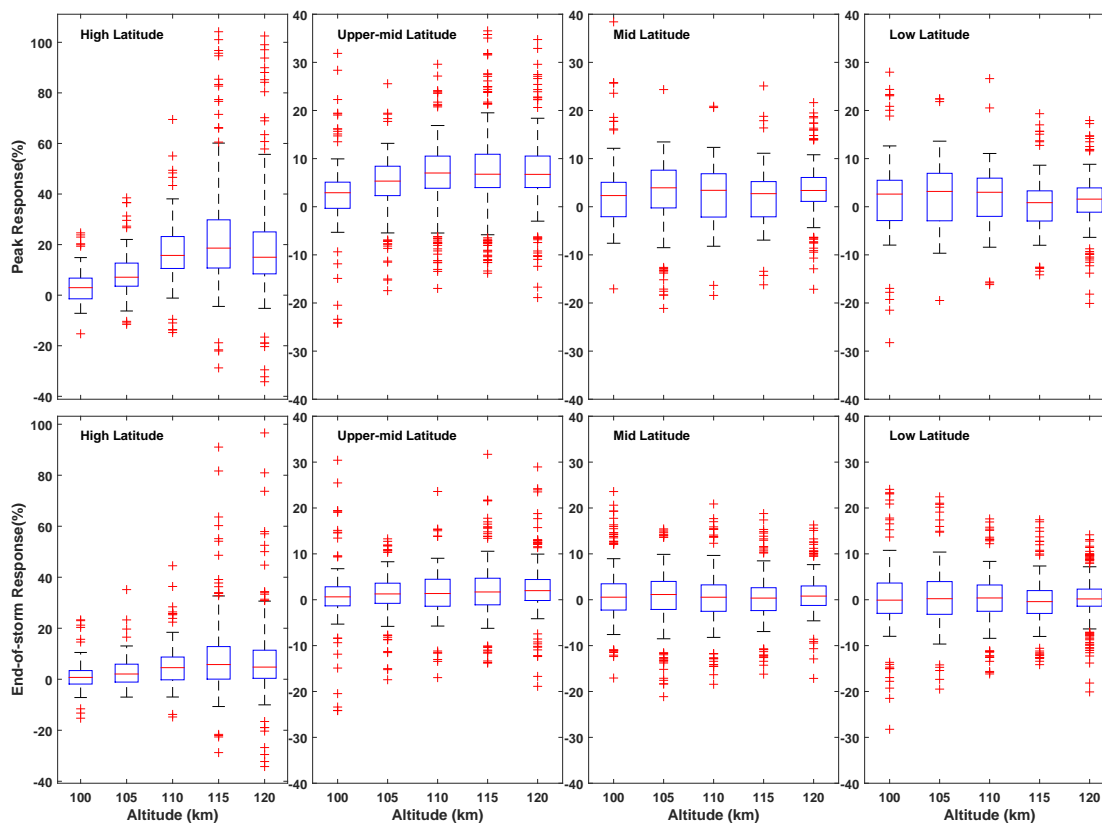


Fig. 4.4: Illustration of global magnitude response to geomagnetic storms as a function of altitude for each of the four latitude bins. The top panels represent the magnitude response using peak response and the bottom panels using end-of-storm response.

The end-of-storm response, as seen from the bottom panels of fig. 4.4, are mostly positive for the high latitude bins and the rest of them have equal instances of both positive and negative values as indicated by zero medians. Although non-zero values indicate incomplete recovery for all storm morphologies, we need to be aware of confidence factors that can be assigned to such an interpretation of end-of-storm response. It was earlier seen in Chapter 2 that random variability exists during quiet time intervals. This is the variability that exists between two quiet intervals of SABER measurements after all known causes of variability are removed. This variability, as illustrated in Chapter 2 and Appendix A, is seen to be

have maximum values of 10% for sub-polar bins and around 40% for the polar bins. Hence when labeling the end-of-storm response as complete recovery or otherwise, we need to be mindful of these random variations acting as confidence intervals. On accounting for these random variations as confidence intervals, the data in fig. 4.4 is suggestive of incomplete thermospheric recovery to occur in about 10% to 25% of our sample set.

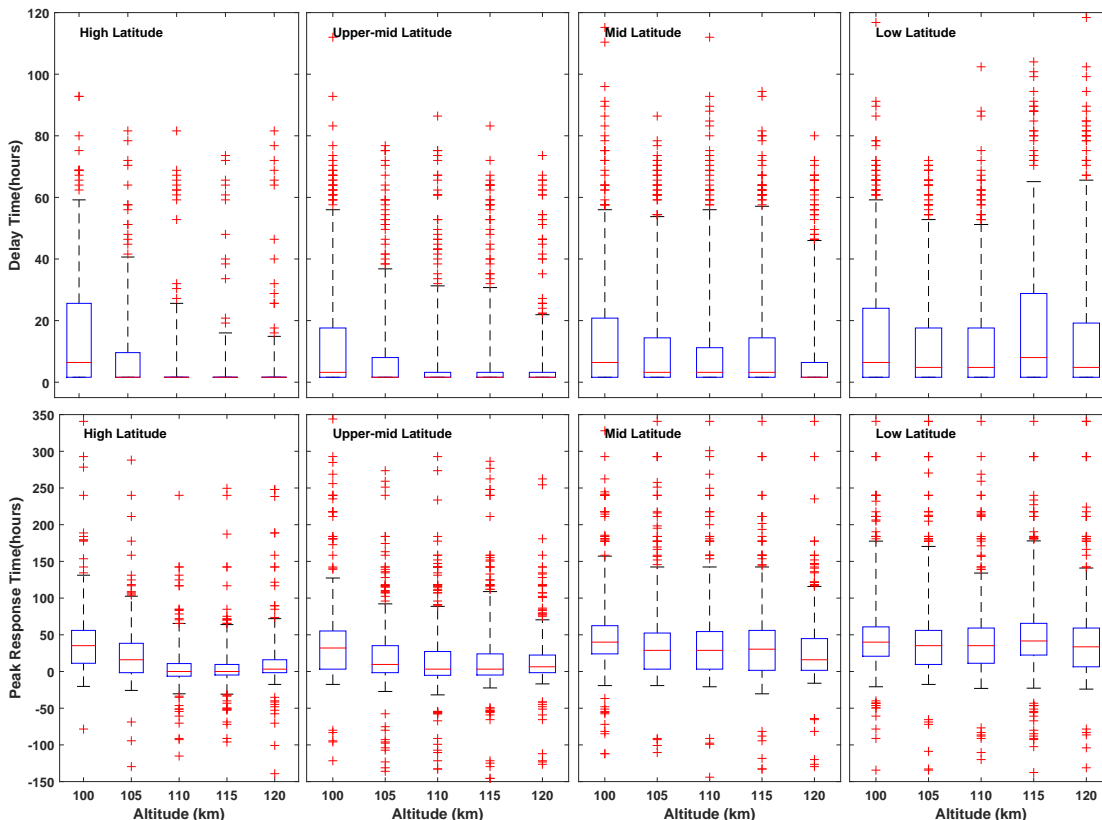


Fig. 4.5: Illustration of global time response to geomagnetic storms as a function of altitude for each of the four latitude bins. The top panels represent time response using delay time and the bottom panels using peak storm response time.

As seen in the top panels of fig. 4.5, majority of the high latitude bins at altitudes of 110 km and higher have delay times of 1.6 hours. This trend was seen in 75% of the sample set as discerned from the absence of any outliers south of the collapsed box. The rest of the bins exhibited delay times having medians close to 5-8 hours. It can be seen that 75% of the samples across all latitude-altitude bins have delay times less than a day and the remaining

samples exhibit delay times ranging from 2-4 days. The largest box sizes and values are seen for the 100 km altitude bins. The presence of this behavior and larger than an orbit of delay time for all the samples at this altitude bin could be due to the in-efficiency of *in situ* heating from storm energy at altitudes lower of 105 km. These effects are hence indicative of the energy transport from higher altitudes being the primary source of storm energy at these lower altitudes.

The peak response times for 75% of the samples across all latitude-altitude bins are positive as seen in the bottom panels of fig. 4.5. This indicates that the peak of the storm response trails behind the storm energy peak for majority of the storms. The small box sizes and zero median values for the high latitude bins at altitudes of 110 km and above, are reflective of the polar bin storm morphology to be the same as the storm energy morphology. The sub-polar bins trail behind the storm energy with their median being close to one to two days. The negative values of peak response time represent those samples where the storm response peaks before the storm energy. They represent instances where the storm energy does not persist and is instead transported to other thermospheric regions.

4.3 Inferential Statistics of the Lower Thermospheric Response to Storms

The storm response summarized in the previous section corresponds to multitude of predictor conditions as illustrated in fig. 4.3. The variation of the predictor values across the sample set are the primary source of the variation observed across the storm response variables illustrated in fig. 4.4 and fig. 4.5. We use this exhaustive data set and employ inferential techniques on them to assess the nature of the predictor influence on the storm response.

As argued in Chapter 3, the practice of testing the role of individual predictors while keeping the remaining predictors constant, does not facilitate explaining the observed storm response. This is most probably due to the multivariate nature of the storm response. In this section, we test the influence of all the storm response predictors simultaneously and investigate if the storm response is indeed a multifaceted phenomenon. The key to conduct such a multivariate study is to investigate the storm response under exhaustive

combination of predictor values. The decade-long dataset illustrated in fig. 4.3 renders such an investigation possible.

We conduct this multivariate study by investigating the statistical dataset as an inductive problem controlled by a combinatorial configuration of predictor space. This means we isolate the associations of predictors and storm response variables and induce the role of predictors from this association. The combinatorial space stems from performing a search through all possible combinations of predictors.

We represent the contribution of a storm response predictor P_m to the thermospheric storm response as a combinatorial space C_{P_m} , which is defined as

$$C_{P_m} = \binom{n}{n} \binom{n}{n-1} \binom{n}{n-2} \dots \binom{n}{2} \binom{n}{1} \binom{n}{0}, \tag{4.1}$$

where ‘n’ is the size of the domain of P_m . The structure of the above equation highlights that the entire range or some or none of the entries from the predictor domain could be contributing to a unique value of storm response variable. Since we investigate all of the five storm predictors simultaneously, a storm response feature is described as being the resultant of some or all of the combinatorial spaces of the five storm predictors, represented as $\prod_{m=1}^5 C_{P_m}$, with C_{P_m} being eq. 4.1.

We scan the storm response as binned by each combinatorial space of $\prod_{m=1}^5 C_{P_m}$ to discern what combination(s) of predictors are associated with a certain type of response. Using this, we induce the role of predictors in describing the features of the storm response. Since the storm response is expressed using the storm response variables, each of the storm response variables will constitute a separate search of the combinatorial space. The combination space defined above, based on the range of the predictor domains could potentially be a vast search space comprising of hundreds of combinatorial subspaces, thereby warranting the usage of an automated search algorithm. For instance, if we consider 5 variables with domain sizes 2, 2, 3, 3 and 3, the total combinatorial space that we will have to scan through will be $\prod_{m=1}^5 C_{P_m} = 2 \times 2 \times 9 \times 9 \times 9$

Such inductive problems of mining for information in data from a large search space

can be best solved using machine learning algorithms. Machine learning algorithms are methods which can learn from data and make data-driven decisions and predictions [103]. In our case, the machine learning algorithm will be set up to search the combinatorial space of storm response predictors to find subspaces which are associated with a certain behavior of storm response variable.

The choice of the algorithm is driven by the attributes of the predictors and the response and includes factors such as distribution, type of data and the presence of covariance in data [104,105]. In the case of storm response predictors, there is a presence of covariance between storm strength, duration and solar cycle phase. The distribution of the storm predictor domains as seen in fig. 4.3 is not normal. Although our data set is comprised of discrete numeric data, it is best that we categorize it into groups before applying the machine learning algorithm. The purpose of grouping the data into categories is to assess the statistical power of our data set. Given that no statistical study has been carried out on SABER data to investigate any of the storm response features, we do not yet possess an understanding of the level of information our data set can unearth. In other words, we would first like to classify our findings into a broader set successfully, and then set out to refine it further into smaller subsets to explore causative factors. In addition, we also categorize the storm response predictors since current approach of storm analysis involves qualitative treatment of these predictors. Thereby testing the fidelity of any of the current hypothesis of the storm time thermosphere would be possible.

Hence based on the above mentioned attributes of our data set, we decide to use decision trees [104,105]. Decision trees have the advantage of working with both classification and regression. Hence if the statistical power of our sample set permits, the same setup can be expanded to conduct this endeavor using discrete data to refine our understanding of the storm responses. In addition, the graphical nature of the decision trees makes them suitable for reasoning since each step in the process of deducing the information from the data will be available for visual inspection and analysis. Other machine learning algorithms are intuitively designed for prediction and hence are not the best choice for inductive reasoning

problem such as ours.

4.3.1 Decision Trees for Storm Response Inference

Decision trees scans the combinatorial subspace of predictors (inputs) to find subspaces which will serve as the basis for partitioning the data into smaller subsets of homogeneous data [105]. In this context, homogeneity refers to the amount of data in a subset which have the same value of response variable (output). The computation of such subsets of predictor(s) along with the predicted response are recursively carried out till the homogeneity of data in a subset can no longer be improved. The predictor subspace along with the predicted response variable value are collectively referred to as a decision or a pattern. These decisions due to the recursive nature of the subset selection, when illustrated graphically, resemble a tree, giving the algorithm the name decision tree. The confidence that can be assigned to each decision of the tree is dependent on the percentage of inhomogeneous data. It is expressed in percentages, either between 0 to 100 or as normalized values between 0 to 1. A decision with a inhomogeneity value of 0 translates into 100% confidence assigned to it.

Categorizing Data for the Storm Response Decision Tree

We convert the storm response predictors into categorical data sets as follows:

- The solar cycle phase, indicated by the year of the storm occurrence, is grouped into ‘solar maximum’ and ‘solar minimum’. Data from years 2002 to 2005 are categorized as ‘solar maximum’ and those from 2006 and onwards as ‘solar minimum’.
- The variable day of year which represents seasons has been grouped into ‘winter solstice’, ‘summer solstice’ and ‘equinox’. A storm instance is grouped into either of these three seasonal groups based on its proximity to each of the groups, with the nearest group being assigned to the instance.
- The variable local time has been grouped into ‘day’ and ‘night’.

- The variable storm intensity has been grouped into ‘low’, ‘medium’ and ‘high’. The peak Dst which is less than -25 is taken as low, peak Dst between -25 and -75 as medium and anything lower than -75 is considered as high.
- The storm duration is again grouped into ‘short’, ‘intermediate’ and ‘long’. The storms with duration less than 25 orbits are defined as short, between 25 and 50 orbits as intermediate and anything more than that as a long duration storm.

We illustrate the predictor space in terms of the categories defined above using piecharts in fig 4.6.

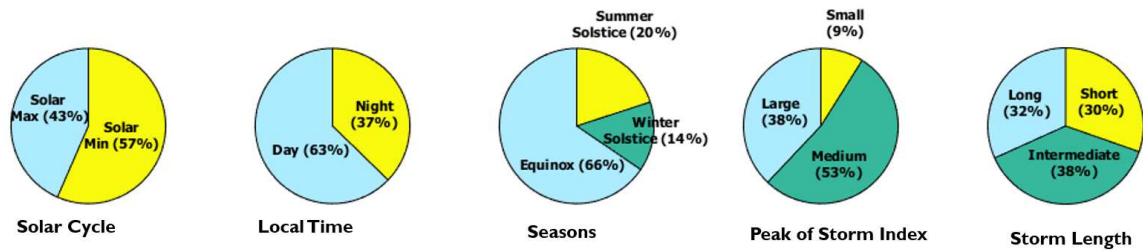


Fig. 4.6: Illustration of categorization scheme for storm response predictors which are employed in the decision tree algorithm investigation of the storm response - storm predictor relationship.

We group the storm response variables will into the following categories:

- The peak response will be grouped into three quantiles.
- The delay time will be grouped into two groups, labeled ‘delay present’ and ‘delay absent’.
- The peak response time will be grouped into ‘saturation’ and ‘no saturation’. Saturation refers to those with negative peak response times, indicating that the response peak saturates and does not increase even-though the storm energy is increasing. The opposite of which is the no saturation.

- The end-of-storm response will be grouped into ‘complete recovery’ and ‘incomplete recovery’ which will indicate if the temperature recovered back to pre-storm values or otherwise. The complete recovery is taken as those with positive values.

We illustrate the storm response expressed in terms of the categories defined above using piecharts in fig 4.7.

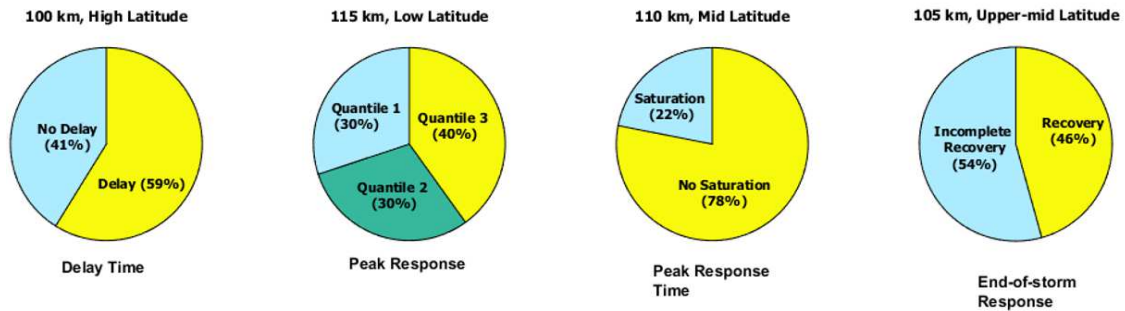


Fig. 4.7: Illustration of categorization scheme for storm response variables used in decision tree algorithm to study the storm response - storm predictor relationship. The latitude-altitude bins corresponding to each of the storm response variables that are illustrated here are labeled at the top of the pie charts.

Using these categorized predictors and responses, we apply decision tree algorithm to answer each of the following questions for every latitude-altitude bin.

- What values of storm response predictors result in the thermosphere to exhibit a delay in the response to storms?
- What values of storm response predictors result in the thermosphere to exhibit complete recovery?
- What values of storm response predictors are associated with each of the three quantiles of the peak response of the storm?
- What values of storm response predictors result in the saturation of storm response peaks?

We use the decision tree algorithm from the machine learning toolbox in the MATLAB software package to perform this analysis. We present the decision tree and their performance metrics in fig. 4.8 to fig. 4.11 for limited instances of latitude-altitude bin. The predictor variables in these figures are represented as follows: solar cycle is represented as SC, seasons as DOY, local time as LT, storm height as StH and storm duration as StD, in the decision trees. The storm response predictor categories are represented using numeric values in the figures. Use of these numeric values to represent the predictor categories are an artifact of MATLAB decision tree set up. For the predictor SC, category 0 refers to solar maximum and 1 refers to solar minimum. For LT, category 1 refers to day and 2 refers to night. For DOY, category 1 refers to equinox, 2 refers to winter solstice and 3 refers to summer solstice. The categories 1, 2 and 3 for the predictor StH refer to small, intermediate and high respectively. Finally, for StD, categories 1, 2 and 3 refer to small, medium and long respectively.

In the decision trees illustrated in fig. 4.8 to fig. 4.11, the triangles are called the classification nodes. The predictor at the top most node also called the root node, corresponds to the predictor partition which accounts for the maximum amount of variability in the dataset. Note that decision trees use greedy search approach and hence using the hierarchy of decision tree nodes to rank the significance of predictors might not be accurate. Other feature selection algorithms need to supplement the decision tree to rank the predictors accurately in the order of importance. The nodes represented by filled circles that are found at the bottom of the decision trees are called leaf nodes. The path between a root node and a leaf node corresponds to a single decision or a single pattern. In this study, pattern refers to finding a storm predictor category (categories) that are most likely to result in a certain category of a storm response variable. The amount of inhomogeneity associated with each decision is represented in red at the bottom of each decision of the tree. The normalized percentages between 0 and 1 are used here to represent the inhomogeneity. As stated earlier, higher value of inhomogeneity translates into lower confidence in the decision.

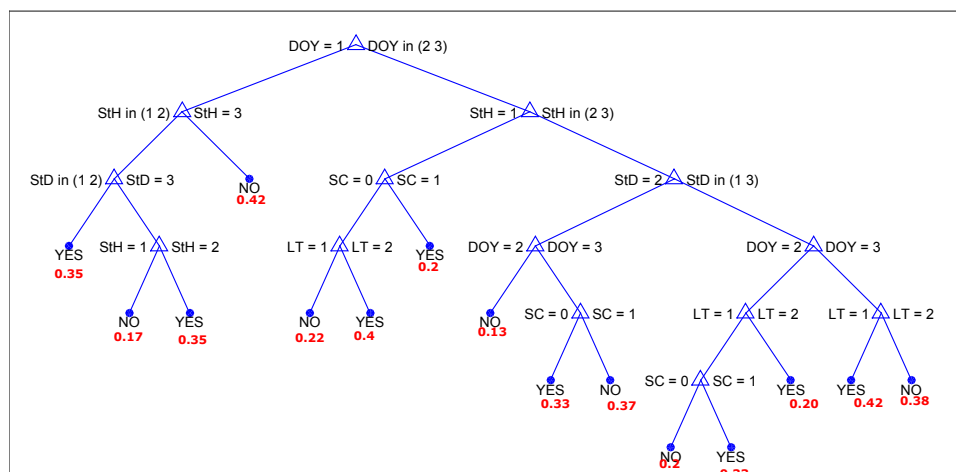


Fig. 4.8: Decision Tree for delay time classification for 100 km altitude and high latitude bin. The YES and NO represent the presence and absence of time delay. The inhomogeneity associated with each branch is illustrated at the bottom of the branch in red.

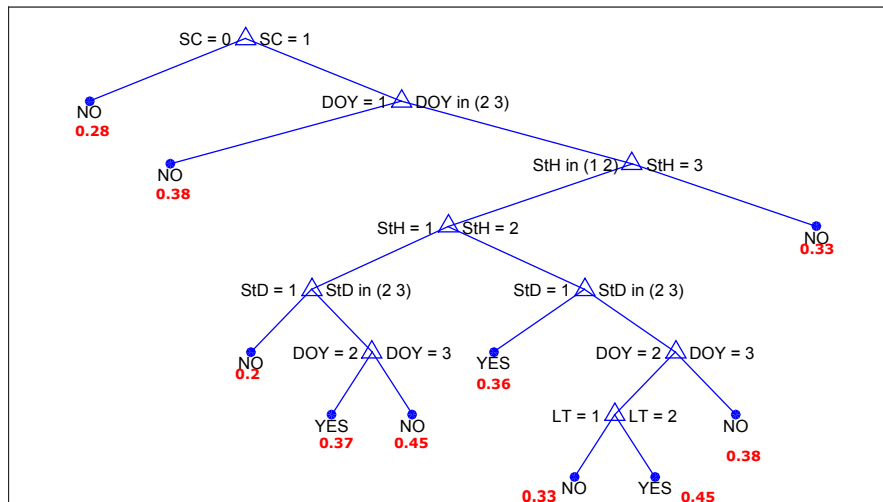


Fig. 4.9: Decision Tree for classifying end-of-storm response for 105 km altitude, upper-mid latitude bin. The class YES indicates recovery and NO indicates otherwise. The inhomogeneity associated with each branch is illustrated at the bottom of the branch in red.

One of the common features we can discern from these four decision trees illustrated in fig. 4.8 to fig. 4.11 is the presence of multiple predictors in each decision for majority of the tree decisions. The multiple predictors in a decision indicate the multi-faceted nature of predictor-response relationships. The second feature we notice from the trees illustrated in fig. 4.8 to fig. 4.11 is the large value of disorder (numbers in red) associated with each of the decision. The continuous presence of high amount of disorder as indicated by the values ranging from 0.2 to 0.4 (20% to 40%), imply a cause other than data outliers.

In order to investigate the decision tree findings from a statistical standpoint, we use a measure called resubstitution error. Resubstitution error is the collective measure of the entropy of all the decisions unearthed from a decision tree. In other words it is equivalent to the average of all the values in red for a decision tree in the decision tree illustrations presented earlier. We plot the resubstitution error for all altitude-latitude bins for each of the four storm response variables under investigation in fig. 4.12.

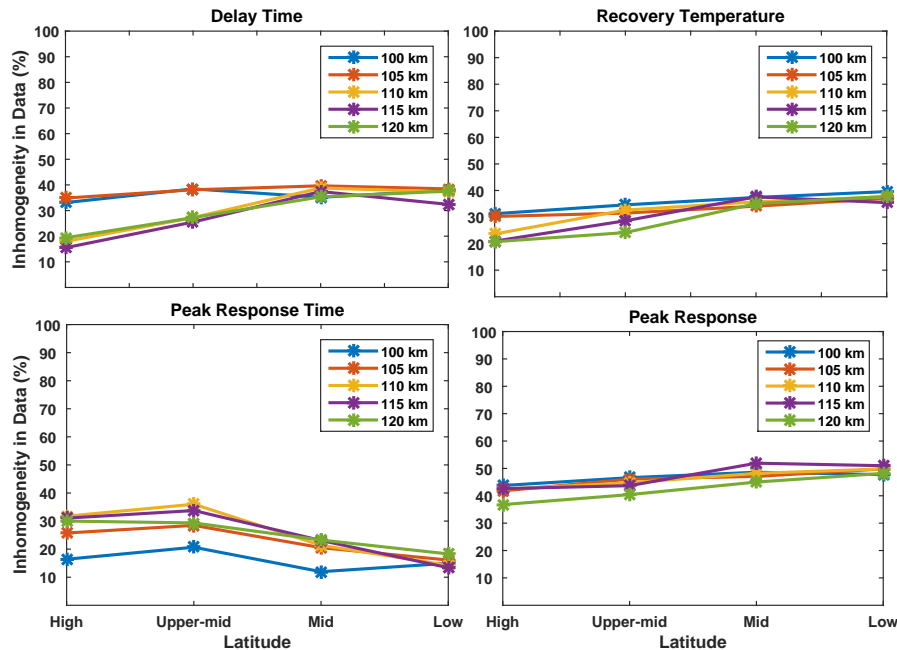


Fig. 4.12: Inhomogeneity of the decision tree response-predictor relationships across all latitude-altitude bins. Each of the four panels represent the four storm response variables.

As seen in fig. 4.12, a similar trend of higher inhomogeneity were found for most latitude-altitude bins. It was found that the patterns which did have lower inhomogeneity were associated with class imbalances. Class imbalances occur when overwhelming majority of the data belong to a single category of the response. In such a case, there is a dearth of combinatorial sub spaces of the minority category and thereby the algorithm is unable to resolve any patterns of the minority category subspace. For instance, the high-altitude-latitude bins correspond to *in situ* heating and thereby delay times are absent, barring a few exceptions. A lower resubstitution error is seen in this case as seen in the top panel of fig. 4.12 for the high latitude and altitude cases. This occurs due to the algorithm's failure to resolve any sub-spaces and form a tree decision. Such an imbalance results in the error to be the percentage of minority data (in the above example, the instances with delay) in the total data set. The class imbalance points towards the necessity of a larger data set to mine the pattern of the minority class of the response variable.

We believe that the larger inhomogeneity indicated by the large error values of 20% to 40% are a symptom of insufficient data or that the storm response predictors used here are not entirely reflective of all the factors influencing the storm response. Another possibility could be that the grouping of storm response predictors into categories as defined earlier, might not be indicative of the actual granularity of the storm response predictors in describing the storm response.

We check if the potential source of inhomogeneity exhibited by the decision trees is due to the improper categorization of the predictors, by using storm response predictors in their native numeric format to run the classification scheme. If the granularity of the predictor categories were insufficient to express the variation of storm response features, greater flexibility offered by a larger combinatorial space should improve the homogeneity of the decision tree. We plot the resubstitution error of such a tree in fig. 4.13.

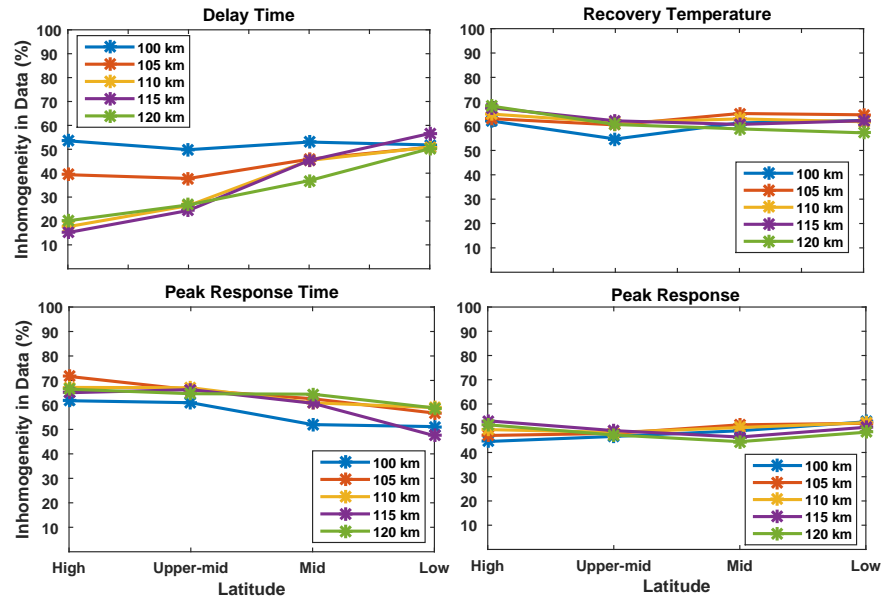


Fig. 4.13: Inhomogeneity of the decision tree response-predictor relationships using granular data.

As seen in fig. 4.13, there is no improvement in the resubstitution errors. In fact, some of the altitude-latitude bins exhibit larger inhomogeneity in their decision tree findings. These results point towards the insufficiency of data. Even if the granularity was the issue, the information contained within our sample set used in the statistical study is unable to unravel it.

The storm response predictors which are active in the realm of our investigation have been set-up as per the current knowledge of lower thermosphere storm time dynamics. The objective was never about reaffirming the importance or deducing the predictors, but deducing the combinatorial influence of the predictors. Hence as per our current thermospheric understanding, we conclude that missing predictors are unlikely to be the cause for the large resubstitution errors.

In addition to the sample size feature discussed above, another recurrent trend in our analysis was the presence of multiple predictors forming a pattern. This confirms the long speculated nature of storm response being a multifaceted phenomenon. The quantity resubstitution error plotted in fig. 4.12 can be used to demonstrate the same insight. If

the influence of predictors were disjoint, given that the predictor sample domain contains the population domain, we should have unearthed patterns with increased homogeneity or perhaps with no entropy. However, the lack of such a case point towards the need for always looking at the storm response problem from a multifaceted angle.

With these arguments, we conclude that the level of convolution of predictors and their role in causing a certain response feature is complex and cannot be unraveled using the current sample size. A follow-up in the future study with larger data set would be the next logical step in the effort to refine our understanding of the thermosphere response to storms. Given the multifaceted nature of the storm response, it is imperative that we have storm intervals spread across the domain of all storm predictors. This is further suggestive of using caution when using current hypothesis of storm response predictor - storm response relationships which have been built to test the influence of single or few predictors.

4.4 Importance of Quiet Time Variation in Storm Response Studies

We conduct an analysis of calculating the storm response variables without applying the quiet time variation model. By doing so, all the variations due to the separation of quiet and storm intervals and the variations arising from the asynoptic data, will be intertwined with the storm response and the ensuing storm response variable calculations. We plot the difference between the storm response using quiet time variation model and without using the model in fig. 4.14 and fig. 4.15. This difference is the illustration of errors we would see if the quiet time variations were not accounted-for, and the difference between the quiet and storm time were taken as-is to be the storm response. The storm response variables presented in fig. 4.14 and fig. 4.15 are derived from the storm response samples illustrated in fig. 4.2. The boxplot construction is similar to the percentile set up that was explained earlier for fig. 4.4 and fig. 4.5.

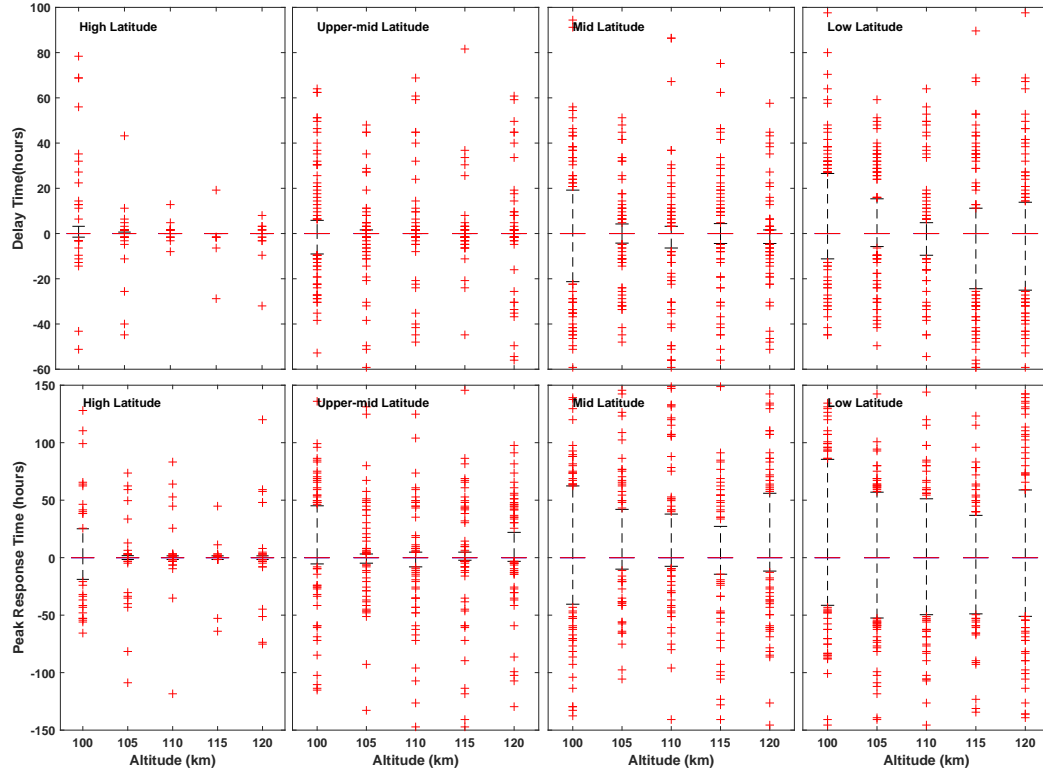


Fig. 4.14: Errors in times of storm response from ignoring quiet time variation. The top panels represent the error in delay time and the bottom panels represent the error in peak response time that was seen across various latitude-altitude bins.

The fig. 4.14 illustrates the spread of phase variations of the local time and seasonal harmonics, which are intertwined in the storm response due to absence of the quiet time variation model. The median phase component was less than or equal to one orbit for all the latitude-altitude bins. The collapsed boxes and whiskers indicate that 50% of the storm response data would have errors of longer than an orbit in the time response calculations. The magnitude errors are illustrated in fig. 4.15 which indicate median magnitude error being close to zero. The low altitude-latitude bins have the highest dispersion of the quiet time variations followed by the mid-latitude bins.

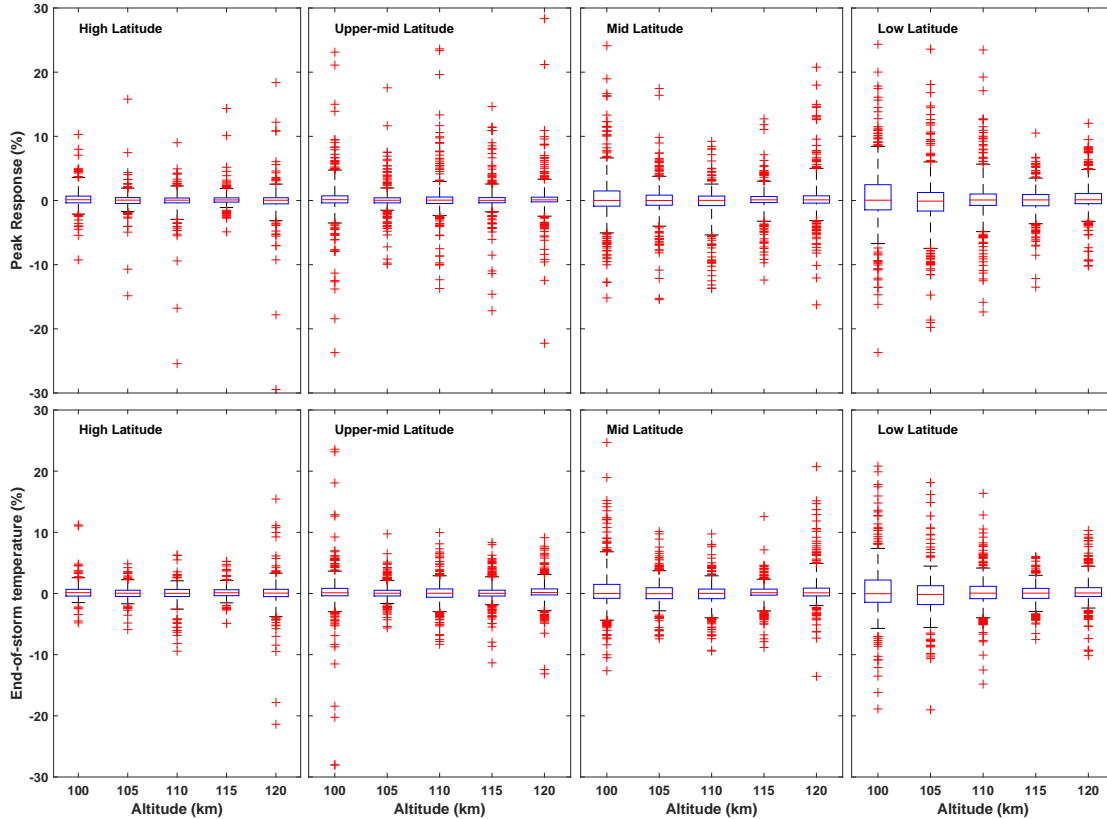


Fig. 4.15: Errors in magnitude of storm response from ignoring quiet time variation. The top panels represent the error in peak response and the bottom panels represent the error in end-of-storm response that was seen across various latitude-altitude bins.

In order to assess the importance of quiet time variations, these errors need to be put in the context of the observed values of the magnitudes and times of the storm response across all the bins. As seen in fig. 4.4, the high altitude-latitude bins have peak responses ranging from -20% to 120% , while the peak response of the low latitude-altitude bins is between -20% to 20% . Hence, even though the peak response errors at high latitude-altitude are comparable with the rest, the significance of errors is greatest at the low latitude-altitude bins since the error is comparable to the peak response computed at these bins. Using this argument and comparing time and magnitude responses from the above figures of this section with those of fig. 4.4 and fig. 4.5, it can be seen that the accuracy of the storm response at low latitude bins at 105 km and 100 km will suffer the most, if the quiet time variations are ignored.

4.5 Summary

This chapter presented the first ever statistical analysis of the lower thermosphere response to storms. Our sample set comprised storm intervals spread across the years from 2002 to 2010. Here below are some of the salient features from this analysis:

- The magnitude response was highest at the polar latitude bins with instances of increases up to 100% and more being observed. The rest of the bins exhibited up to 40% increase in temperature magnitudes with respect to their quiet time magnitudes.
- The delay times of majority of the polar bins at 110 km was 1.6 hours. The median was close to 5 to 8 hours for the rest of the latitude-altitude bins.
- The presence of large delay times for all latitude bins corresponding to the 100 km altitude bin hinted that the storm energy transport from higher altitudes was more important than *in situ* heating at these lower altitudes.
- The recovery of the thermosphere to quietude was not complete in the 24 hours after the end of storm for about 10% to 25% of the storm samples.

This chapter also presented the first ever multivariate study of storm response. A new technique of analysis using decision trees was formulated. The ensuing analysis highlighted the multifaceted nature of the storm response and emphasized on the necessity of using all the factors influencing the storm response such as local time, season, solar cycle and type of storm to be simultaneously considered while defining the storm response. The decision tree analysis indicated that the information dispensed by the decade long data is not sufficient to infer the complex nature of the predictor domain - response domain relationships, calling for a larger scale statistical study to be conducted in the future.

We also conducted a study to investigate the importance of considering quiet time variations in storm response computations. We found the importance of the quiet time variations to be highest at the low latitude bins where the quiet time contributions were comparable to the storm responses.

CHAPTER 5
COMPARISON OF LOWER THERMOSPHERIC STORM RESPONSE OF SABER,
NRLMSIS-00 AND TIEGCM TEMPERATURES

The models, TIEGCM [72] and NRLMSIS-00 [71], are state-of-art physics and empirical models of the thermosphere, whose representation of the upper-thermosphere energetics and dynamics, have been previously studied [73]. This includes the study of upper thermosphere energetics and dynamics during geomagnetic storms. However, their performance and replication of thermosphere behavior during geomagnetic storms at the lower altitudes of 100 - 120 km, has not been investigated so far. In this chapter, we investigate the TIEGCM and NRLMSIS-00 simulations of the lower thermosphere response to geomagnetic storms, in-comparison with the SABER temperature derived storm response.

5.1 Storm Intervals

The storm responses that were analyzed so far were processed using the quiet time variation model. This was done to remove the variations induced from asynoptic satellite sampling and from the quiet and storm interval separation. However the construction of the quiet time variation model is local to the SABER temperature data and therefore cannot be applied to the TIEGCM and NRLMSIS-00 models. Hence to conduct a comparison between the models and data, we search for storm intervals whose length and separation from a quiet interval correspond to a negligible local time precession of the TIMED orbit. This ensures we can conduct the storm response analysis without using the quiet time variation model. Although we could find a few storm intervals using this search criterion during the solar minima, we could not find any storm intervals during the solar maxima phase of the solar cycle. To facilitate analyzing a storm interval of higher intensity which is prevalent only during the solar maxima phase, we relax our definition of quiet interval by scanning for intervals which predominantly has Kp less than 3 but allowing a few hours of Kp index

being equal to 3.

Using this criterion, we choose two storms for this study, one that occurred during Oct 2008 and the other during Oct 2003. The Oct 2008 storm interval comprises the duration between 12:00 of UT October 11, 2008 and 06:00 UT of October 13, 2008. The 24 hour interval preceding 12:00 UT of October 10, 2008 is taken as the quiet interval. Since the local time precession of TIMED orbit is about 12 minutes a day, the local time precession of the TIMED orbit for the storm and quiet intervals is less than hour of local time for the Oct 2008 storm. The second storm we selected for this study corresponds to the duration of 02:00 UT October 28, 2003 to 17:00 UT November 4, 2003. The nearest quiet interval is the 24 hour duration following 18:00 UT of November 5, 2003. The quiet interval has 3 hours of Kp index of values 3 with the remainder of the quiet interval having Kp less than 3. For this storm, the local time precession of the TIMED orbit is about 0.4 - 1.5 hours of local time for the storm and quiet intervals. We illustrate the relative Dst indices of the storm interval which were defined as the variations with respect to the quiet interval Dst, in fig. 5.1.

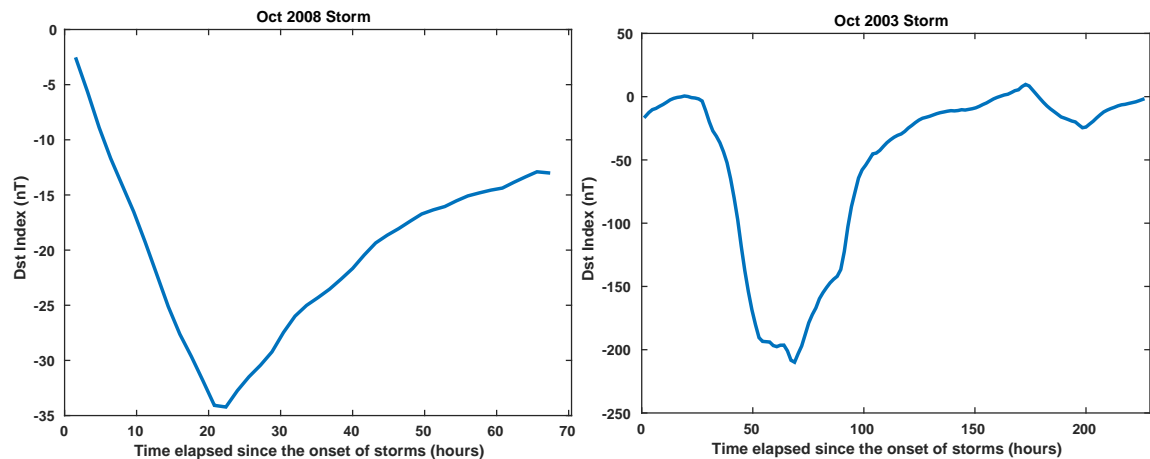


Fig. 5.1: Dst index values for the Oct 2008 (left box) and the Oct 2003 (right box) storm intervals. The value of the Dst indices illustrated in this figure are the relative Dst indices which are defined as the relative variation of the storm interval Dst values with reference to the quiet interval Dst index.

5.2 Storm Responses

The TIEGCM and NRLMSIS-00 data were run along the orbits of SABER measurements for both of the storm intervals and their respective quiet intervals. The data sets were aggregated in 20° latitude and 5 km altitude bins. We calculated the storm response T_{storm} as follows

$$T_{storm}(\Theta, z) = \frac{T_s(\Theta, z) - T_q(\Theta, z)}{T_q(\Theta, z)} * 100. \quad (5.1)$$

In equation (5.1), $T_s(\Theta, z)$ and $T_q(\Theta, z)$ are the zonal mean temperatures of the storm and quiet interval respectively at latitude Θ and altitude z .

We illustrate the models and the SABER data response to both the storms in fig. 5.2 and fig. 5.3. To illustrate the global storm response behavior at all altitudes in a concise manner which is suitable for data *vs.* model comparisons, we make use of the storm response variables that were defined in Chapter 3. The storm response variables for all latitude - altitude bins, for both the storms are presented in fig. 5.4 - fig. 5.13. In fig. 5.4 - fig. 5.13, the storm response predictors for the ascending pass are illustrated with thick bars and the descending pass with thin bars having red outlines. For the Oct 2008 storm, the ascending pass measurements correspond to nighttime measurements around 20:00 to 23:00 local times for -30° to 70° latitude, while the descending pass measurements correspond to the evening sector of 15:00 to 17:00 local times. Both ascending and descending pass measurements correspond to nighttime sector of 23:00 and 02:00 local time for the -50° latitude. For the Oct 2003 storm, the ascending pass measurements correspond to nighttime measurements around 02:00 to 03:00 local times for -30° to 70° latitude, while the descending pass measurements correspond to the evening sector of 17:00 to 18:00. Both ascending and descending pass measurements correspond to nighttime sector of 20:00 and 01:00 local times for the -50° latitude.

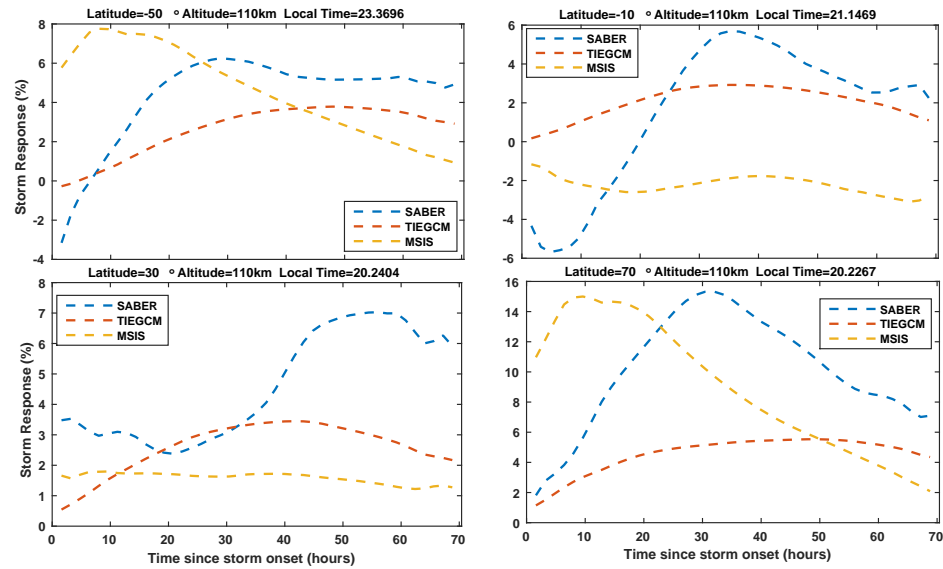


Fig. 5.2: Comparison of the SABER, NRLMSIS-00 and TIEGCM response to the Oct 2008 storm for selected latitude bins of 110 km altitude. The local time of the SABER orbit at the storm onset for each of the selected latitude is illustrated at the top of the plot.

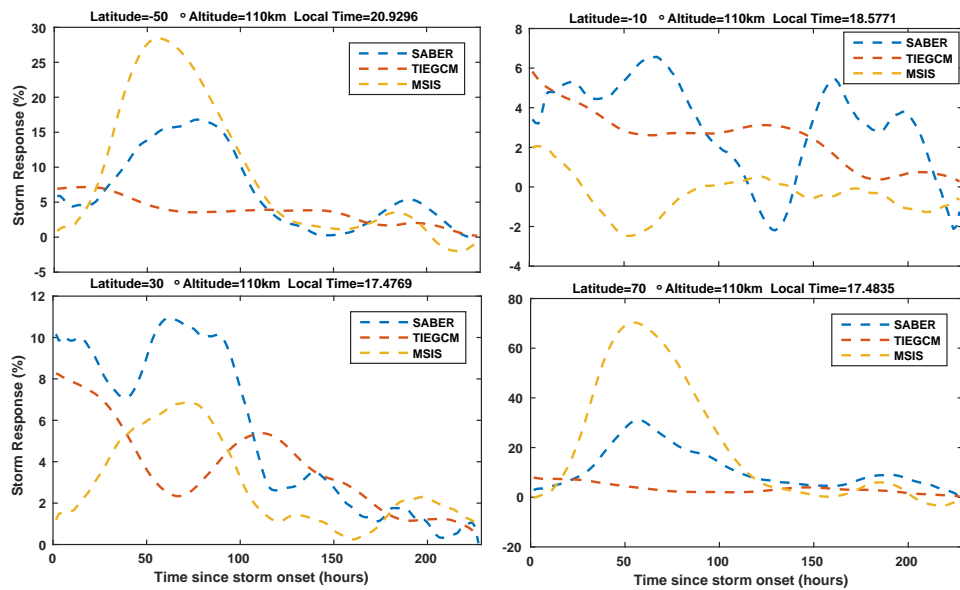


Fig. 5.3: Comparison of the SABER, NRLMSIS-00 and TIEGCM response to the Oct 2003 storm for selected latitude bins of 110 km altitude. The local time of the SABER orbit at the storm onset for each of the selected latitude is illustrated at the top of the plot.

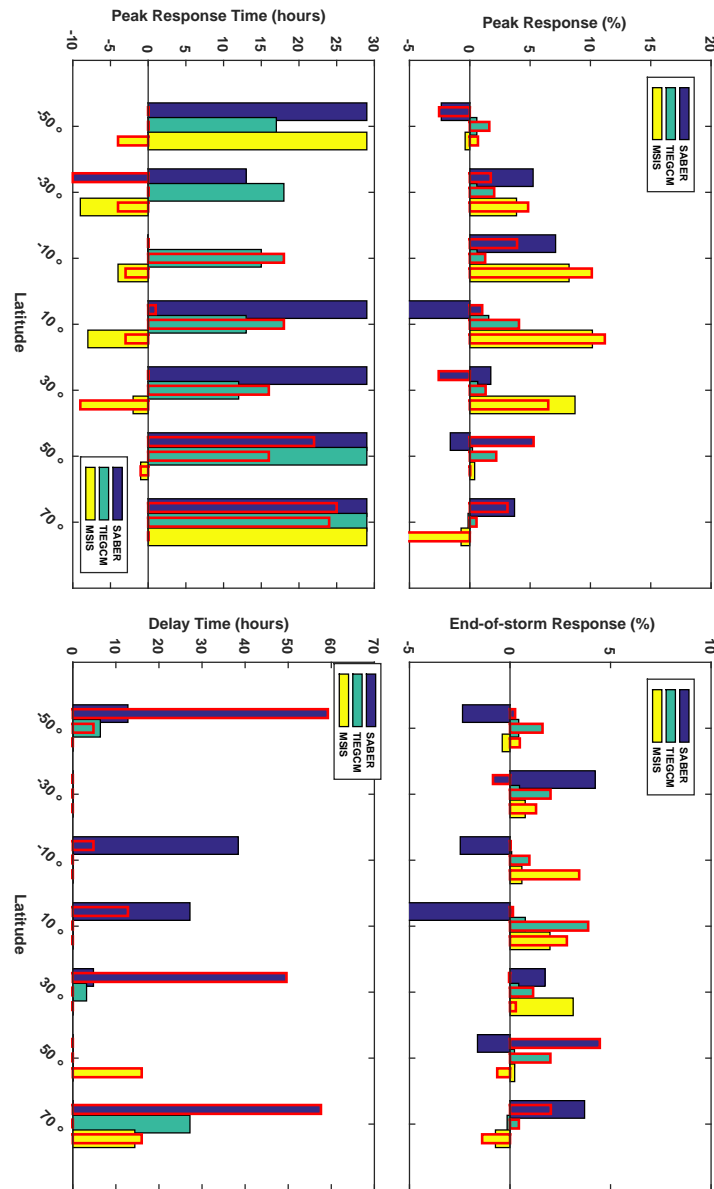


Fig. 5.4: Comparison of the Oct 2008 storm response variables computed using SABER, NRLMSIS-00 and TIEGCM for all latitudes of the 100 km altitude bin. In this figure, the thick bars represent the storm response variables deduced from the ascending pass measurements and the thin bars with red outline represent the storm response variables derived from the descending pass.

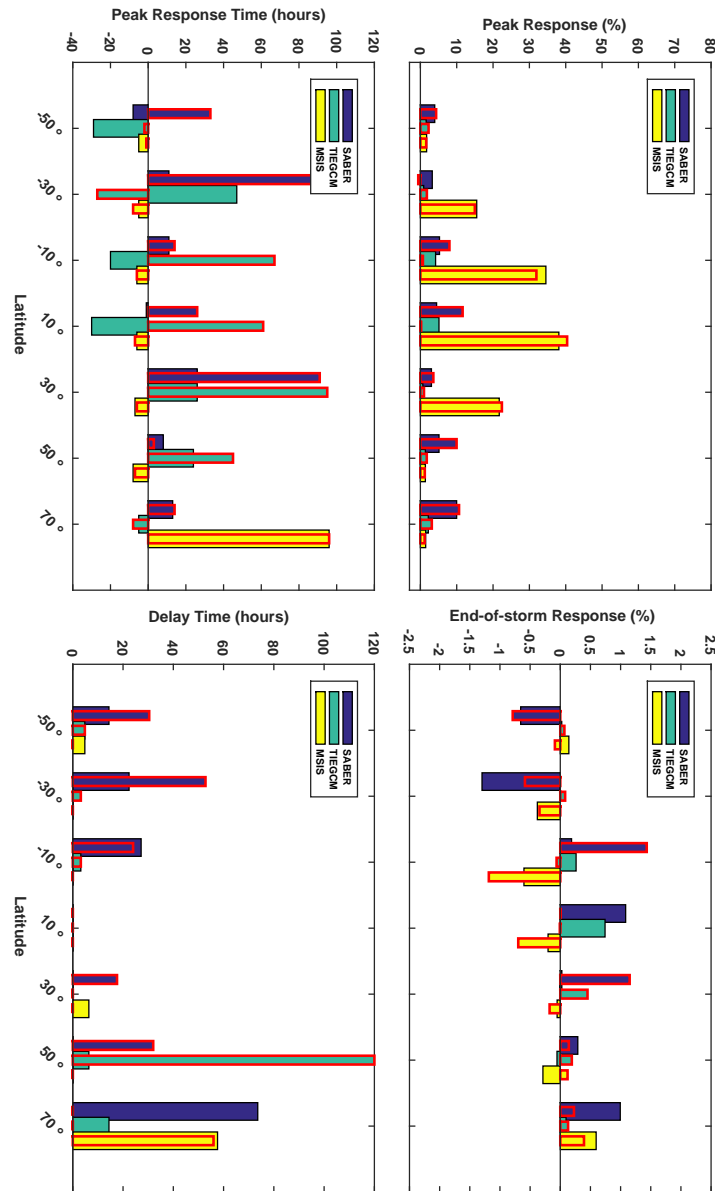


Fig. 5.5: Comparison of the Oct 2003 storm response variables computed using SABER, NRLMSIS-00 and TIEGCM for all latitudes of the 100 km altitude bin. In this figure, the thick bars represent the storm response variables deduced from the ascending pass measurements and the thin bars with red outline represent the storm response variables derived from the descending pass.

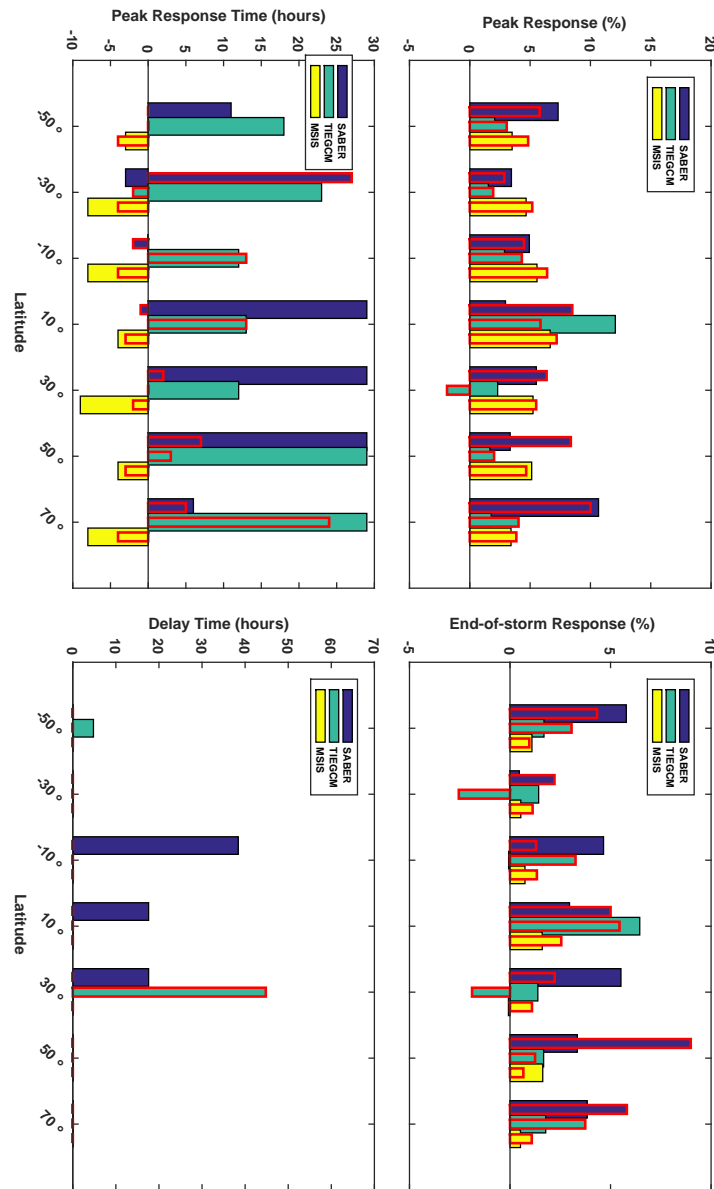


Fig. 5.6: Comparison of the Oct 2008 storm response variables computed using SABER, NRLMSIS-00 and TIEGCM for all latitudes of the 105 km altitude bin. In this figure, the thick bars represent the storm response variables deduced from the ascending pass measurements and the thin bars with red outline represent the storm response variables derived from the descending pass.

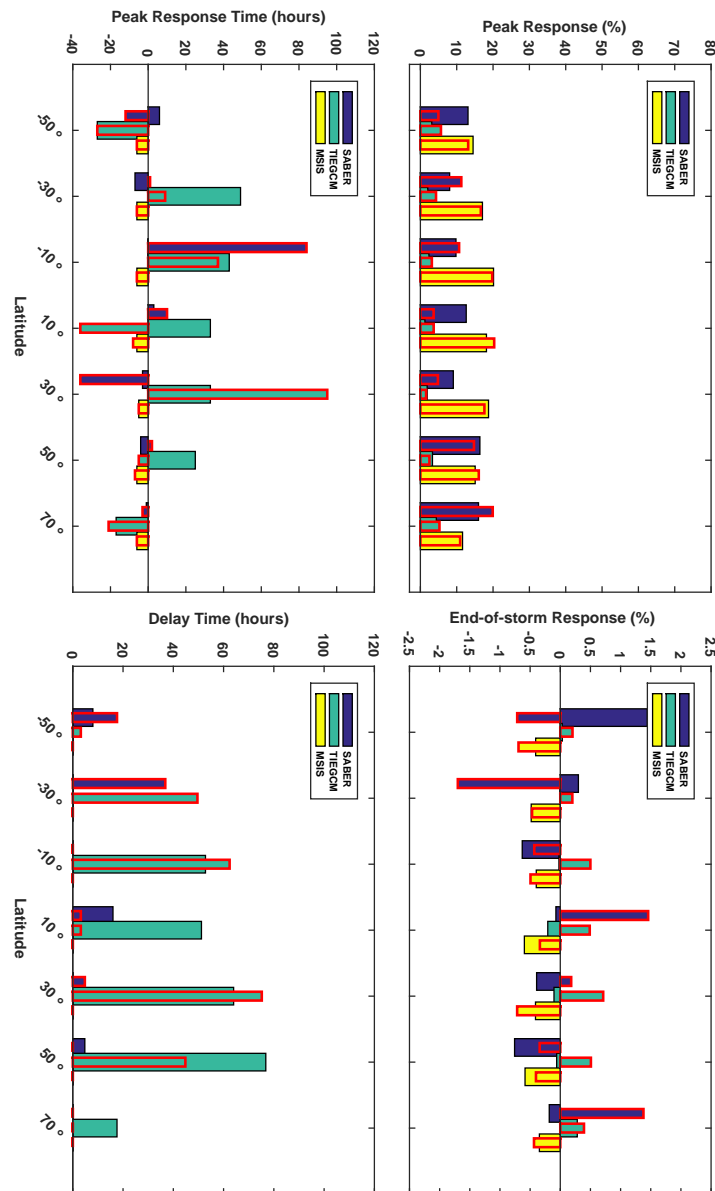


Fig. 5.7: Comparison of the Oct 2003 storm response variables computed using SABER, NRLMSIS-00 and TIEGCM for all latitudes of the 105 km altitude bin. In this figure, the thick bars represent the storm response variables deduced from the ascending pass measurements and the thin bars with red outline represent the storm response variables derived from the descending pass.

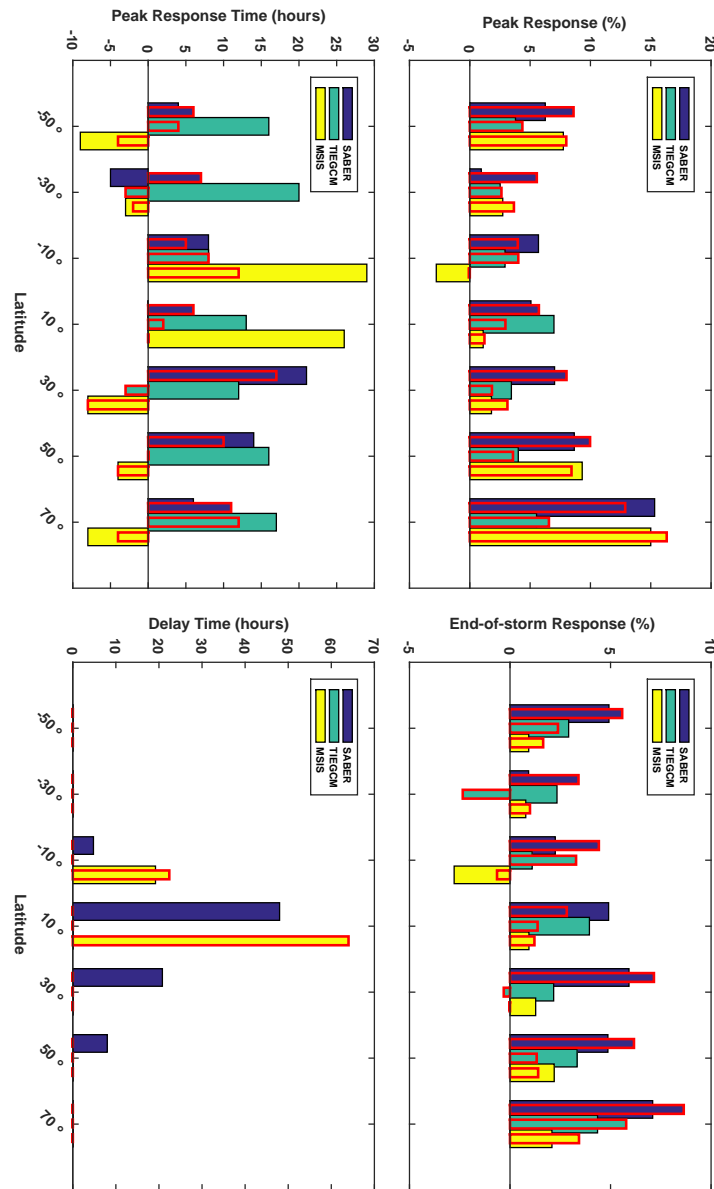


Fig. 5.8: Comparison of the Oct 2008 storm response variables computed using SABER, NRLMSIS-00 and TIEGCM for all latitudes of the 110 km altitude bin. In this figure, the thick bars represent the storm response variables deduced from the ascending pass measurements and the thin bars with red outline represent the storm response variables derived from the descending pass.

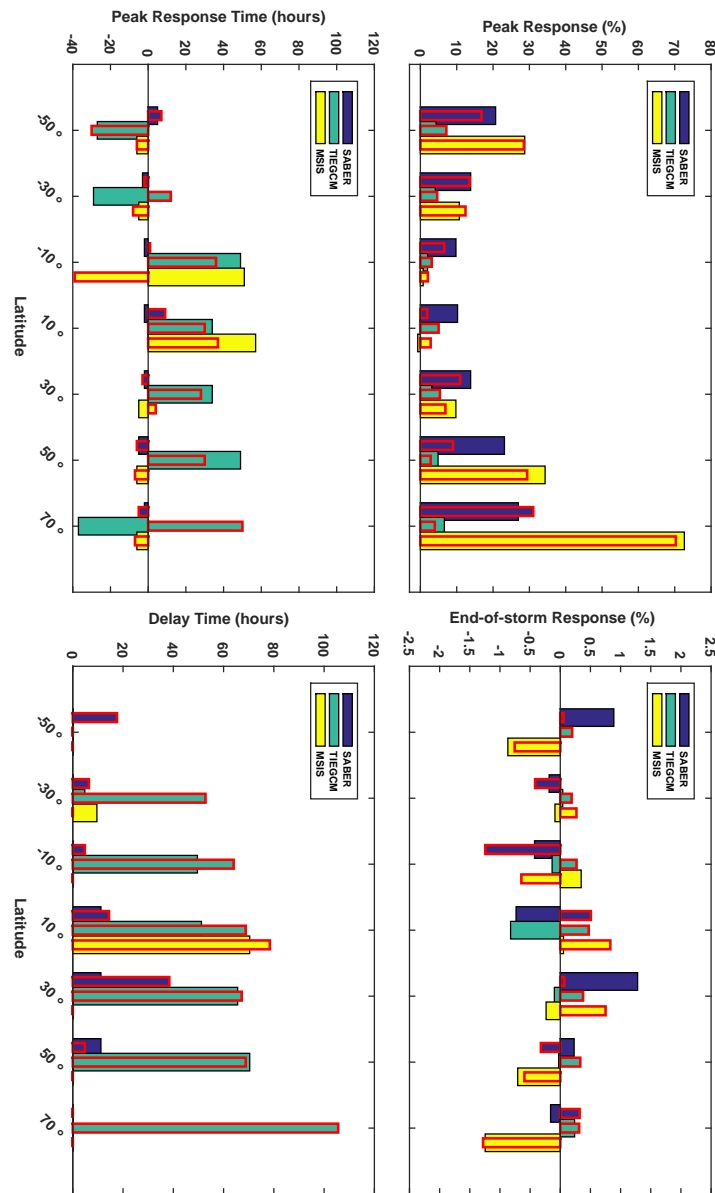


Fig. 5.9: Comparison of the Oct 2003 storm response variables computed using SABER, NRLMSIS-00 and TIEGCM for all latitudes of the 110 km altitude bin. In this figure, the thick bars represent the storm response variables deduced from the ascending pass measurements and the thin bars with red outline represent the storm response variables derived from the descending pass.

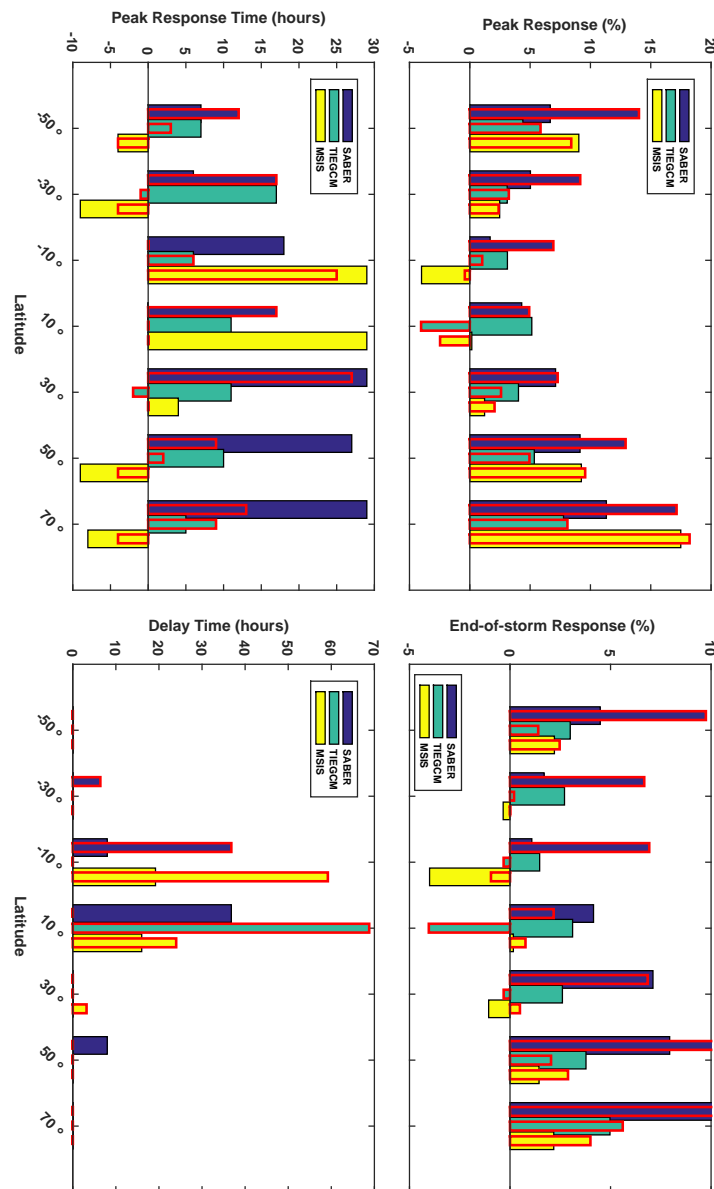


Fig. 5.10: Comparison of the Oct 2008 storm response variables computed using SABER, NRLMSIS-00 and TIEGCM for all latitudes of the 115 km altitude bin. In this figure, the thick bars represent the storm response variables deduced from the ascending pass measurements and the thin bars with red outline represent the storm response variables derived from the descending pass.

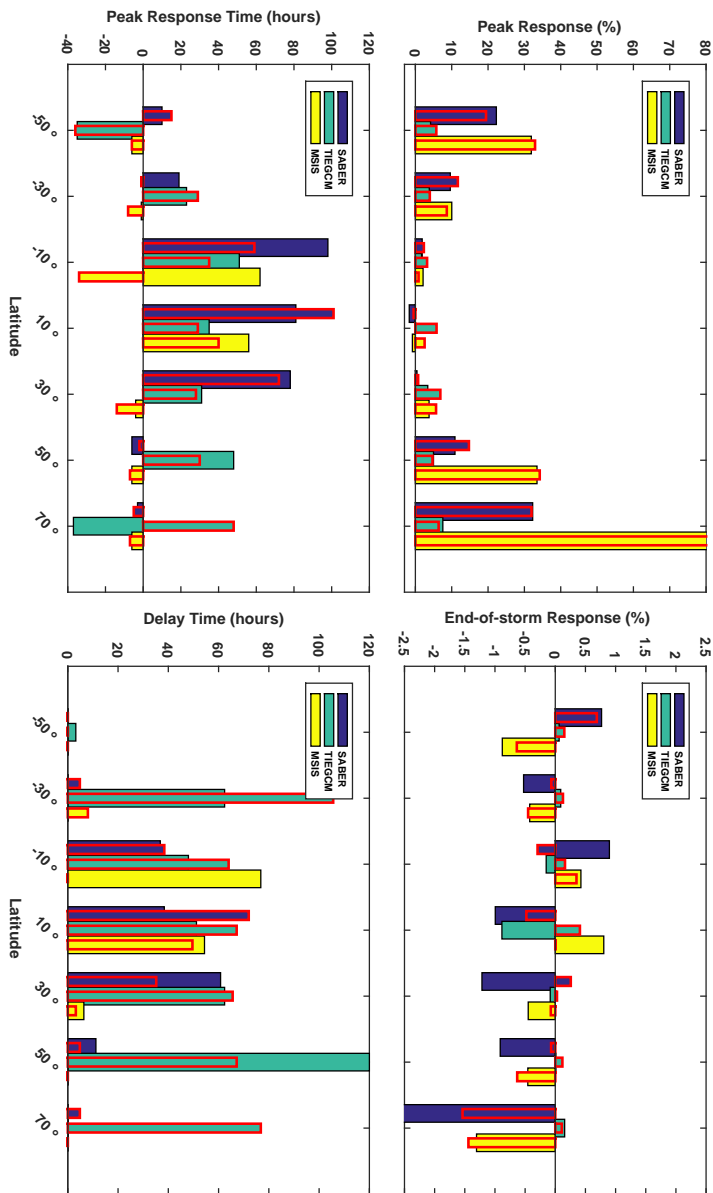


Fig. 5.11: Comparison of the Oct 2003 storm response variables computed using SABER, NRLMSIS-00 and TIEGCM for all latitudes of the 115 km altitude bin. In this figure, the thick bars represent the storm response variables deduced from the ascending pass measurements and the thin bars with red outline represent the storm response variables derived from the descending pass.

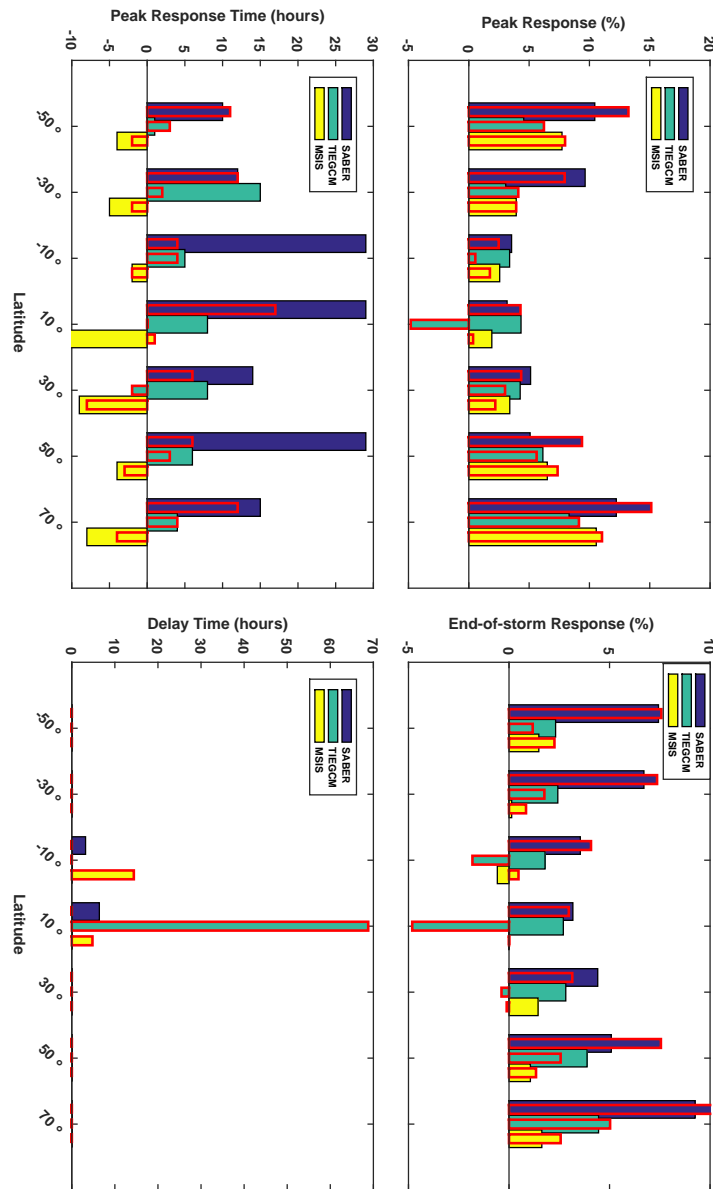


Fig. 5.12: Comparison of the Oct 2008 storm response variables computed using SABER, NRLMSIS-00 and TIEGCM for all latitudes of the 120 km altitude bin. In this figure, the thick bars represent the storm response variables deduced from the ascending pass measurements and the thin bars with red outline represent the storm response variables derived from the descending pass.

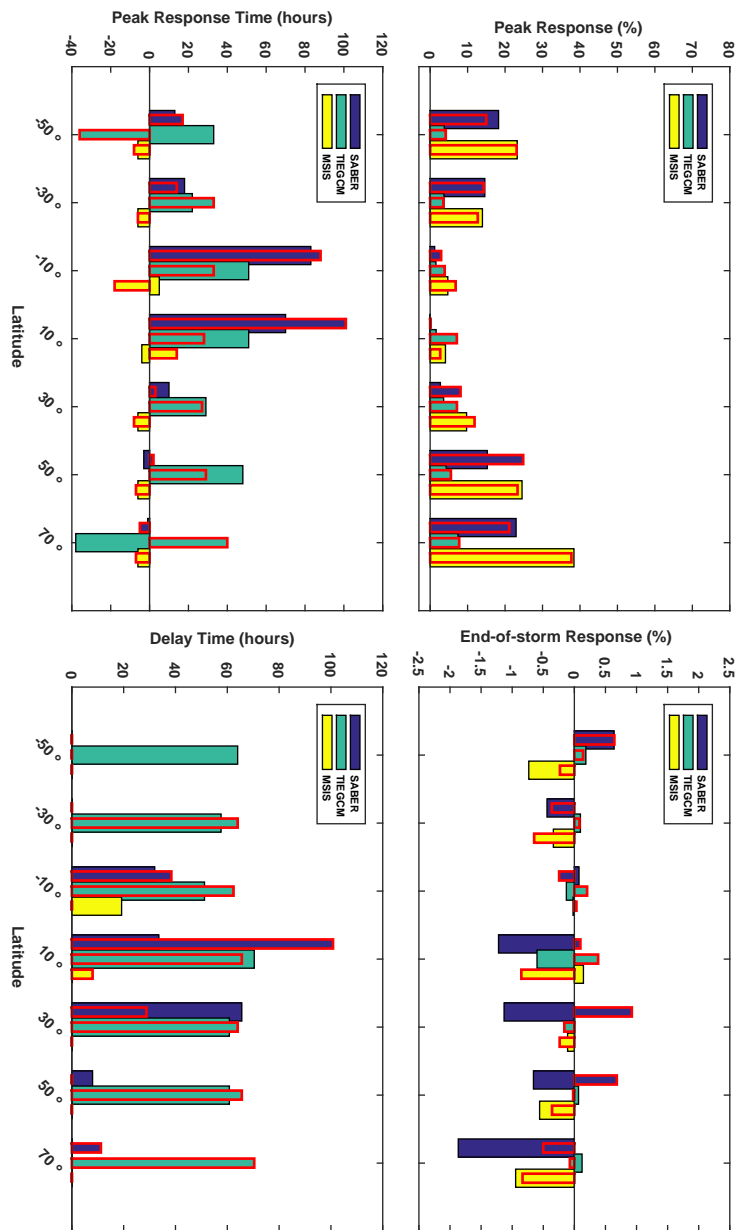


Fig. 5.13: Comparison of the Oct 2003 storm response variables computed using SABER, NRLMSIS-00 and TIEGCM for all latitudes of the 120 km altitude bin. In this figure, the thick bars represent the storm response variables deduced from the ascending pass measurements and the thin bars with red outline represent the storm response variables derived from the descending pass.

5.2.1 Discussion

As seen in fig. 5.4 - fig. 5.13, the SABER storm responses for both of the storms exhibit maximum peak response at polar latitude bins, at altitudes of 110 km and higher. The Oct 2003 storm has higher intensity than the Oct 2008 storm and the SABER peak response correspondingly exhibits a higher peak response for the Oct 2003 storm. The peak response times for both the storms indicate that the peak response trails behind the storm energy peak for most latitude-altitude bins. The delay times are largest for the case of 100 km altitude. For the Oct 2008 storm, the end-of-storm response indicates the recovery to be partial, however, for the Oct 2003 storm, the end-of-storm response is close to zero, hinting that the thermospheric recovery from the storm is possibly complete.

The NRLMSIS-00 storm responses are largely comparable in their peak responses to that of the SABER data, with the exception of polar latitudes for the Oct 2003 storm. The altitude distribution of the peak responses is reflective of the SABER temperature storm responses. The NRLMSIS-00 simulations systematically indicate immediate response at polar latitudes with delays seen for 100 km and equatorial bins. Similarly, the peak charging times for both the storms, mostly lead the storm energy peak and subsequently recover back to the quiet time values at the end of the storm interval. These systematic storm response differences seen in the comparisons between NRLMSIS-00 and SABER delay times and peak charging times, point towards the need of lower thermospheric storm time measurements to be assimilated into the NRLMSIS-00 model.

The TIEGCM model largely underestimates the response to both the storms. The largest differences between TIEGCM and SABER are seen at the poles, with largest differences seen for the Oct 2003 storm. The model does not have any systematic trends that can be discerned from its comparison with the data. We speculate the woefully low polar responses and the subsequent sub-polar responses, to be linked to the choice of the high latitude electrodynamics input into the model. We use Weimer model as the high latitude electrodynamics input into the TIEGCM runs. Use of data assimilation procedures like AMIE or AMPERE data would need to be used in a follow-up study to test if any

improvements in the magnitudes of storm response can be seen.

We investigate whether the difference between the ascending and descending pass responses that are made at two different local times, are reflective of our current understanding of the local time effects on the storm response. As mentioned earlier, the thick bars indicate nightside and the thin bars indicate dayside in fig. 5.4 - fig. 5.13, for both the storms, for the latitudes -30° to 70° . For -50° latitude, both ascending and descending pass measurements are nighttime, for both of the storms. As explained in Chapter 3, the local time influence has been linked to the Joule heating efficiency. It is believed that Joule heating efficiency is greater in the presence of decreased EUV radiation and hence nighttime is expected to exhibit higher storm induced changes [48] when compared to daytime. Hence, as per this, the peak response with thick bars should be higher than the red-outlined thin bar counterparts in fig. 5.4 - fig. 5.13 for the latitudes -30° to 70° . Our observations of the storm response indicate this is not always true and only limited altitude-latitude bins exhibit this trend. The daytime *vs.* nighttime differences are irregular for both of the models and the data, with no consistent trend emerging in their behavior. We believe this observation affirms the multi-faceted nature of the storm response that was discussed in Chapters 3 and 4, stressing the importance of other factors like storm intensity, the exact value of the local time, duration of the storm, etc., as adding complexity to the storm response.

We also investigate if the models and the data exhibit a similar trend in their peak response to the local time variation. It is observed that the difference between the ascending and descending pass storm responses for a latitude-altitude grid are not reflected in the corresponding responses obtained using the two models. NRLMSIS-00 model shows very little difference in its peak response for the two different local times. TIEGCM shows a marked difference for only the 10° latitude bin observation for the Oct 2003 storm and shows negligible difference for the rest of the observations.

We investigate the local time influence on the time taken for the storm energy to be transported to the sub-polar latitudes. Our current understanding is driven by the thought process that default equatorward transport from the poles during nighttime facilitates faster

storm energy transport. Hence when compared to daytime which have the quiet time flow from equator to pole, the nighttime sub-polar latitudes should see faster storm energy effects. However, we do not see an indication of this local time effect being responsible for storm energy transport in our observations across all of the latitudes and altitudes. The delay times are instead irregular in their latitude distribution. Also, the difference between the two delay times of the SABER storm response for the two different local times of a latitude-altitude bin, are not reflected in the models. A similar trend of disparity between the two models and the data for a given latitude-altitude grid in their local time influence on the storm response, is observed for all of the storm response variables. We therefore hypothesize that the local time effects on the storm response may not be sufficiently accounted-for, in both TIEGCM and NRLMSIS-00 models.

We also explore the seasonal influence since SABER makes measurements across both of the hemispheres. Note that for both of the storms here, the southern hemisphere is the summer hemisphere. The influence of seasons on times and magnitudes of the storm response are explained with similar undertones to that of local time [48]. Hence the summer hemisphere should exhibit faster sub-polar region transport and winter hemispheres should exhibit higher peak responses. We do not find any evidence for either of these two theories to be reflected in our observations. The difference in the observations between the two hemispheres for a given altitude bin are random. The difference between the southern and northern hemisphere for a given altitude bin of SABER storm response, is not sufficiently replicated in the two models. We hence conclude that both local time and seasonal influences are not sufficiently accounted-for in both TIEGCM and NRLMSIS-00 models. The storm response complexity as seen in the local time and seasonal differences, continues to support the multi-variate nature of the storm response predictors that was outlined in Chapter 4.

It is also worth noting that the Oct 2003 storm is longer than the Oct 2008 storm and has 2-8 days separation between the quiet interval and the storm interval. This separation corresponds to about 0.4 - 1.5 hours of local time progression of the SABER orbit. Hence any deficiencies in the modeling of local time-driven quiet time variations in TIEGCM and

NRLMSIS-00 could also be minimally contributing to the observed differences in the models *vs.* data comparisons of the Oct 2003 storm.

5.3 Summary

In this chapter, we compared SABER deduced thermosphere response of two storm intervals with that of physics and empirical models. The empirical model NRLMSIS-00, fared relatively better than the physics model TIEGCM. The difference between magnitude response of the data and models, as seen by peak response and end of storm response variables, was between 0 to 50%. The highest differences were seen between NRLMSIS-00 and SABER at high latitudes whereas TIEGCM consistently underestimated the global magnitude response when compared to SABER observations. The maximum time response differences between the data and models were found to be up to 70 hours for NRLMSIS-00 and 120 hours for TIEGCM.

CHAPTER 6

CONCLUSION

Geomagnetic storms energize the terrestrial atmosphere resulting in global energy redistribution. This energy mostly converges at altitudes of 100 to 150 km, which are then globally redistributed throughout the thermosphere. In this work, we presented the first ever study of the global thermospheric response to storms at lower altitudes of 100 to 120 km.

In this chapter, we present the key findings from our study and make recommendations for future studies.

6.1 Summary

6.1.1 Isolating Storm Response from SABER Temperature Measurements

The process of discerning the thermospheric response to storm energy involves isolating the characteristics of the thermosphere which differ from its base state. It is common practice to consider the orbit or the day before the storm as the base state and compute the storm response. In the case of a statistical study involving several storm intervals, such a scheme would suffer from the base state not being uniform for all the storm intervals. This is because the thermosphere during the pre-storm orbit/day will not necessarily be the same for every storm under consideration. This in-turn would cause the storm response characteristics deduced from such a study to have errors induced from the difference in the pre-conditioning of the thermosphere across the samples of the data set being used for the statistical study. Hence it is important that we choose a base state whose definition is uniform for all the storms. Therefore, in our study, we chose the thermosphere under quiet geomagnetic activity (K_p Index < 3) as the base state.

The storm interval and the above defined base state are not necessarily consecutive in

their occurrence, and when the measurement platform is asynoptic, geophysical variations from non-storm sources will convolve into the storm response deductions. These non-storm geophysical variations convolved with storm time measurements depend on the sampling scheme of the instrument and the satellite orbital characteristics.

In Chapter 2, we devised a scheme for accounting for these non-storm variations. The challenge in deriving such a scheme involved off-setting the bias and variance inherent to our decade long data set. The solution was the derivation of a piecewise continuous model which modeled all known sources of quiet time variation that could be potentially convolved into the storm response calculations of SABER temperatures. The model leveraged the almost constant beta angle of the TIMED satellite and the presence of large number of quiet days in the unusually quiet year 2009 in formulating what we refer to as the quiet time variation model.

6.1.2 Magnitude and Time Response of the Lower Thermosphere to Geomagnetic Storms

The quiet time variation model was applied to our statistical data set to derive the thermosphere temperature variations caused by the geomagnetic storm and the corresponding time scales for the storm induced changes to occur globally.

In Chapter 3, we investigated a single storm interval and illustrated the storm response morphology and discussed the typical features and their deviations. The case study served as an example storm from which storm response variables, variables which define the magnitude and time of storm response, were derived. These variables are essential to conduct the statistical study.

Since the satellite samples both the hemispheres with the exception of polar latitudes and also provides both dayside and nightside coverage, the case study was used to test some of the current hypothesis of local time and seasonal effects on storm response. The analysis highlighted the disparity in our current understanding and the observed thermospheric storm time dynamics, stemming from our limited knowledge of case studies and univariate analysis of storm response. The results of this case study highlighted some of the salient

features of storm response and also pointed towards the necessity of conducting multi-variate storm response studies using a statistical data set.

6.1.3 Statistical Study of Storm Response

Such a multi-variate storm response study and the statistical study was conducted in Chapter 4. Some of the findings from this study include:

- The magnitude of increase is highest at the polar regions of altitudes 110 km and above, with instances of temperature increase up to 100% were observed. The rest of the bins exhibited up to 40% increase in temperature with respect to the quiet time.
- The polar bins above 100 km mostly exhibited immediate response to storms with less than 25% of the sample set exhibiting larger delays. The delay time of the mid and low latitude bins vary from being 1.5 hours to a couple of days. The median was close to 5 to 8 hours for all sub-polar latitude-altitude bins.
- The delay times at 100 km were seen to be more than an orbit for all the latitude bins indicating energy transport from other latitudes as the major source of storm energy at all latitudes, including the polar bins.
- The recovery of the thermosphere to quietude was not complete in the 24 hours after the end-of storm for about 25% of our storm samples.

We conducted a multivariate study of storm response by simultaneously accounting for all the factors which influence the thermospheric storm response. We derived a decision tree algorithm set up to investigate the influence of local time, seasons, solar cycle, and type of storm as the various predictors responsible for the thermosphere's reaction to storm energy.

The study confirmed the speculation that the storm response is a multi-faceted phenomenon. The surprising find of the study was that the decade long data set is not sufficient to unravel the multivariate nature of storm response predictors. This highlights the nature of storm response being a combinations of variations whose modes vary widely in time and spatial scales.

6.1.4 Comparison of State-of-art Physics and Empirical Models

We compared the performance of NRLMSIS-00 and TIEGCM models in replicating the lower thermosphere storm response as observed using SABER data. The performance of the model and the data were compared for two storm intervals and it was seen that the empirical model had systematic differences in its behavior with respect to the SABER data. The model captured some of the features like altitude and latitude distribution of storm energy but failed to sufficiently capture the magnitudes and times of any of the storm induced changes. The TIEGCM model consistently under estimated the model, especially at the high latitudes. The physics model mostly failed to capture the storm response details and in-comparison the empirical model looked more promising.

The maximum difference between magnitude response of the data and models, as seen by peak response and end of storm response variables, was 50% for NRLMSIS-00 and 30% for TIEGCM. The highest differences were seen between NRLMSIS-00 and SABER temperatures at high latitudes whereas TIEGCM consistently underestimated the magnitude response when compared to SABER observations across all latitudes. The maximum time response differences between the data and models were found to be 70 hours for NRLMSIS-00 and 120 hours for TIEGCM.

6.2 Future Work

This work provided an insight into the lower thermosphere response to storms. In the pursuit of this, various inadequacies and questions to be explored in future, were brought to light. We discuss these below.

- The storm response morphology that was discussed in Chapter 3 shed light onto some of the transport mechanisms that could be attributed to the observed response. Even though, we cannot conclude the type of transport mechanism responsible for the observed storm response, the time scales of 1.6 hours for equatorward transport and non-monotonic arrangement of delay times for storm response transport to lower latitudes, warrant an investigation into the role of the competing transport mechanisms. Aug-

menting our storm response study with wind and composition measurements would shed light onto this.

- The large scale wave activity noticed in Chapter 3 storm response observations hinted that the thermospheric response to storm energy could have larger resonances of periods of a few days. Exploring the periodicity of these large scale resonances or waves would aid in improving our understanding of thermospheric dynamics.
- Our storm response study highlighted the need for refinement in our understanding the thermosphere recovery time. It is currently believed that in 24 hours of time after the storm energy ceases, one would expect the thermosphere to recover from storm energy. However, on observing the end of the storm responses, it was seen that there were instances of storm intervals hinting at incomplete recovery. Extending the end-of-storm response further and investigating what could be used as an upper limit for the lower thermospheric recovery, would be a worthwhile effort.
- One of the surprising findings of this work was the inability of the statistical study to completely describe the storm response predictors. Extending the trend of case studies into a statistical study of 145 storm intervals, seemed like a large enough sample set to capture the modes of thermosphere response to storms. However, the complex nature of spatial and temporal scales of storm response predictors convolving with one another, challenged this assumption. Extending this statistical study to an additional decade would be a good step forward in solving the multi-variate storm response problem. Given that the longest time scale of interest is a solar cycle, we would need to augment our current data set with both solar maxima and solar minima data to ensure class balance of the decision tree algorithm.
- Models, both empirical and physics-based, do not provide sufficient description of the lower thermosphere under the influence of storm energy. Since the empirical models are only as good as the data that is fed into them, the addition of the findings from the SABER lower thermosphere study, could prove to be a useful metric for empirical

model refinement. Exploring the electric field models' role in improving the physics models would be yet another road forward.

In conclusion, understanding the thermospheric energetics and dynamics to provide closure to the outstanding questions, is contingent on obtaining additional data and measurements. A comprehensive study of all state variables of the lower thermosphere which can be obtained from the various instruments of the TIMED satellite would be a potential method for carrying out such an endeavor. Since TIMED is currently operational, extending our data set to include the end of the current solar cycle would be an excellent path forward in advancing our understanding of the lower thermospheric response to geomagnetic storms.

REFERENCES

- [1] C. L. Schrijver and G. L. Siscoe, *Heliophysics I: Plasma Physics of the Local Cosmos*. Cambridge University Press, 2009.
- [2] K. J. H. Phillips, *Guide to the Sun*. Cambridge University Press, 1995.
- [3] C. L. Schrijver and G. L. Siscoe, *Heliophysics II: Evolving Solar Activity and the Climates of Space and Earth*. Cambridge University Press, 2010.
- [4] C. T. Russell, "Solar wind and interplanetary magnetic field: A tutorial," *Space Weather*, pp. 73–89, 2001.
- [5] C. L. Schrijver and G. L. Siscoe, *Heliophysics III: Space Storms and Radiation: Causes and Effects*. Cambridge University Press, 2010.
- [6] D. H. Hathaway, "The Solar Cycle," *Living Reviews in Solar Physics*, no. 1, 2010.
- [7] C. T. Russell and J. G. Luhmann, "Solar-Terrestrial Interactions," *Encyclopedia of Earth Science*, vol. 4, 1992.
- [8] T. F. Tascione, *Introduction to the space environment*. Orbit: Foundation Series, 1988.
- [9] C. T. Russell, "The Solar Wind Interaction with the Magnetosphere: A Tutorial," *IEEE Transactions on Plasma Science*, vol. 28, no. 6, Dec. 2000.
- [10] R. Schwenn, "Space weather: The solar perspective," *Living Reviews in Solar Physics*, vol. 3, no. 2, 2006.
- [11] T. Pulkkinen, *Living Reviews in Solar Physics*.
- [12] N. Gopalaswamy, "Coronal mass ejections and space weather," *Climate and Weather of the Sun-Earth System (CAWSES): Selected Papers from the 2007 Kyoto Symposium*, 2009.
- [13] T. I. Gombosi, *Physics of the space environment*. Cambridge University Press, 1998.
- [14] J. E. Borovsky and M. H. Denton, "Differences between cme-driven storms and cir-driven storms," *Journal of Geophysical Research: Space Physics*, vol. 111, no. A7, 2006, a07S08.
- [15] P.-N. Mayaud, "Derivation, meaning, and use of geomagnetic indices," *Washington DC American Geophysical Union Geophysical Monograph Series*, vol. 22, p. 607, 1980.
- [16] G. Rostoker, "Geomagnetic indices," *Reviews of Geophysics*, vol. 10, no. 4, pp. 935–950, 1972.

- [17] M. H. Rees, *Physics and Chemistry of the Upper Atmosphere*. Cambridge University Press, 1989.
- [18] R. Schunk and A. Nagy, *Ionospheres*, 2nd ed. Cambridge University Press, 2009.
- [19] R. P. Wayne, *Chemistry of the Atmosphere*. Oxford University Press, 2000.
- [20] R. M. Johnson, T. L. Killeen, and R. G. Roble. American Geophysical Union, 1995.
- [21] T. L. Killeen, A. G. Burns, I. Azeem, S. Cochran, and R. G. Roble, “A theoretical analysis of the energy budget in the lower thermosphere,” *Journal of Atmospheric and Solar-Terrestrial Physics*, vol. 59, no. 2, pp. 675–689, 1997.
- [22] J. M. Forbes, “Dynamics of the thermosphere,” *Journal of the Meteorological Society of Japan. Ser. II*, vol. 85B, pp. 193–213, 2007.
- [23] R. G. Roble, “Dynamics of the earth’s thermosphere,” *Reviews of Geophysics*, vol. 21, no. 2, pp. 217–233, 1983.
- [24] A. E. Hedin and H. G. Mayr, “Solar euv variations in the thermosphere,” *Journal of geophysical Research*, vol. 92, pp. 869–875, 1987.
- [25] G. W. Prölls and M. Roemer, “Some properties of the polar energy source and of the associated atmospheric perturbations.”
- [26] D. Knipp, W. Tobiska, and B. Emery, “Direct and indirect thermospheric heating sources for solar cycles 21?23,” *Solar Physics*, vol. 224, no. 1-2, pp. 495–505, 2004.
- [27] J. P. Thayer and J. Semeter, “The convergence of magnetospheric energy flux in the polar atmosphere,” *Journal of Atmospheric and Solar-Terrestrial Physics.*, vol. 66, no. 10, pp. 807–824, 2004.
- [28] T. J. Fuller-Rowell and M. V. Codrescu, “Response of the thermosphere and ionosphere to geomagnetic storm,” *Journal of Geophysical Research*, vol. 99, no. A3, pp. 3393–3914, 1994.
- [29] L. G. Jacchia, “Corpuscular radiation and the acceleration of artificial satellites,” 1959.
- [30] G. W. Prölls, “Density perturbations in the upper atmosphere caused by the dissipation of solar wind energy,” *Surveys in Geophysics*, vol. 32, no. 2, pp. 101–195, 2011.
- [31] J. Emmert, “Thermospheric mass density: A review,” *Advances in Space Research*, vol. 56, no. 5, pp. 773–824, 2015.
- [32] J. M. Forbes, R. Gonzalez, F. A. Marcos, D. Revelle, and H. Parish, “Magnetic storm response of lower thermosphere density,” *Journal of Geophysical Research: Space Physics*, vol. 101, no. A2, pp. 2313–2319, 1996.

- [33] E. K. Sutton, J. M. Forbes, and D. J. Knipp, "Rapid response of the thermosphere to variations in joule heating," *Journal of Geophysical Research: Space Physics*, vol. 114, no. A4, 2009.
- [34] J. M. Forbes, G. Lu, S. Bruinsma, S. Nerem, and X. Zhang, "Thermosphere density variations due to the 1524 april 2002 solar events from champ/star accelerometer measurements," *Journal of Geophysical Research: Space Physics*, vol. 110, no. A12, 2005, a12S27.
- [35] J. Lei, J. P. Thayer, G. Lu, A. G. Burns, W. Wang, E. K. Sutton, and B. A. Emery, "Rapid recovery of thermosphere density during the october 2003 geomagnetic storms," *Journal of Geophysical Research: Space Physics*, vol. 116, no. A3, 2011, a03306.
- [36] S. Bruinsma, J. M. Forbes, R. S. Nerem, and X. Zhang, "Thermosphere density response to the 2021 november 2003 solar and geomagnetic storm from champ and grace accelerometer data," *Journal of Geophysical Research: Space Physics*, vol. 111, no. A6, 2006, a06303.
- [37] C. Barth, "Joule heating and nitric oxide in the thermosphere,1," *Journal of Geophysical Research: Space Physics*, vol. 114, no. A5, 2009.
- [38] C. Barth, "Joule heating and nitric oxide in the thermosphere,2," *Journal of Geophysical Research: Space Physics*, vol. 115, no. A10, 2010.
- [39] G. Earle, R. Davidson, R. Heelis, W. Coley, D. Weimer, J. Makela, D. Fisher, A. Gerard, and J. Meriwether, "Low latitude thermospheric responses to magnetic storms," *Journal of Geophysical Research: Space Physics*, vol. 118, no. 6, pp. 3866–3876, 2013.
- [40] A. Burns, W. Wang, S. Solomon, and L. Qian, "Energetics and composition in the thermosphere," *Modeling the Ionosphere-Thermosphere System, AGU Geophys. Monogr. Ser.*, 2014.
- [41] Y. Deng, T. J. Fuller-Rowell, R. A. Akmaev, and A. J. Ridley, "Impact of the altitudinal joule heating distribution on the thermosphere," *Journal of Geophysical Research: Space Physics*, vol. 116, no. A5, 2011.
- [42] Y. Huang, A. D. Richmond, Y. Deng, and R. Roble, "Height distribution of joule heating and its influence on the thermosphere," *Journal of Geophysical Research: Space Physics*, vol. 117, no. A8, 2012.
- [43] J. Lei, J. P. Thayer, A. G. Burns, G. Lu, and Y. Deng, "Wind and temperature effects on thermosphere mass density response to the november 2004 geomagnetic storm," *Journal of Geophysical Research: Space Physics*, vol. 115, no. A5, 2010.
- [44] A. Aksnes, R. Eastes, S. Budzien, and K. Dymond, "Dependence of neutral temperatures in the lower thermosphere on geomagnetic activity," *Journal of Geophysical Research: Space Physics*, vol. 112, no. A6, 2007, a06302.

- [45] L. C. Chang, J. P. Thayer, J. Lei, and S. E. Palo, "Isolation of the global mlt thermal response to recurrent geomagnetic activity," *Geophysical Research Letters*, vol. 36, no. 15, 2009.
- [46] R. McGranaghan, D. J. Knipp, R. L. McPherron, and L. A. Hunt, "Impact of equinoctial high-speed stream structures on thermospheric responses," *Space Weather*, vol. 12, no. 4, pp. 277–297, 2014.
- [47] G. Lu, M. Mlynczak, L. Hunt, T. Woods, and R. Roble, "On the relationship of joule heating and nitric oxide radiative cooling in the thermosphere," *Journal of Geophysical Research: Space Physics (1978–2012)*, vol. 115, no. A5, 2010.
- [48] A. Burns, T. Killeen, W. Wang, and R. Roble, "The solar-cycle-dependent response of the thermosphere to geomagnetic storms," *Journal of atmospheric and solar-terrestrial physics*, vol. 66, no. 1, pp. 1–14, 2004.
- [49] H. Liu and H. Lühr, "Strong disturbance of the upper thermospheric density due to magnetic storms: Champ observations," *Journal of Geophysical Research: Space Physics*, vol. 110, no. A9, 2005.
- [50] G.-m. Chen, J. Xu, W. Wang, A. Burns, *et al.*, "A comparison of the effects of cir-and cme-induced geomagnetic activity on thermospheric densities and spacecraft orbits: Statistical studies," *Journal of Geophysical Research: Space Physics*, vol. 119, no. 9, pp. 7928–7939, 2014.
- [51] G. Jiang, W. Wang, J. Xu, J. Yue, A. G. Burns, J. Lei, M. G. Mlynczak, and J. M. Russell, "Responses of the lower thermospheric temperature to the 9day and 13.5day oscillations of recurrent geomagnetic activity," *Journal of Geophysical Research: Space Physics*, vol. 119, no. 6, pp. 4841–4859, 2014, 2013JA019406.
- [52] C. Lathuillre, M. Menvielle, A. Marchaudon, and S. Bruinsma, "A statistical study of the observed and modeled global thermosphere response to magnetic activity at middle and low latitudes," *Journal of Geophysical Research: Space Physics*, vol. 113, no. A7, 2008, a07311.
- [53] J. Kennewell, B.-N. Vo, *et al.*, "An overview of space situational awareness," in *Information Fusion (FUSION), 2013 16th International Conference on*, pp. 1029–1036. IEEE, 2013.
- [54] D. J. Kessler, N. L. Johnson, J. Liou, and M. Matney, "The kessler syndrome: implications to future space operations," *Advances in the Astronautical Sciences*, vol. 137, no. 8, p. 2010, 2010.
- [55] D. A. Vallado and D. Finkleman, "A critical assessment of satellite drag and atmospheric density modeling," in *AIAA/AAS astrodynamics specialist conference and exhibit*, pp. 18–21, 2008.
- [56] D. N. Baker, "How to cope with space weather," *Science*, vol. 297, no. 5586, p. 1486, 2002.

- [57] J.-H. Yee, G. E. Cameron, and D. Y. Kusnierkiewicz, "Overview of timed," pp. 244–254, 1999.
- [58] J.-H. Yee, "Timed mission science overview," *John Hopkins Applied Technical Digest*, vol. 24, no. 2, pp. 244–254, 2003.
- [59] <http://www.nasa.gov/>.
- [60] R. Niciejewski, Q. Wu, W. Skinner, D. Gell, M. Cooper, A. Marshall, T. Killeen, S. Solomon, and D. Ortland, "Timed doppler interferometer on the thermosphere ionosphere mesosphere energetics and dynamics satellite: data product overview," *Journal of Geophysical Research: Space Physics (1978–2012)*, vol. 111, no. A11, 2006.
- [61] C. J. Mertens, M. G. Mlynczak, M. Lopez-Puertas, P. P. Wintersteiner, R. Picard, J. R. Winick, L. L. Gordley, and J. M. Russell III, "Retrieval of mesospheric and lower thermospheric kinetic temperature from measurements of," *Geophysical Research Letters*, vol. 28, no. 7, pp. 1391–1394, 2001.
- [62] M. Garca-Comas, M. Lopez-Puertas, B. T. Marshall, P. P. Wintersteiner, B. Funke, D. Bermejo-Pantalen, C. J. Mertens, E. E. Remsberg, L. L. Gordley, M. G. Mlynczak, and J. M. Russell, "Errors in sounding of the atmosphere using broadband emission radiometry (saber) kinetic temperature caused by non-local-thermodynamic-equilibrium model parameters," *Journal of Geophysical Research: Atmospheres*, vol. 113, no. D24, 2008.
- [63] A. B. Christensen, R. L. Bishop, S. A. Budzien, J. H. Hecht, M. G. Mlynczak, J. M. Russell, A. W. Stephan, and R. W. Walterscheid, "Altitude profiles of lower thermospheric temperature from raids/nirs and timed/saber remote sensing experiments," *Journal of Geophysical Research: Space Physics*, vol. 118, no. 6.
- [64] X. Zhang, J. M. Forbes, M. E. Hagan, J. M. Russell, S. E. Palo, C. J. Mertens, and M. G. Mlynczak, "Monthly tidal temperatures 20120 km from timed/saber," *Journal of Geophysical Research: Space Physics*, vol. 111, no. A10, pp. 2156–2202.
- [65] L. C. Chang, J. P. Thayer, J. Lei, and S. E. Palo, "Isolation of the global mlt thermal response to recurrent geomagnetic activity," *Geophysical Research Letters*, vol. 36, no. 15, 2009.
- [66] J. Xu, A. Smith, W. Wang, G. Jiang, W. Yuan, H. Gao, J. Yue, B. Funke, M. López-Puertas, and J. M. Russell, "An observational and theoretical study of the longitudinal variation in neutral temperature induced by aurora heating in the lower thermosphere," *Journal of Geophysical Research: Space Physics*, vol. 118, no. 11, pp. 7410–7425, 2013.
- [67] G. Jiang, W. Wang, J. Xu, J. Yue, A. G. Burns, J. Lei, M. G. Mlynczak, and J. M. Russell, "Responses of the lower thermospheric temperature to the 9 day and 13.5 day oscillations of recurrent geomagnetic activity," *Journal of Geophysical Research: Space Physics*, vol. 119, no. 6, pp. 4841–4859, 2014.
- [68] <http://saber.gats-inc.com/>.

- [69] W. H. Campbell, *Introduction to geomagnetic fields*. Cambridge University Press, 2003.
- [70] <http://wdc.kugi.kyoto-u.ac.jp/index.html>.
- [71] J. Picone, A. Hedin, D. P. Drob, and A. Aikin, “Nrlmsise-00 empirical model of the atmosphere: Statistical comparisons and scientific issues,” *Journal of Geophysical Research: Space Physics (1978–2012)*, vol. 107, no. A12, pp. SIA–15, 2002.
- [72] R. E. Dickinson, E. Ridley, and R. Roble, “Thermospheric general circulation with coupled dynamics and composition,” *Journal of the atmospheric sciences*, vol. 41, no. 2, pp. 205–219, 1984.
- [73] J. Shim, M. Kuznetsova, L. Rastätter, D. Bilitza, M. Butala, M. Codrescu, B. Emery, B. Foster, T. Fuller-Rowell, J. Huba, *et al.*, “Cedar electrodynamics thermosphere ionosphere (eti) challenge for systematic assessment of ionosphere/thermosphere models: Electron density, neutral density, nmf2, and hmf2 using space based observations,” *Space Weather*, vol. 10, no. 10, 2012.
- [74] <http://ccmc.gsfc.nasa.gov/>.
- [75] J. Lei, J. P. Thayer, W. Wang, and R. L. McPherron, “Impact of cir storms on thermosphere density variability during the solar minimum of 2008,” *Solar Physics*, vol. 274, no. 1-2, pp. 427–437, 2011.
- [76] J. S. Nisbet, C. Stehle, and E. Bleuler, “Initial tests of an index based on al values for modeling magnetic storm related perturbations of the thermosphere,” *Journal of Geophysical Research: Space Physics (1978–2012)*, vol. 88, no. A3, pp. 2175–2180, 1983.
- [77] G. W. Prolls and M. Roemer, “Thermosphere storms,” *Advances in space research*, vol. 7, no. 10, pp. 223–235, 1987.
- [78] G. Prölss, M. Roemer, and J. Slowey, “Dissipation of solar wind energy in the earth’s upper atmosphere: The geomagnetic activity effect,” *Advances in space research*, vol. 8, no. 5, pp. 215–261, 1988.
- [79] S. Maeda, T. Fuller-Rowell, and D. Evans, “Heat budget of the thermosphere and temperature variations during the recovery phase of a geomagnetic storm,” *Journal of Geophysical Research: Space Physics (1978–2012)*, vol. 97, no. A10, pp. 14 947–14 957, 1992.
- [80] G. R. Wilson, D. R. Weimer, J. O. Wise, and F. A. Marcos, “Response of the thermosphere to joule heating and particle precipitation,” *Journal of Geophysical Research: Space Physics*, vol. 111, no. A10, 2006.
- [81] W. H. Campbell, *Quiet Daily Geomagnetic Fields*, W. H. Campbell, Ed. Birkhuser Basel, 1989.
- [82] J. M. Forbes, *Tidal and Planetary Waves*. American Geophysical Union, 2013.

- [83] J. M. Forbes, X. Zhang, S. Palo, J. Russell, C. J. Mertens, and M. Mlynczak, "Tidal variability in the ionospheric dynamo region," *Journal of Geophysical Research: Space Physics* (1978–2012), vol. 113, no. A2, 2008.
- [84] J. M. Forbes, X. Zhang, E. R. Talaat, and W. Ward, "Nonmigrating diurnal tides in the thermosphere," *Journal of Geophysical Research: Space Physics*, vol. 108, no. A1, 2003.
- [85] M. E. Hagan and J. M. Forbes, "Migrating and nonmigrating diurnal tides in the middle and upper atmosphere excited by tropospheric latent heat release," *Journal of Geophysical Research: Atmospheres*, vol. 107, no. D24, 2002.
- [86] D. Pancheva, P. Mukhtarov, B. Andonov, N. J. Mitchell, and J. Forbes, "Planetary waves observed by timed/saber in coupling the stratosphere–mesosphere–lower thermosphere during the winter of 2003/2004: Part 1comparison with the ukmo temperature results," *Journal of Atmospheric and Solar-Terrestrial Physics*, vol. 71, no. 1, pp. 61–74, 2009.
- [87] D. Pancheva, P. Mukhtarov, B. Andonov, N. J. Mitchell, and J. Forbes, "Planetary waves observed by timed/saber in coupling the stratosphere–mesosphere–lower thermosphere during the winter of 2003/2004: Part 2altitude and latitude planetary wave structure," *Journal of Atmospheric and Solar-Terrestrial Physics*, vol. 71, no. 1, pp. 75–87, 2009.
- [88] M. L. Salby, "Sampling theory for asymptotic satellite observations. part ii: Fast fourier synoptic mapping," *Journal of the Atmospheric Sciences*, vol. 39, no. 11, pp. 2601–2614, 1982.
- [89] S. M. I. Azeem, T. L. Killeen, R. M. Johnson, Q. Wu, and D. A. Gell, "Space-time analysis of timed doppler interferometer (tidi) measurements," *Geophysical Research Letters*, vol. 27, no. 20.
- [90] R. R. Garcia, R. Lieberman, J. M. Russell III, and M. G. Mlynczak, "Large-scale waves in the mesosphere and lower thermosphere observed by saber," *Journal of the atmospheric sciences*, vol. 62, no. 12, pp. 4384–4399, 2005.
- [91] M. Jones, J. Forbes, M. Hagan, and A. Maute, "Non-migrating tides in the ionosphere-thermosphere: In situ versus tropospheric sources," *Journal of Geophysical Research: Space Physics*, vol. 118, no. 5, pp. 2438–2451, 2013.
- [92] J. E. Salah, J. V. Evans, and R. H. Wand, "Seasonal variations in the thermosphere above millstone hill," *Radio Science*, vol. 9, no. 2, pp. 231–238, 1974.
- [93] L. Qian and S. C. Solomon, "Thermospheric density: An overview of temporal and spatial variations," *Space science reviews*, vol. 168, no. 1-4, pp. 147–173, 2012.
- [94] W. Menke, *Geophysical data analysis: discrete inverse theory*. Academic press, 2012.
- [95] K. A. Clarke, "The phantom menace: Omitted variable bias in econometric research," *Conflict Management and Peace Science*, vol. 22, no. 4, pp. 341–352, 2005.

- [96] J. J. Heckman, "Sample selection bias as a specification error," *Econometrica*, vol. 47, no. 1, pp. 153–161, 1979.
- [97] G. De Toma, "Evolution of coronal holes and implications for high-speed solar wind during the minimum between cycles 23 and 24," *Solar Physics*, vol. 274, no. 1-2, pp. 195–217, 2011.
- [98] X. Zhu, J.-H. Yee, E. Talaat, M. Mlynczak, L. Gordley, C. Mertens, and J. Russell, "An algorithm for extracting zonal mean and migrating tidal fields in the middle atmosphere from satellite measurements: Applications to timed/saber-measured temperature and tidal modeling," *Journal of Geophysical Research: Atmospheres (1984–2012)*, vol. 110, no. D2, 2005.
- [99] H. Abdi, "Partial least square regression (pls regression)," *Encyclopedia for research methods for the social sciences*, pp. 792–795, 2003.
- [100] W. Gonzalez, J. Joselyn, Y. Kamide, H. Kroehl, G. Rostoker, B. Tsurutani, and V. Vasyliunas, "What is a geomagnetic storm?" *Journal of Geophysical Research: Space Physics (1978–2012)*, vol. 99, no. A4, pp. 5771–5792, 1994.
- [101] C. Loewe and G. Prölss, "Classification and mean behavior of magnetic storms," *Journal of Geophysical Research: Space Physics (1978–2012)*, vol. 102, no. A7, pp. 14 209–14 213, 1997.
- [102] W. Mendenhall, R. Beaver, and B. Beaver, *Introduction to probability and statistics*. Cengage Learning, 2008.
- [103] A. Ng. () Machine learning [Online]. Available: <http://openclassroom.stanford.edu/MainFolder/CoursePage.php?course=MachineLearning>.
- [104] D. J. MacKay, *Information theory, inference and learning algorithms*. Cambridge university press, 2003.
- [105] T. Hastie, R. Tibshirani, and J. Friedman, *The elements of statistical learning theory*. Springer New York:, 2001.

APPENDICES

Appendix A

Coefficients of Quiet Time Variation Model

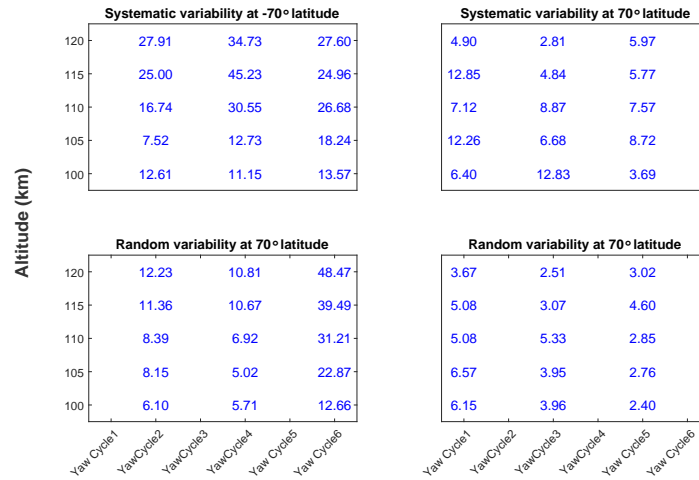


Fig. A.1: Maximum Systematic and random variation at -70° and 70° latitude in %.

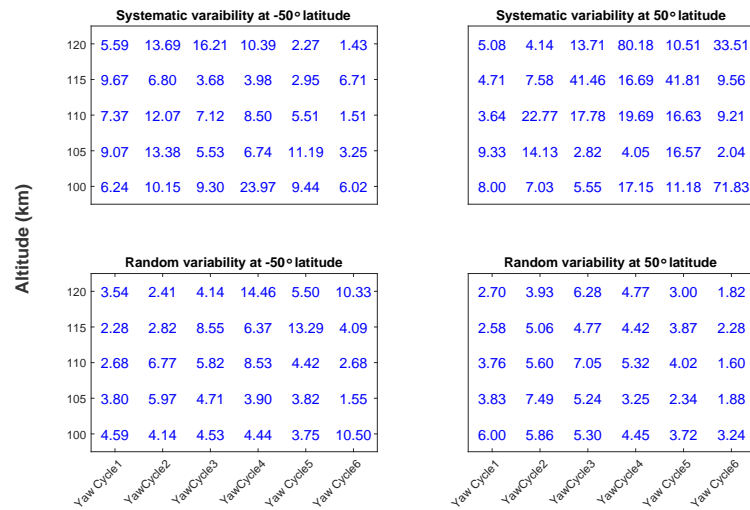


Fig. A.2: Maximum Systematic and random variation at -50° and 50° latitude in %.

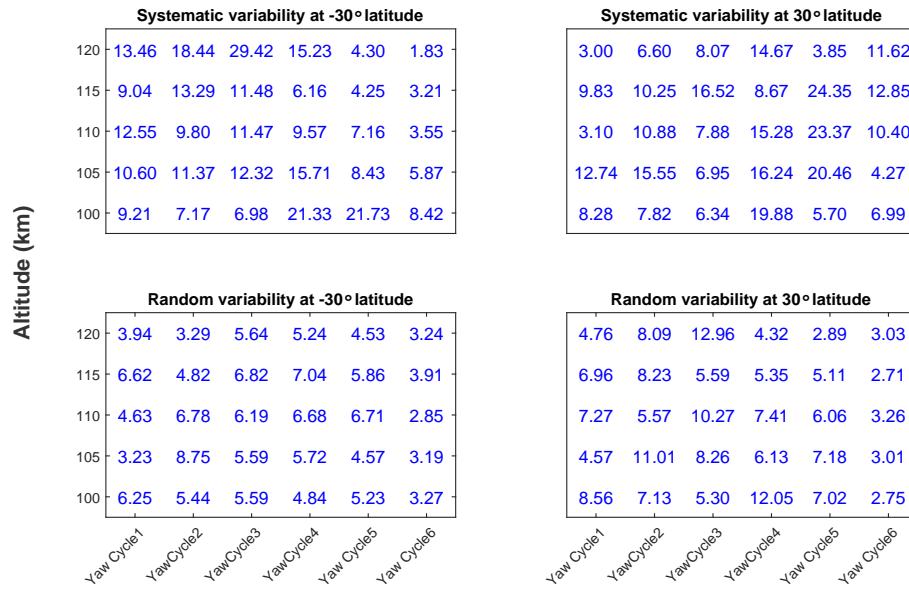


Fig. A.3: Maximum Systematic and random variation at -30° and 30° latitude in %.

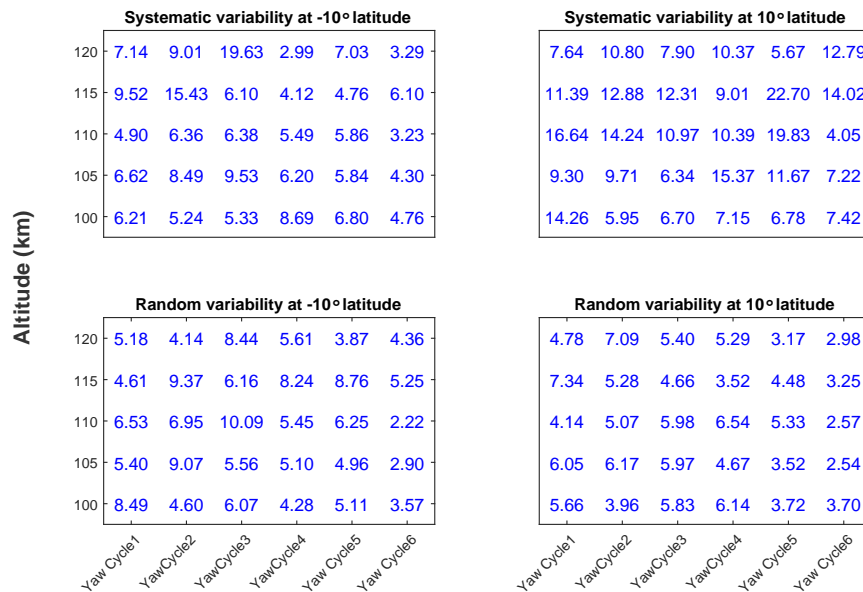


Fig. A.4: Maximum Systematic and random variation at -10° and 10° latitude in %.

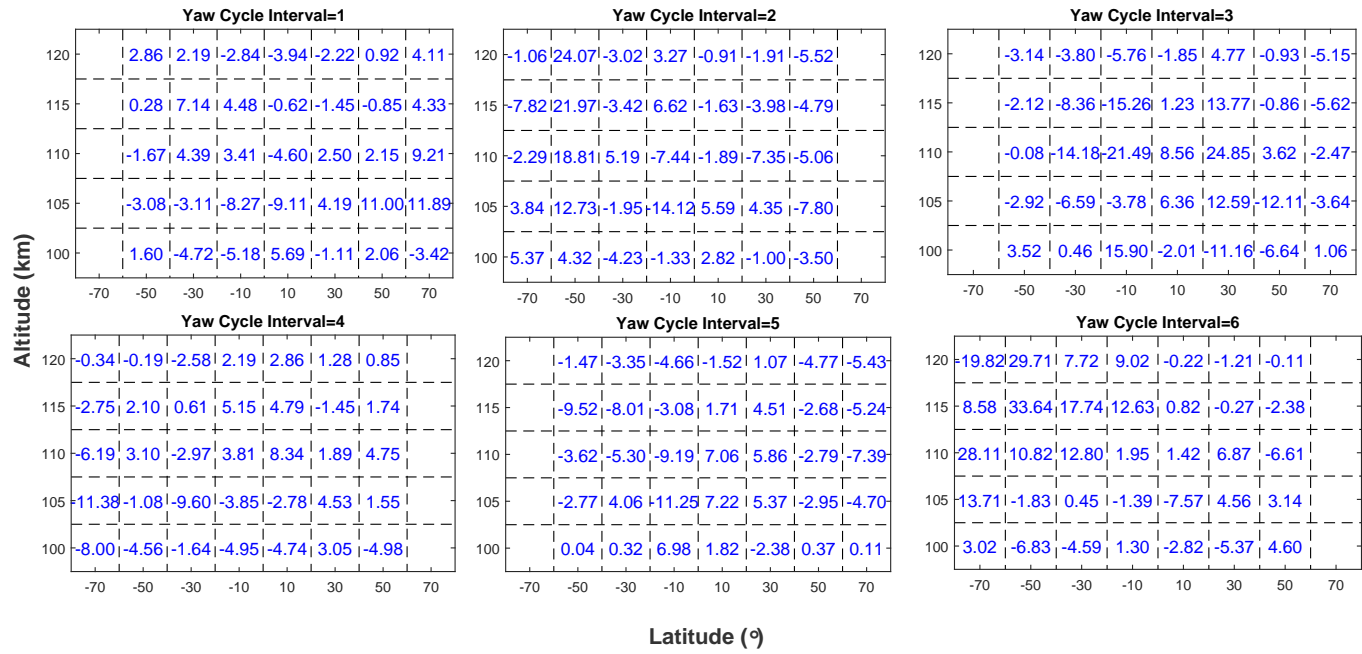


Fig. A.5: Amplitude Coefficient 1 in %

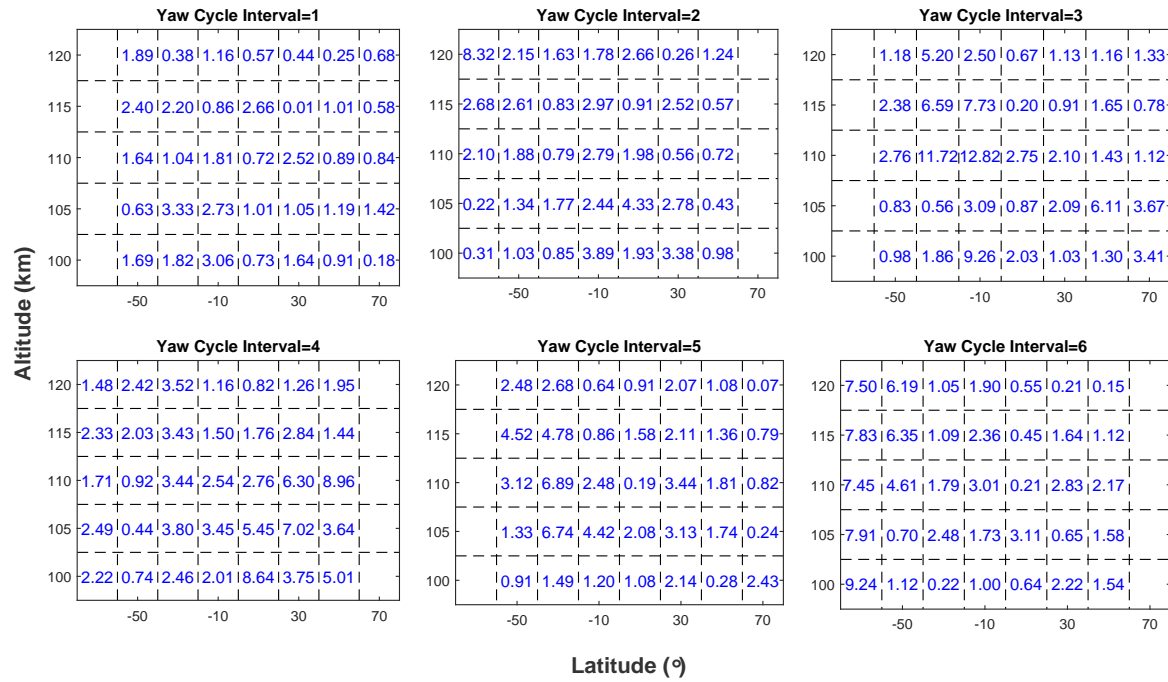


Fig. A.6: Amplitude Coefficient 2 in %

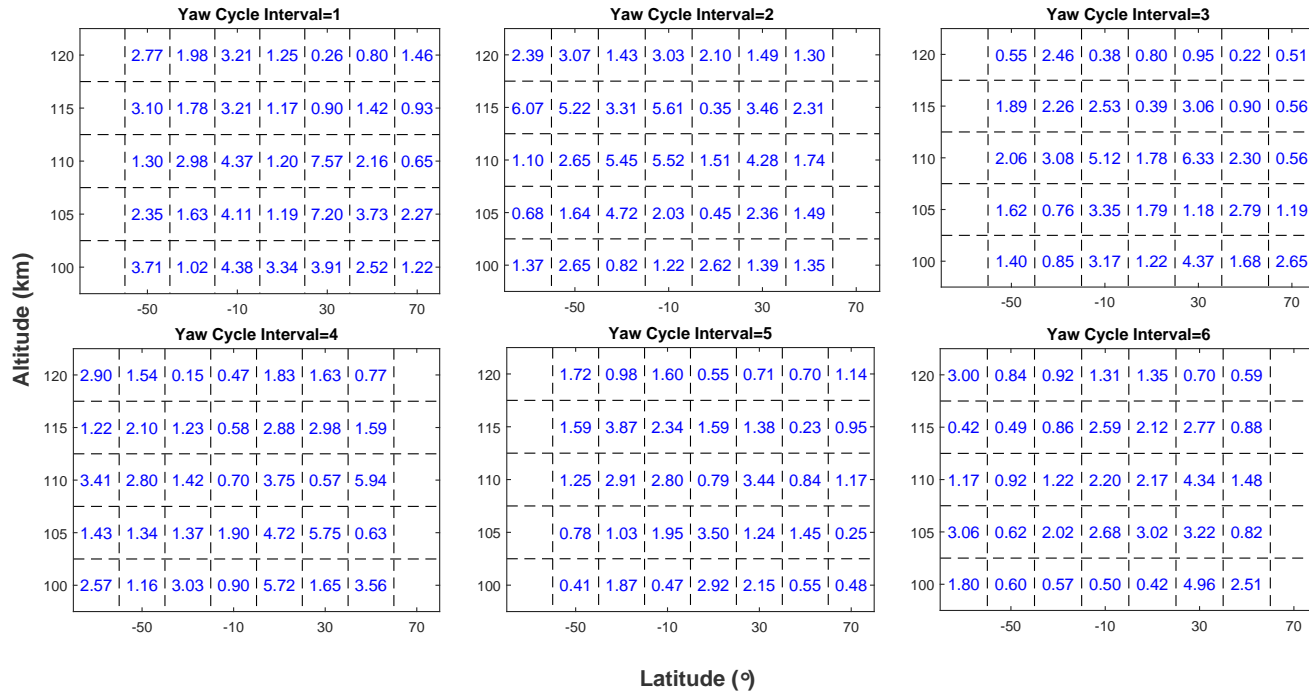


Fig. A.7: Amplitude Coefficient 3 in %

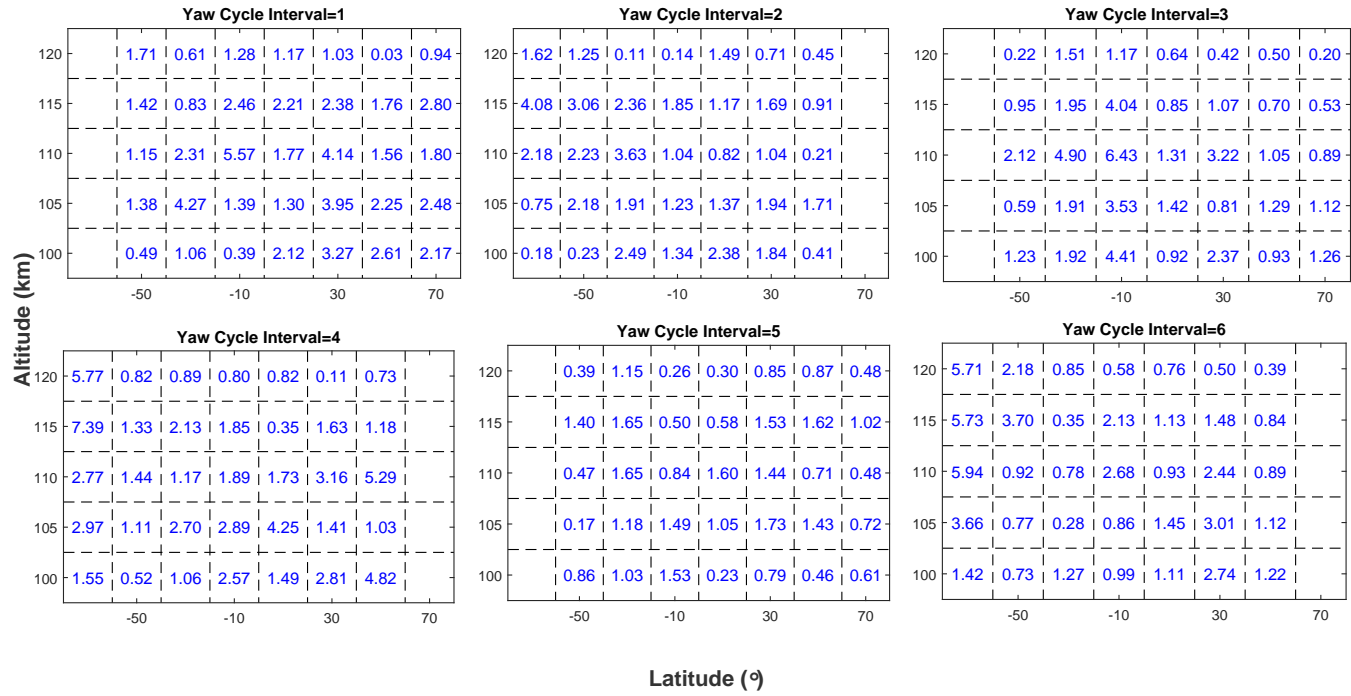


Fig. A.8: Amplitude Coefficient 4 in %

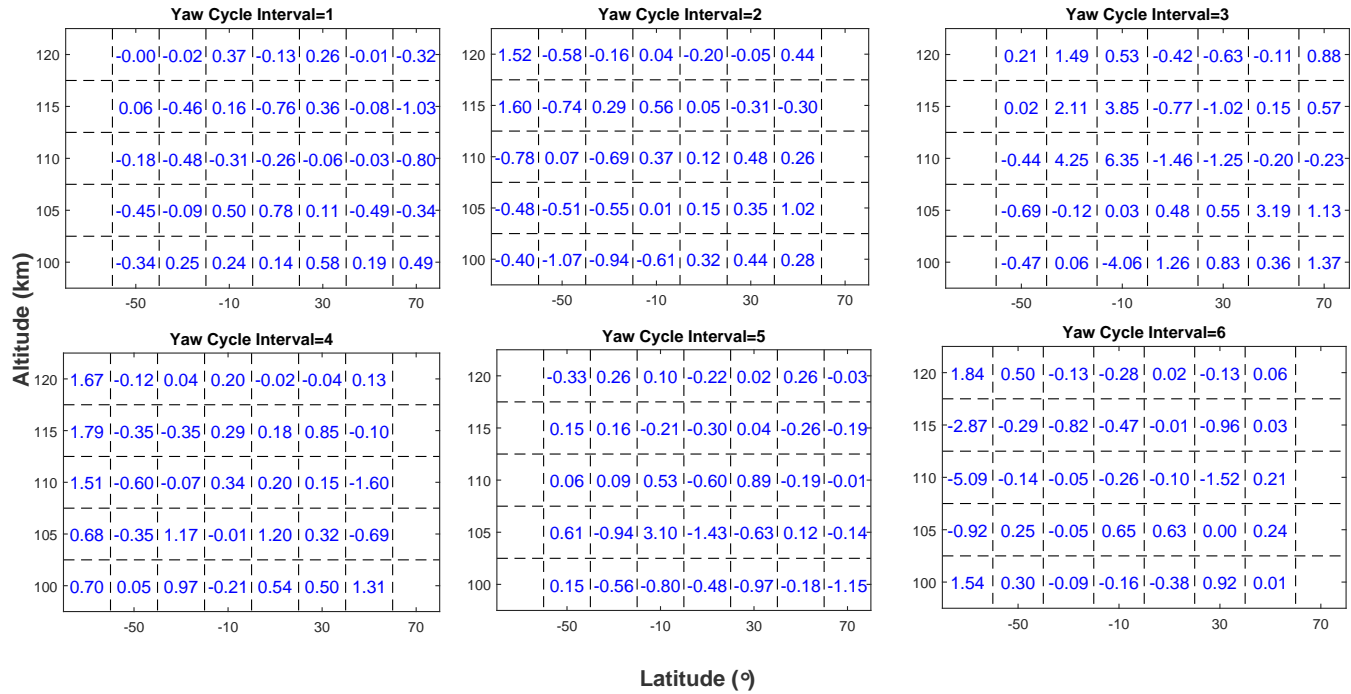


Fig. A.9: Amplitude Coefficient 5 in %

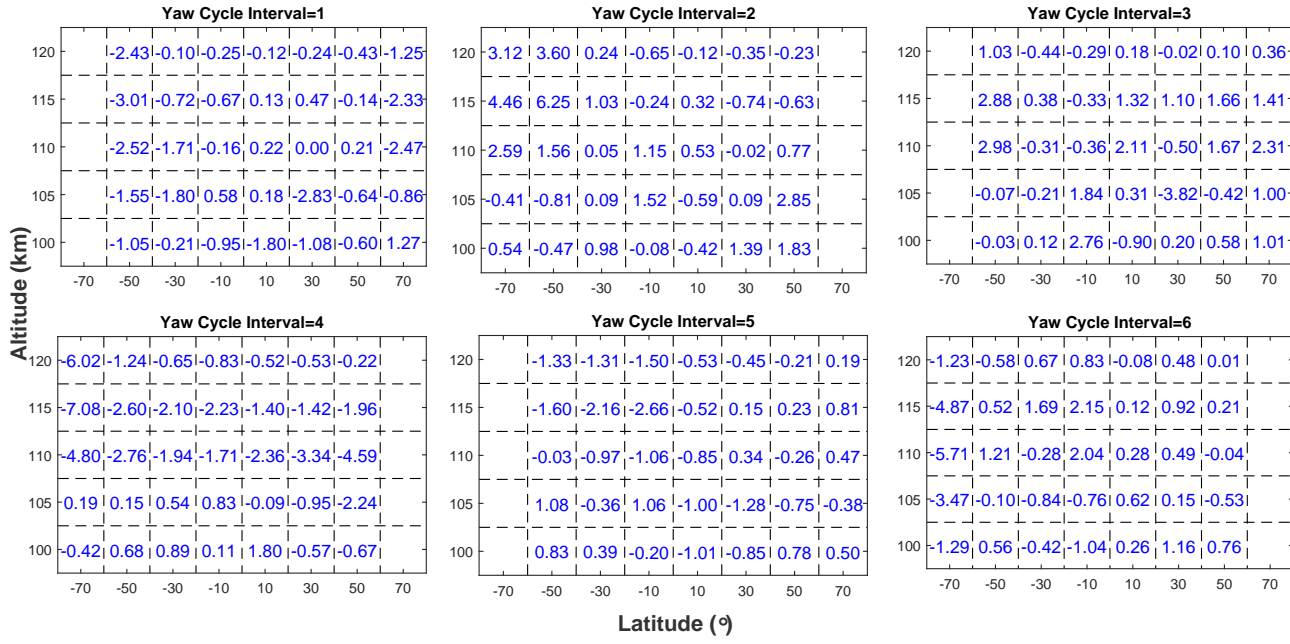


Fig. A.10: Amplitude Coefficient 6 in %

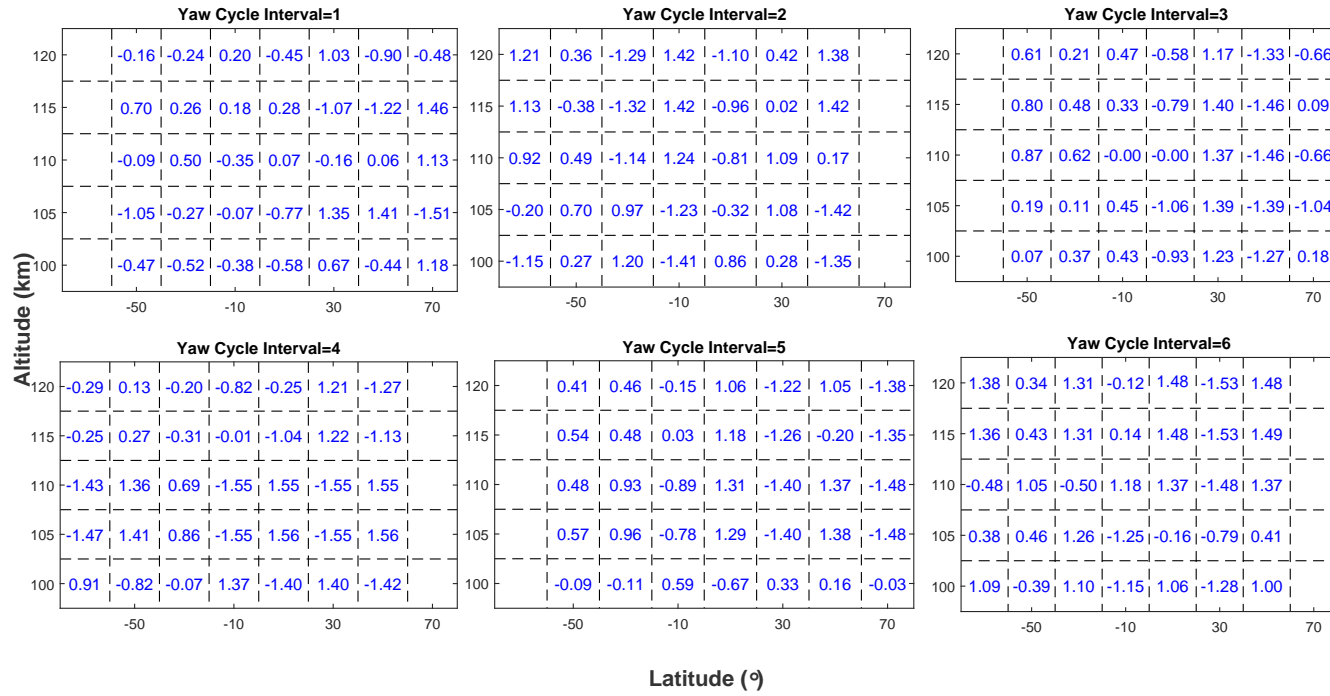


Fig. A.11: Phase Coefficient 1 in radians.

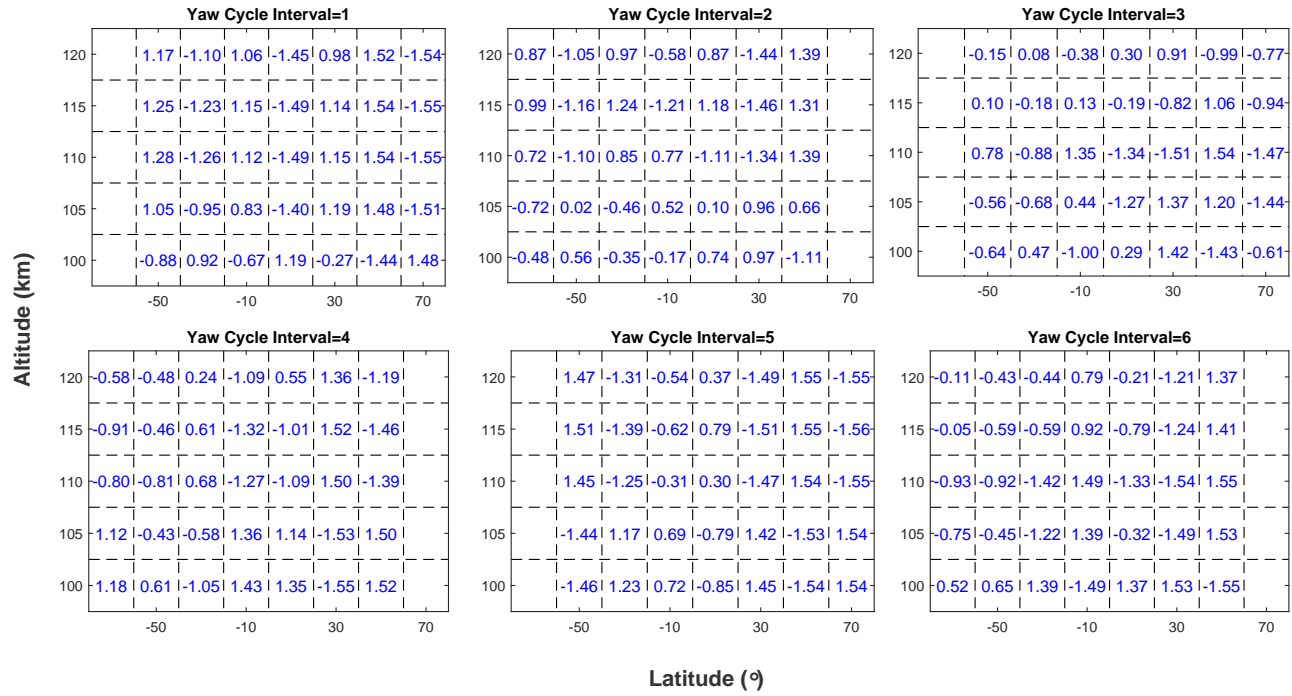


Fig. A.12: Phase Coefficient 2 in radians.

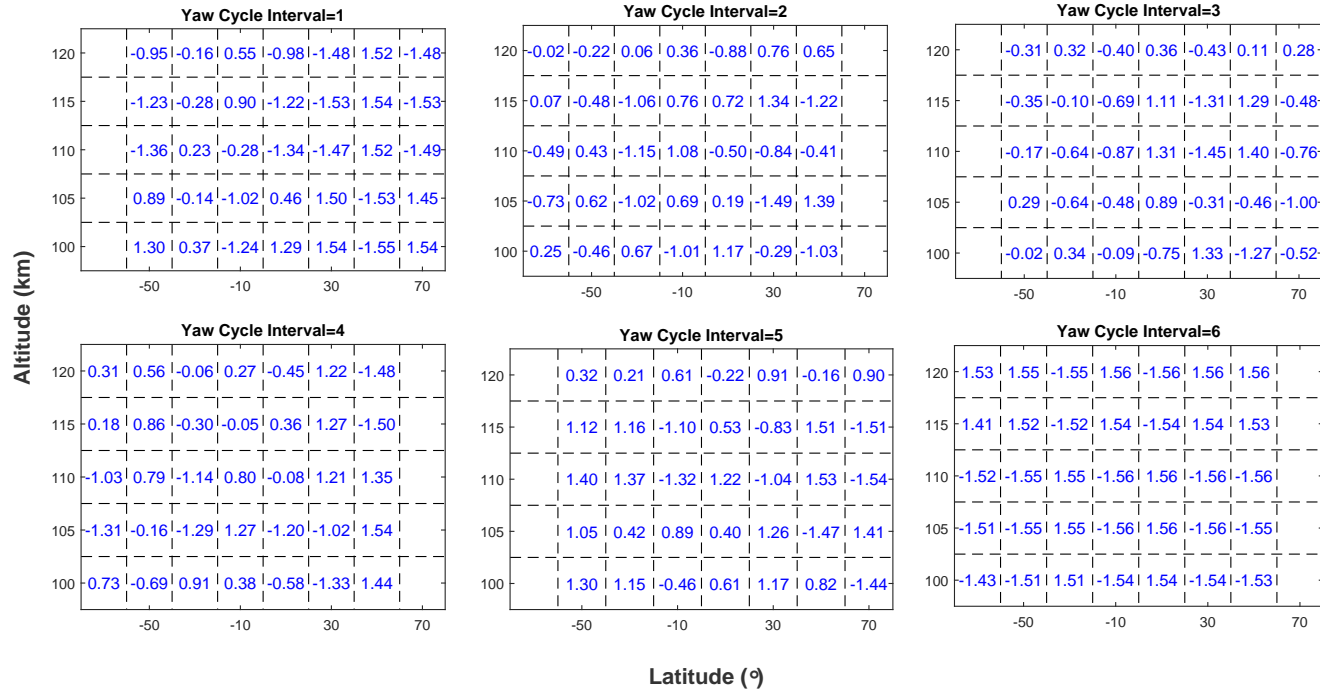


Fig. A.13: Phase Coefficient 3 in radians.

Appendix B

 T_{ref} Across Various Yaw Cycles and Altitude-latitude Bins.

In this section, we present the T_{ref} values which are used in constructing the piecewise quiet time variation model. T_{ref} is the zonal mean temperature of the ascending passes of the first quiet day in each yaw cycle interval of year 2009. It is calculated for each latitude-altitude bin, for every yaw one of the six yaw cycles.

As per the set-up described in Chapter 2, equation 2.14, the magnitude coefficients of the model can be converted back from percentage to absolute temperatures in kelvin on multiplying T_{ref} . Similarly the storm responses calculated using the storm response model, can also be converted back into absolute temperatures in kelvin from % by multiplying T_{ref} .

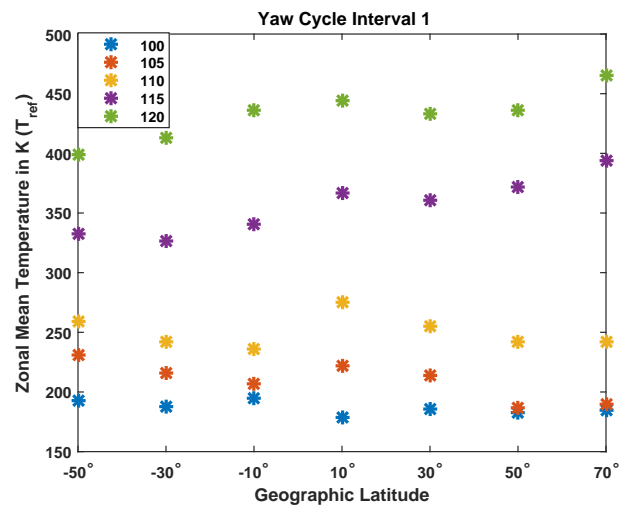


Fig. B.1: T_{ref} for Yaw Cycle Interval 1 for all latitude-altitude bins.

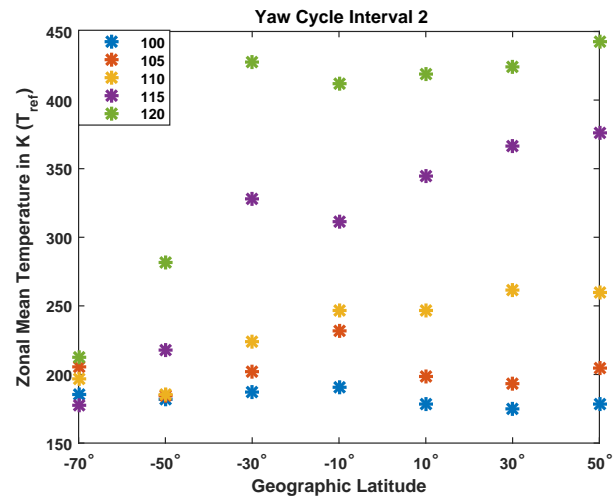


Fig. B.2: T_{ref} for Yaw Cycle Interval 2 for all latitude-altitude bins.

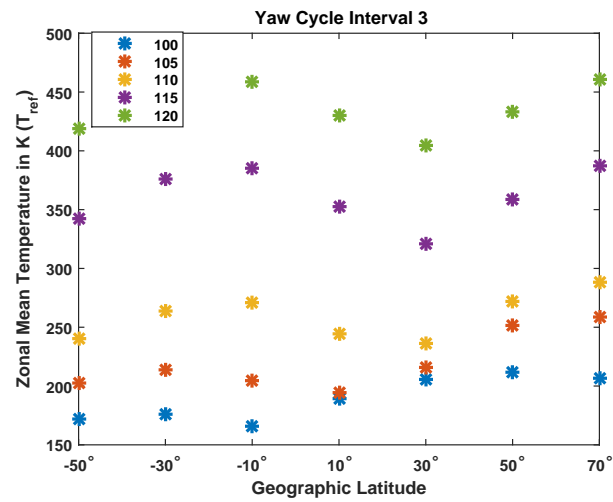


Fig. B.3: T_{ref} for Yaw Cycle Interval 3 for all latitude-altitude bins.

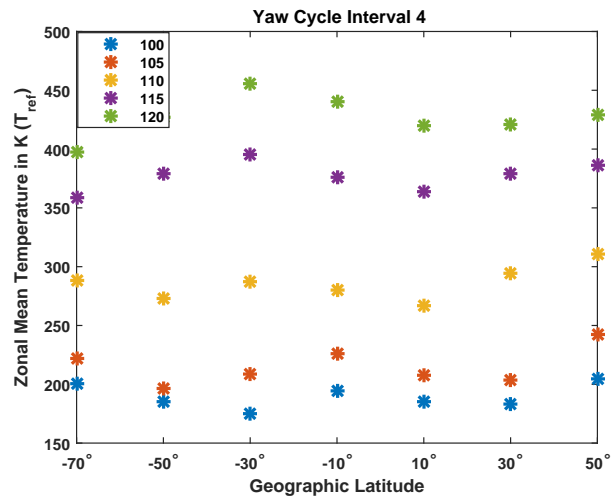


Fig. B.4: T_{ref} for Yaw Cycle Interval 4 for all latitude-altitude bins.

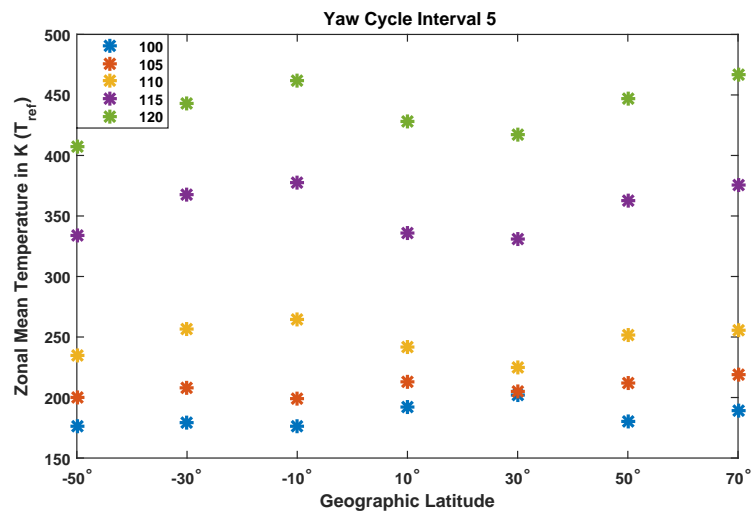


Fig. B.5: T_{ref} for Yaw Cycle Interval 5 for all latitude-altitude bins.

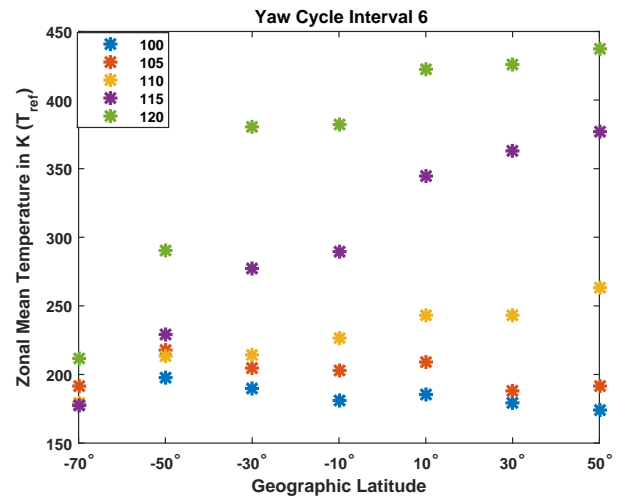


Fig. B.6: T_{ref} for Yaw Cycle Interval 6 for all latitude-altitude bins.

CURRICULUM VITAE

Padmashri Suresh**Education**

Ph.D. in Electrical Engineering, Utah State University (2011-2016).

M.S. in Electrical Engineering, Utah State University (2008-2010).

B.Eng. in Electrical Engineering, Visvesvaraya Technological University (2002-2006).

Published Conference Papers and Articles

- P. Suresh and C. M. Swenson, Study of Thermosphere Temperature Response to Geomagnetic Storms, EOS Trans. AGU Abstract SA21A-4048 (Presented at 2014 Fall Meeting, AGU, San Francisco, Calif.)
- P. Suresh, H. Godinez, R. Linares, and A. Walker, Global Thermospheric Density Response to a Geomagnetic Storms, 2014 LANL Summer School Reports.
- P. Suresh and C. M. Swenson, Measurement Of Lower Thermosphere Using the Optical Profiling of the Atmospheric Limb (OPAL) Cubesat Experiment, 2014 USNC-URSI National Radio Science Meeting.
- P. Suresh and C. M. Swenson , A Novel Method to Analyze Ionospheric Measurements made by a Non-uniformly Contaminated Langmuir Probe On-board a Sounding Rocket.”, 2014 USNC-URSI National Radio Science Meeting.
- P. Suresh and C. M. Swenson, Study of Global Storm Time Energy Transport in the Lower Thermosphere using SABER Temperatures, EOS Trans. AGU Abstract SA31A-1973 (Presented at 2013 Fall Meeting, AGU, San Francisco, Calif. 9-13Dec), 2013.

- P. Suresh and C. M. Swenson, Global Thermosphere Temperature Response to Geomagnetic Storms, CEDAR MLT Poster Session, June 2013.
- P. Suresh and C. M. Swenson, Statistical Study of Storm-Time thermosphere Temperature, EOS Trans. AGU Abstract SA51A-2155 (Presented at 2012 Fall Meeting, AGU, San Francisco, Calif. 3-7 Dec), 2012.
- P. Suresh, C. M. Swenson, C. J. Mertens, and A. B. Christensen. Global thermospheric temperature response to geomagnetic storms. EOS Trans. AGU, Abstract SA11A-1566 (Presented at 2011 Fall Meeting, AGU, San Francisco, Calif. 5-9 Dec.), 2011.
- P. Suresh and C.M. Swenson, ITM Study using ISS as a launch platform, CEDAR Poster Session, June 2011.
- P Suresh, C. Swenson, and A.B. Christensen. A statistical nighttime analysis of the equatorial ionization anomaly. EOS Trans. AGU , Abstract SA51B-1638 (Presented at 2010 Fall Meeting, AGU, San Francisco, Calif. 13-17 Dec.), 2010.
- S Burr, C. Swenson, C. Fish, G. Crowley, D. Hui, P. Suresh, and T. Neilsen. Expected performance of the plasma diagnostic instrumentation on DICE. EOS Trans. AGU , Abstract SA43B-1769 (Presented at 2010 Fall Meeting, AGU, San Francisco, Calif. 13-17 Dec.), 2010
- P. Suresh and C. M. Swenson. Implications of contamination and surface area ratios for Langmuir probe diagnostics on CubeSats. EOS Trans. AGU, Abstract SM33C-1573(90(52)):Fall Meet.Suppl., 2009.
- P. Suresh and C. M. Swenson. Estimation of Langmuir probe currents in the event of surface potential variation. CEDAR, Poster Session, July 2009.

Patents

- Intelligent System and Fuzzy Logic Based Method to determine Project Risk. Inventors: Padmashri Suresh, Sri Ramanathan, Matthew B. Trevathan, and Balaji

Venkatraman., IPC8 Class: AG06Q1000FI , USPC Class: 705 9 , USPTO Patent application number: 20100030609. Patent assigned to IBM.

- Fuzzy Logic for Project Time estimation, Protected IBM Intellectual Capitals.

Awards and Honors

- Semi-finalist, Presidential Management Fellow, 2015.
- NASA Earth and Space Science Fellowship (NESSF), 2011-2015.
- Vela Fellowship at Los Alamos National Labs, 2014.
- National Academy of Science (NAS) Science and Technology Policy Fellowship (Christine Mirzayan Policy Fellowship).
- 3rd prize, Ernest K. Smith paper competition, 2014 U.R.S.I. National Radio Science Meeting.
- U.S. National Committee for the International Union of Radio Science (U.S.N.C.-U.R.S.I.) Travel Fellowship Grant.
- Utah State University Students Association Scholarship, 2013-2014.
- Honorable Mention, Student Poster Competition, NSF Geospace and Geoscience Conference (CEDAR), 2009.
- Graduate Student Fellowship, Department of Electrical and Computer Engineering, Utah State University, 2008-2009.

Service and Leadership

- Director of Graduate Research, Associated Students of Utah State University, selected to represent the graduate student body at Utah State University, 2013-2014.
- Chair, Research and Project Grants Committee, Utah State University, 2013-2014.

- Member, Graduate Council, Utah State University, 2013-2014.
- Member, Enhancement Awards, Utah State University, 2013-2014.
- Executive Secretary, 2013 NASA Heliophysics Panel, NASA HQ.
- Executive Secretary, 2009 NASA Causes and Consequences of the Minimum of Solar Cycle Panel, NASA HQ.